Chemistry of Functional Molecules at Metal Surfaces

Dissertation

zur

Erlangung der naturwissenschaftlichen Doktorwürde
(Dr. sc. nat.)

vorgelegt der

Mathematisch-naturwissenschaftlichen Fakultät

der

Universität Zürich

von

Jingyi Li

aus

V.R. China

Promotionskommission

Prof. Dr. Karl-Heinz Ernst (Vorsitz)

Prof. Dr. Roger Alberto

Prof. Dr. Jürg Osterwalder

Zürich, 2017

寄蜉蝣于天地，渺沧海之一粟。

苏轼

Abstract

This thesis reports studies of various surface-assisted chemical reactions using thermally deposited organic molecules on metal surfaces under ultra-high vacuum conditions, studied by means of scanning tunneling microscopy, X-ray photoelectron spectroscopy and thermal desorption spectroscopy.

At first, thin layers of the strong electron acceptor corannulene were metalated with alkali metal atoms, *i.e*. potassium and lithium, after deposition onto a Cu(111) single crystal surface. Formation of a stable compound was observed around 400 K for potassium, with a ration of with 4 K^+ ions per corannulene molecule. In the case of lithium, no stable compound/complex was observed, because of substantial higher thermal stability of lithium films. This fact did not allow an approach using Li in access with respect to corannulene for compound formation. Using lithium at small amounts failed due to the very small sensitivity in photoelectron spectroscopy, the method used for stoichiometric analysis.

Secondly, sub-monolayer and monolayer coverages of free-base pyrphyrin molecules on Cu(111) were investigated for their ability of on-surface metalation with Cu-adatoms and subsequent formation of highly ordered organometallic layers. The metalation of the free-base pyrphyrin macrocycle with ruthenium atoms, deposited by e-beam evaporation, on a Au(111) surface has been successfully demonstrated. Due to the high cohesive nature of ruthenium, only a partial metalation has been achieved. The role of the cyano groups of the pyrphyrin macrocycle has been further explored using cobalt pyrphyrin and Ni adatoms on both Cu(111) and Au(111) surfaces.

Thirdly, thermally grown graphene on Cu(111) from both planar and pentagon-rich curved polycyclic aromatic hydrocarbon (buckybowls) precursors has been achieved and the graphene topography and its growth dynamics have been demonstrated in details. It is evidenced that, polycyclic aromatic hydrocarbon’s original structure was broken at relatively low temperatures before graphene flake formation starts. Thus, it is not possible to introduce defects with pentagonal rings in a controlled manner into the later produced graphene with this method.

Lastly, stereoselective Ullmann coupling reactions have been realized using bromo-helicene molecules on metal surfaces. 2-bromo[4]helicenes couple into a dimer by forming a new single C-C bond on Cu(100) while 2,3-dibromo[4]helicenes form a tris-helicene product by generating a new C6 aromatic ring on Au(111). In both cases of dimerization or trimerization, homochiral combinations of the precursors were observed and the produced enantiomers assemble into 2D conglomerates of homochiral domains.

Zusammenfassung

Diese Dissertation berichtet über Untersuchungen verschiedener chemischer Reaktionen mit thermisch abgeschiedenen organischen Molekülen auf Metalloberflächen unter Ultrahochvakuumbedingungen. Dien Studien wurden mittels Rastertunnelmikroskopie, Röntgen-Photoelektronenspektroskopie und thermischer Desorptionsspektroskopie durchgeführt.

Zuerst wurden dünne Schichten des starken Elektronenakzeptors Corannulen nach der Abscheidung auf einer Cu(111)-Einkristalloberfläche mit Alkalimetallatomen, *d.h.* Kalium und Lithium, metallisiert. Die Entstehung einer stabilen Verbindung wurde bei rund 400 K im Falle von Kalium beobachtet, und zwar mit einem Verhältnis von 4 K^+ Ionen pro Corannulen Molekül. Bei Lithium wurde aufgrund der wesentlich höheren thermischen Stabilität von Lithiumfilmen kein stabiler Komplex beobachtet. Aufgrund dessen lässt sich kein Weg finden, wie ein Lithium-Corannulen Komplex gebildet werden kann, auch nicht mit Li im Überschuss im Vergleich zu Corannulen. Auch die Verwendung von Lithium in kleinen Mengen scheiterte, und zwar an der sehr geringen Empfindlichkeit der Photoelektronenspektroskopie, der Methode zur stöchiometrischen Analyse.

Zweitens wurden Sub-Monolayer- und Monolayer-Bedeckungen von freien Pyrphyrin-Molekülen auf Cu(111) auf ihre Fähigkeit hin untersucht, mit Cu-Adatomen an der Oberfläche zu metallisieren und anschließend hochgeordnete metallorganische Schichten zu bilden. Die Metallisierung des Pyrphyrin- Makrocyclus mit Rutheniumatomen, die durch Elektronenstrahlverdampfung auf einer Au(111)-Oberfläche abgeschieden wurden, konnte erfolgreich nachgewiesen werden. Die Rolle der Cyano-Gruppen des Pyrphyrin-Makrocyclus wurde weiter erforscht, indem Kobalt-Pyrphyrin und Ni Adatome sowohl auf Cu(111) als auch auf Au(111)-Oberflächen verwendet wurden.

Drittens wurde thermisch gewachsenes Graphen auf Cu(111) sowohl aus planaren als auch aus fünfeckigen schalenförmigen polycyclischen aromatischen Kohlenwasserstoffen (Buckybowls) gewonnen. Die Graphentopographie und ihre Wachstumsdynamik wurden detailliert studiert. Die ursprüngliche Struktur der polycyclischen aromatischen Kohlenwasserstoffen wurde bei relativ niedrigen Temperaturen aufgebrochen, bevor die Bildung von Graphendomänen begann. Daher ist es mit diesem Verfahren nicht möglich, Defekte bestehend aus fünfeckigen Ringen kontrolliert in das später hergestellte Graphen einzubringen.

Schließlich wurden stereoselektive Ullmann-Kupplungsreaktionen mit Bromhelicen-Molekülen auf Metalloberflächen realisiert. 2-Brom[4]helicene koppeln zu Dimeren, indem sie eine neue C-C-Bindung auf Cu(100) bilden, während 2,3-Dibrom[4]helicene ein Trishelicenprodukt bilden, indem sie einen neuen aromatischen C6-Ring auf Au(111) erzeugen. In beiden Fällen der Dimerisierung oder Trimerisierung wurden homochirale

Kombinationen der Vorläufer beobachtet und die so hergestellten Enantiomere zu 2D-Konglomeraten in homochiraler Domänen zusammengefügt.

Acknowledgment

All these years in Zürich are full of exciting adventures and vibrant memories, filled with both laughers and tears.

First I would like to thank my parents, Junli and Zhenyu Li. I probably would not have pursued a Ph.D. if not for their encouragements. This journey starts there.

I want to thank my thesis supervisor Prof. Karl-Heinz Ernst for offering the opportunity for working in this exciting field of natural science and the support I received during the whole course of this my doctoral studies. He is truly a skilled and inspiring mentor.

I thank Manfred Parschau for all the insightful scientific suggestions in the lab as well as amusing conversations during coffee breaks. I thank Prof. Hans Josef Hug for his always timely and immense supports even though he is very busy.

I thank Christian Wäckerlin, my valuable friend and colleague, for all the scientific and non-scientific discussions, as well as for all the help in the lab and with the thesis.

I thank my fellow Ph.D students in our group, Anais Mairena, Gitika Srivastava, and Alexandra Rieger, for making our research group so much fun beyond science. I thank the rest of Nanoscale Materials Science laboratory in Empa for being supportive in maintaining such a professional yet always-fun environment. Particularly, I want to thank Xue Zhao and Liying Ma for being truthful friends next door.

I would also like to thank all my friends in Zürich, especially Meijun Liu and Ferenc Muranyi. Meijun has been a beloved friend through all ups and downs with me all the years during my doctoral studies with her passion towards life and calming personality. Ferenc has been a reliable friend and always gave me constructive suggestions based on fruitful experiences as a doctor himself.

Financial support from University Research Priority Program LightChEC is also greatly acknowledged. Graduate School of Chemical and Molecular Sciences Zurich (CMSZH) helped in printing this thesis.

Jingyi Li

Zürich, June 2017

Table of Contents

Abstract

Zusammenfassung

Acknowledgment

Chapter 1 Introduction ... 1

Chapter 2 Experimental Methods ... 3

- 2.1 X-ray photoelectron spectroscopy (XPS) ... 3
- 2.2 Scanning Tunneling Microscopy (STM) ... 3
- 2.3 Thermal desorption spectroscopy (TDS) ... 5
- 2.4 Experimental setups ... 6

Chapter 3 Metalation of corannulene with alkali metals: thin film syntheses on a Cu(111) surface ... 9

- 3.1 Chemistry of corannulene with potassium on the Cu(111) surface ... 10
- 3.2 Chemistry of corannulene and Li as thin films on the Cu(111) surface ... 14
- 3.3 Conclusions ... 19

Chapter 4 Self-assembly and metal coordination of surface-adsorbed pyrphyrin molecules ... 21

- 4.1 Metalation on Cu(111) ... 21
- 4.2 Coordination networks of CoPyr on Cu(111) and Au(111) ... 28
- 4.3 Pyrphyrin metalation with ruthenium ... 31
- 4.4 Conclusion ... 33

Chapter 5 An on-surface pathway from PAHs to graphene ... 35

- 5.1 Graphene from pentaindenocorannulene ... 36
- 5.2 Graphene from coronene ... 43
- 5.3 Self-assembly of excess carbon: a new unknown species ... 47
- 5.4 Conclusion ... 49

Chapter 6 Ullmann Coupling of bromo-helicenes on metal surfaces ... 51

- 6.1 2-Bromo[4]helicene on Cu (100) ... 51
- 6.2 Trishelicenes from 2,3 -dibromo[4]helicene on Au(111) ... 56
- 6.3 Conclusion and Outlook ... 60

Appendix ... 63

References ... 67

List of Publications and conference contributions

Curriculum Vitae

Chapter 1 Introduction

Surface-assisted chemical reactions have been of great interest in the scientific field of molecular nanoscience in the past three decades. Surfaces constrain the reactants in two dimensions, thus the reactions can be precisely controlled. The educts and products of on-surface reactions can be directly probed using various methods, including spatially resolving techniques such as scanning tunneling microscopy and atomic force microscopy, and surface-sensitive, spatially averaging methods such as X-ray photoelectron microscopy. Moreover, if reaction products desorb from the surface, they can be identified using thermal desorption spectroscopy. Reactions at atomically clean, single crystal surfaces in ultra-high vacuum are thus impeccable model systems to deepen the fundamental understanding of chemistry.

These model systems also give the possibility of solvent-free reactions which could not happen otherwise because of interference with the solvent. Furthermore, novel reaction products can be obtained at surfaces due to steric constraints of being adsorbed, due to the catalytic activity of the (metal) surface and due to their insolubility. In addition different reaction conditions can be precisely tailored and are attainable experimentally. For example, instead of designing a reaction by choosing different solvents and reagents' concentrations, other control parameters such as deposition rates can be regularly tuned.

For some reactions which require harsh conditions, the presence of metal surfaces allows for a milder environment. Another example is a type of reactions which contain extremely active reagents such as alkali metals. These reactions are only achievable when any exposure to air is strictly avoided. At ambient pressure the metal oxidizes much faster than the expected reaction. Thus ultrahigh vacuum experiments are a must for these kinds of reactions. Chapter 3 presents exactly such a case. Within these *in-vacuo* experiments complex-compounds consisting of small organic molecules and potassium/lithium can be obtained and kept clean for days for further measurements.

One surface-specific reaction, typically known as surface-assisted metalation [1], is a successful way for synthesis of novel functionalized molecules. Due to either the insolubility of the specific molecules used here or the extreme requirements of the reaction conditions in general, the metal coordination of organic molecules is usually more easily accessible through surface-metalation. These metalated molecules are predicted to provide promising catalytic properties *via* their coordinated metal atoms [2–4]. And the variety of metal species and their tunable physical and chemical properties, such as spin [5–9] and oxidation states [10,11], opens new doors to novel applications, such as spintronics, superconductivity or their use as organic semiconductors. Surface-mediated metalation is typically completed in planar macrocycles such as porphyrin and phthalocyanines, and self-assembly [12–14] of these molecules at surfaces is commonly achieved. Thus the phenomenon of 2D crystallization allows obtaining highly ordered layers, *i.e*. functionalized surfaces, from mere bottom-up assembly. Unlike crystallization processes of bulk, self-assembly on surfaces is usually dominated by the substrate chemical properties and lattice symmetry [15]. Moreover, 2D crystallization of molecules can play an important role in supramolecular chemistry [16,17]. In this way, both the molecular functionality and 2D nanostructures can be tuned for potential future applications.

Chapter 4 of this thesis reports how a novel macrocycle "pyrphyrin" undergoes metalation reactions and its subsequent self-assembly on copper surfaces [14]. This finding extends the concept of surface functionalization by metalation to a different class of macrocycle and thus opens new doors towards different possible molecular functionality and specific catalytic activity.

As the metalation modifies functionality on a molecular level and self-assembly usually produces physically linked network on surface, a more stable covalently-extended network on surfaces is more beneficial in most of application. Graphene, a single layer of sp^2-bonded carbon atoms, has received intense attention in the last decade for example due to its exceptional electronic properties. For many applications, large high-quality graphene layers with few defects and domains are desirable, while for other applications defect-rich graphene are more attractive [18–20]. In most studies of graphene growth on metal surfaces via chemical vapor deposition (CVD), the precursor, *i.e.* the carbon source, is a simple gaseous hydrocarbon. Recently it has been reported that graphene can also be synthesized by depositing larger polycyclic aromatic hydrocarbons (PAHs) such as coronene, pentacene, rubrene [21,22]. In the attempt to explore the possibility of engineering defects in graphene, chapter 5 reports *in-situ* studies of producing graphene of different distinctive qualities via deposition of two PAHs onto a hot copper surface.

Another category of a typical surface reaction leading to covalent bond formation is the Ullmann coupling between aryl halides on copper [23]. While traditional requirements of the reaction conditions are harsh, surface experiments on a copper surface is most successfully achieved in ultra-high vacuum (UHV) [24–30]. By tailoring the functional groups of the molecules, as well as reaction control parameters, such as evaporation rate, substrate symmetry, and annealing temperatures, different products can be achieved as expected. Amongst these examples were graphene nanoribbons [29,31] and hyperbenzene [30,32]. Since the covalent C-C bonds are formed in a highly controlled fashion, Ullmann coupling has been considered the most suitable reaction to achieve surface engineering with stable outcome. Stereoselective Ullmann reactions are reported in Chapter 6 of this thesis using bromo-helicene molecules [33].

Chapter 2 Experimental Methods

2.1 X-ray photoelectron spectroscopy (XPS)

X-ray photoelectron spectroscopy (XPS) is a surface sensitive analytical technique, also known as Electron Spectroscopy for Chemical Analysis (ESCA). Kai Siegbahn's research group first developed the XPS technique in 1954 and he was awarded with the Nobel Prize in 1981 for it [34,35]. It is a widely used surface characterization technique, which gains its popularity due to its high information content, flexibility in detecting various elements on the sample's surface, and firm theoretical basis [36].

The general principle of XPS is as follows: the sample is irradiated by x-rays of specific energy. Thereby electrons are excited from the core levels of the atoms and photoelectrons are generated. These photoelectrons have a kinetic energy given by Einstein's equation:

$$E_k = h\nu - E_B - \varphi, \quad (1)$$

where E_B is the binding energy of electrons in inner shell of the atom, $h\nu$ is the photon energy of x-rays, E_k is the kinetic energy of the emitted photoelectrons which is measured, and φ is the work function. Thus, from the known photon source energy emitted by the x-ray source and from the detected kinetic energy, the binding energy, which provides atomic and structural information, can be calculated.

Binding energies differ for different elements, electronic levels, as well as for each atom’s chemical environment. In each atom, the electron closer to the nucleus exhibits a greater binding energy. The variation in binding energy of a specific core level of a specific element depends on the different chemical environment of the atoms and is known as chemical shift.

XP spectra can provide rich information about a surface within the surface proximal layers [36]. Both qualitative and quantitative information can be obtained, such as the identification of elements, the determination of the approximate surface composition, the oxidation state of surface atoms, molecular environment, *etc.*, without destroying the surface structure [36].

2.2 Scanning Tunneling Microscopy (STM)

Invented in 1981 [37–39], by Binnig and Rohrer (awarded with the Nobel Prize in 1986), scanning tunneling microscopy (STM) has become a very powerful and widely used surface imaging technique [37,40]. By mapping the electronic density of states at surfaces, it gives high-resolution images of a surface in real space with a lateral resolution below 1 Å. Later developments of STM include manipulation at the single atom level, local spectroscopy and detection of magnetic properties of a single molecule/atom. It is commonly used under UHV conditions, yet instrumentation working at ambient pressure and in various liquids has also been achieved.

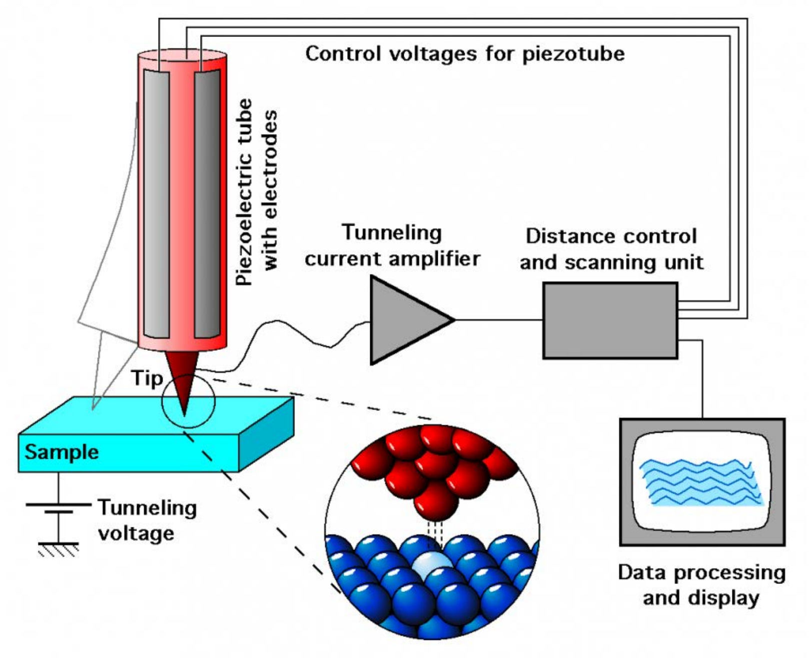

Figure 2.1: schematic drawing of the STM, figure by Michael Schmid, TU Wien

The essential elements of STM are illustrated in Figure 2.1. The probe tip is usually made of W or Pt-Ir alloy. It is mounted on a piezoelectric drive, which can control the tip movement both horizontally (x and y directions) and vertically (z direction). Thus, the atomically sharp tip can approach so close to the sample surface that the electron wave functions of the tip and the surface atoms overlap. Tunneling of electrons occurs if a bias voltage between sample and tip is applied. By measuring the tunneling currents at different positions on the surface, a 2D map of electron density at the surface can be obtained. There are two major scanning modes, constant current and constant height mode. In this work the constant current mode is used, where the tunneling current is kept constant and the tip height is regulated and recorded while scanning.

As mentioned above, STM is based on the quantum tunneling effect. In quantum mechanics, an electron has a probability of tunneling through a potential barrier. In the STM setup, this means that electrons can tunnel through the vacuum level barrier between the sample and the tip. ϕ is the work function of the metal sample, which is defined as the minimum energy required for an electron to escape from a solid to the vacuum level. It depends on both the surface material used and the surface crystallographic orientation. E_F is the Fermi energy level of the metal, which is the upper energy level of occupied states in a metal. If no voltage between the tip and the sample is applied, the Fermi levels of the tip and the sample are identical, because both metals are in contact. So electrons can tunnel from the sample to the tip, *vice versa*. After applying a bias voltage V between the tip and the sample, a net tunneling current occurs. Here it is assumed that $e \cdot V \ll \phi$. By definition, the transmission coefficient T(E) is the probability where electron tunneling occurs. It can be deducted from quantum mechanics as following [41]:

$$T(E) \propto \frac{eV}{E_{Vac}} \cdot e^{-kz} \qquad (2)$$

where $k = \sqrt{2m\varphi}/\hbar$ is momentum of the electron and *z* is the distance between the tip and the sample. The transmission coefficient *T(E)* and hence the tunneling current can be adjusted by the bias applied between the tip and the sample. The tunneling current also depends exponentially on the tip sample distance *z, i. e.* the current decays exponentially as the distance between the tip and the sample increases. The barrier height represents the conduction of the tunneling gap, which in turn depends on the density of states in the surface and the tip. Thus, a STM image is always a representation of the surface topography represented by its density of states as well as the density of states and the shape of the tip.

Here in this thesis, all STM images that have been processed, *i.e.* flattening, subtraction *etc*. by using the WSxM software [42].

2.3 Thermal desorption spectroscopy (TDS)

Thermal desorption spectroscopy (TDS), also known as temperature programmed desorption (TPD), is a surface technique which is used to study the kinetic and thermodynamic parameters of desorption processes where atoms or molecules (intact or their fragments) thermally desorb from a surface. The main setup of TDS is shown in Figure 2.2. The essential parts are a temperature control unit, which is able to ramp the sample temperature at a constant rate during measurement, and a mass spectrometer as detector of desorbed particles in the gas phase. In this work, two different approaches have been used. In the first, the used quadrupole mass spectrometer was placed in a special, differentially pumped housing with a pin-hole, a so-called Feulner cup. The cup could be moved closely in front of the sample in order to collect only desorbing materials from the sample surface, rather than from other degassing surfaces (*e.g*. the heating filament or the sample holder). The second set-up had the quadrupole mass spectrometer without any cup.

The measured signal is proportional to the partial pressure of certain particles of desorbed molecules or molecular fragments (to be defined by the mass setting of the spectrometer) and can be related to the desorption rate $\frac{d\theta}{dt}$ [43]. Thermal desorption is an activated process and can be described by an Arrhenius-like equation, the so-called Polanyi-Wigner equation [44]:

$$I(T) \sim r_{des} = -\frac{d\theta}{dt} = v(\theta,T) \cdot \theta^n \cdot exp\left(\frac{-E_{des}(\theta,T)}{k_B T}\right) \qquad (3)$$

Here, r_{des} is the desorption rate, $v(\theta,T)$ is the pre-exponential frequency factor as a function of coverage and temperature, θ is the coverage of the adsorbates, n (typically $0 \leq n \leqslant 2$) is the reaction order of the desorption process and E_{des} is the activation energy for desorption.

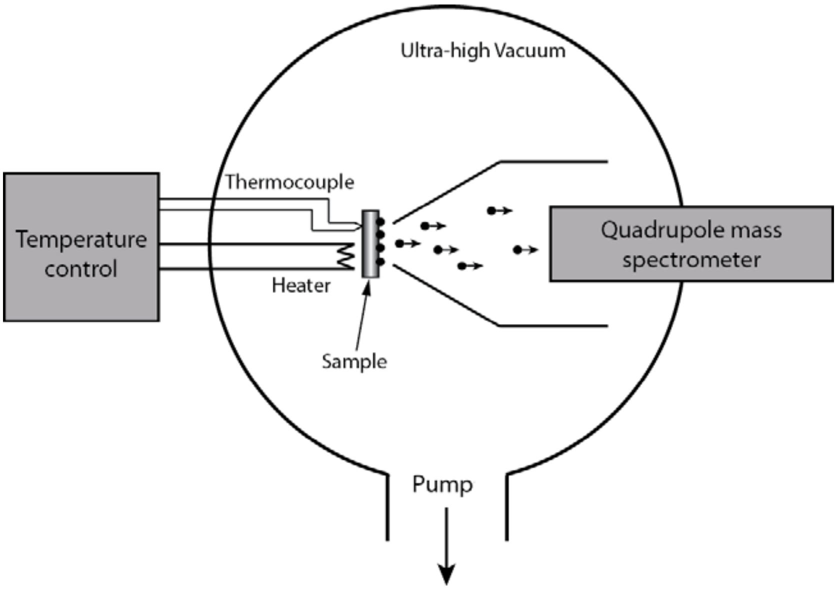

Figure 2.2: Schematic illustration of TDS with a Feulner cup.

2.4 Experimental setups

The scientific results presented in this thesis have been achieved in two labs at Empa, the Swiss Federal Laboratories for Materials Science and Technology in Dübendorf, where each sample can be prepared and characterized *in-situ* under UHV conditions. All experiments in chapter 3 and the TDS in chapter 4 were carried out in the 'ESCA lab', and the rest in the 'RAIRS lab'.

2.4.1 ESCA lab

The ESCA system is a two-chamber UHV system (Shown in Figure 2.3). The sample (Figure 2.3b), a single crystal in this case, has been spot-welded and clamped by two tantalum wires onto the manipulator and was in good thermal and electric contact with the copper block and heating bands from the manipulator. In addition, a type K thermocouple has been spot-welded on the side of the crystal for precise temperature detection and control (from ~80 K to ~1500 K). In order to reach different experimental techniques, the manipulator allows manual sample rotation and translation. The preparation chamber is equipped with low energy electron diffraction (LEED) optics, a quadrupole mass spectrometer and a sputter gun for standard sample cleaning with Ar ionized gas. A differentially pumped evaporation cell has been mounted behind a gate valve and can be inserted into the chamber during molecular deposition. A commercial alkali getter has been mounted for alkali metal co-deposition. A photoelectron spectrometer from Physical Electronics and a Mg/Al dual x-ray source has been installed in the XPS chamber. The two chambers can be pumped separately via the ion pump and the turbo pump with the base pressure below 10^{-5} mbar.

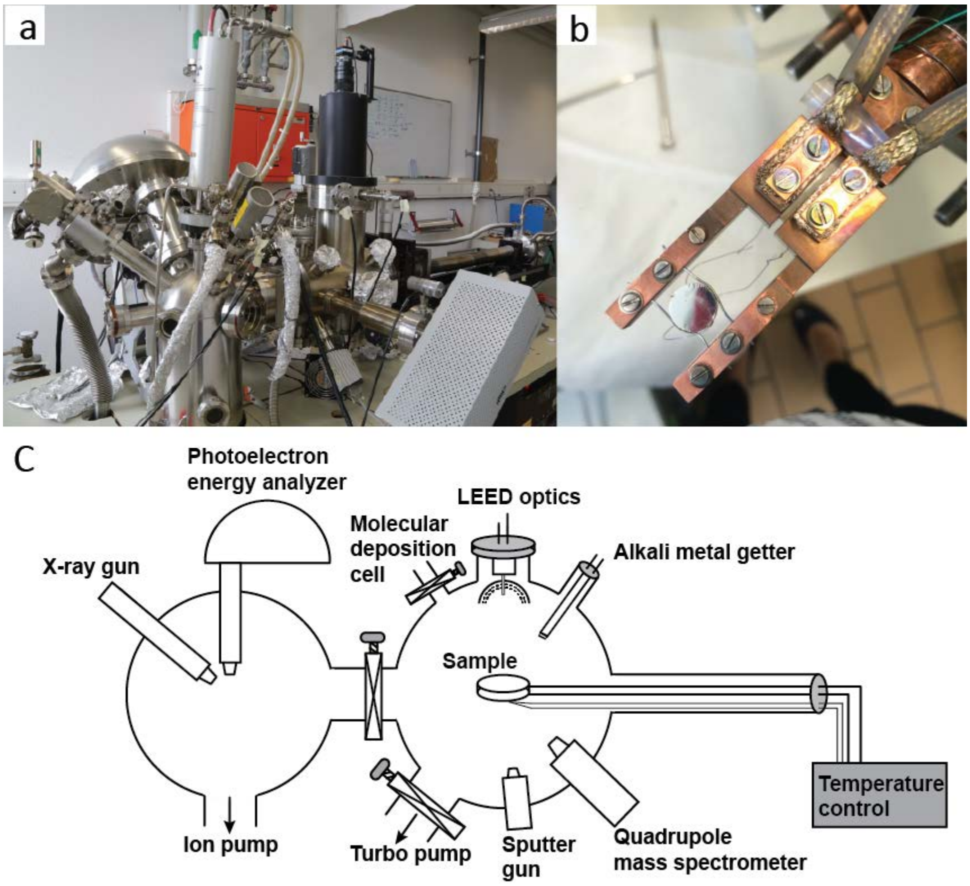

Figure 2.3: Photos and the sketch of the ESCA lab. a) Overview photo of the ESCA lab; b) Photo of a single crystal mounted on the manipulator; c) Sketch of ESCA lab showing the main techniques.

2.4.2 RAIRS lab

RIARS lab is an UHV system consisting of a main chamber and a load-lock chamber (Figure 2.4). The single crystal substrate has been fixed mechanically onto a sample holder, and then clamped onto the manipulator by springs on the sides. Thus the crystal remains in close physical contact to the cooling copper block. The temperature measurement in this case was achieved by physical contact to a type K thermocouple imposed by the springs mounted on the manipulator. The sample holder allows electron bombardment for heating from the backside of the surface. The sample holder also permits *in-situ* sample transfer between the main chamber and the load-lock chamber. As for the ESCA lab, the manipulator allows manual translation and radial rotation of the sample in the main chamber. The chamber is also equipped with a STM (Specs Aarhus 150, incl. a Pt/Ir tip), a quadrupole mass spectrometer housed in a Feulner cup, XPS and a reflection absorption infrared spectrometer (RAIRS). Samples were prepared by using standards methods, such as Ar ion sputtering of the single crystal surface, annealing, molecule deposition and e-beam-heated metal co-deposition. The base pressure of the system was 2×10^{-10} mbar.

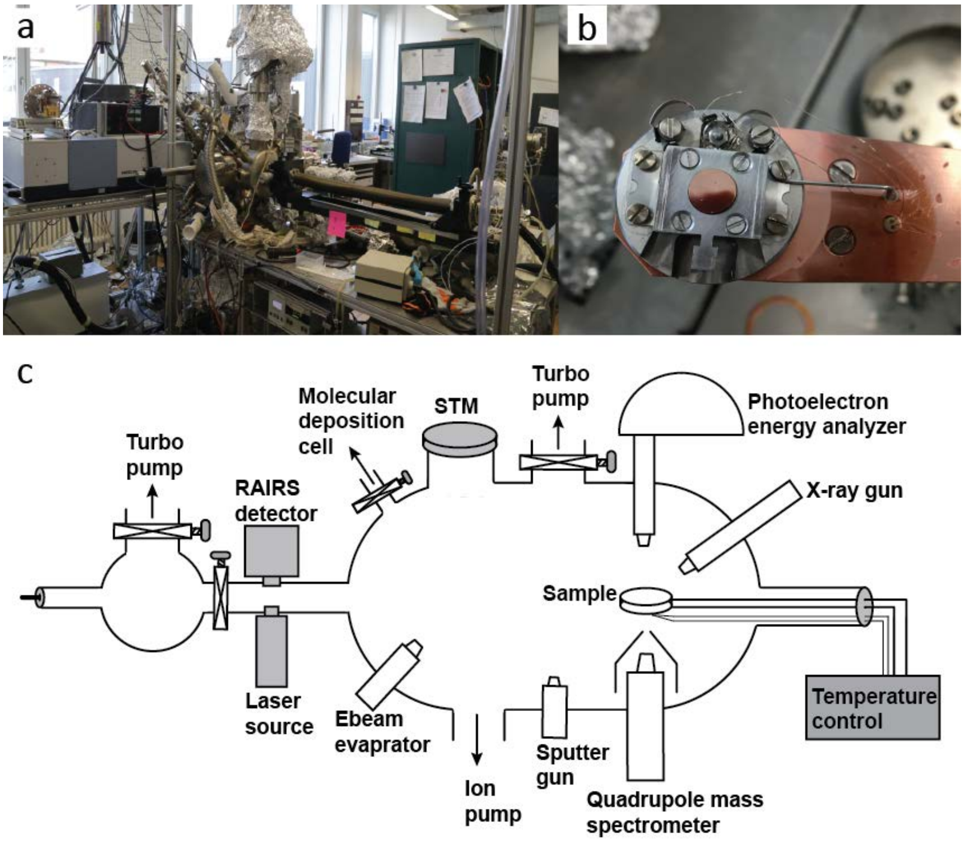

Figure 2.4: a) An overview picture of the RAIRS lab; b) The photo shows a single crystal fixed on the sample holder, mounted on the manipulator; c) A sketch of RAIRS system. Notably, the location and orientation of each technique shown in this sketch does not precisely correspond to the realistic case in the system.

Chapter 3 Metalation of corannulene with alkali metals: thin film syntheses on a Cu(111) surface

Corannulene, a typical Buckminsterfullerene fragment (so-called buckybowls), is a PAH molecule with the chemical formula $C_{20}H_{10}$ [45,46]. Its molecular structure is shown in Scheme 3.1. It has a pentagonal ring in the center, fused with five benzo moieties. Thus it renders a five-fold rotational symmetry, which is incompatible with any periodic crystal lattice [47]. This character of corannulene alone makes it an interesting material to study it on surfaces. Interestingly, the corannulene molecules show on a Cu(111) surface a tilt to avoid C_5 symmetry and are packed in a (4 × 4) long-range ordered superlattice [48,49]. A similar tilt was observed on Cu(110) [50]. Reports also show that the self-assembly of corannulene is dominated by reversible phase transitions at defined temperatures, suggesting an entropy-controlled 2D crystallization process [49], as well as inducing a pronounced charge redistribution at the metal surface upon adsorption [51].

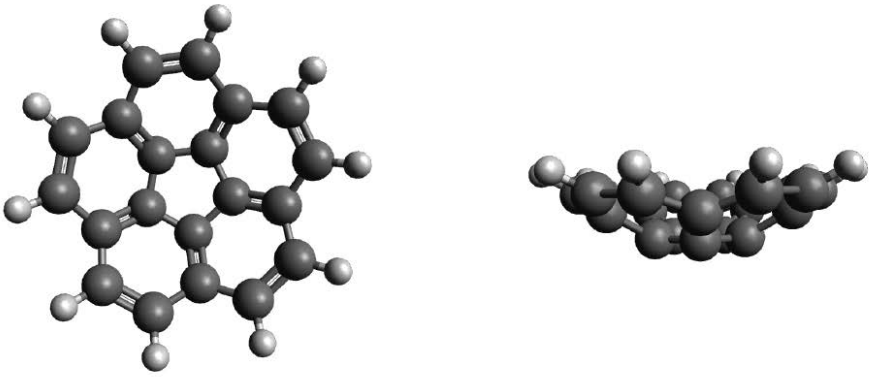

Scheme 3.1: Ball-and-stick model of corannulene

Starting in 1991, it has been reported experimentally that intercalating C_{60} crystals with alkali metals in bulk samples induces superconductivity with transition temperatures as high as 39 K [52,53]. Later, picene, a wide-bandgap semiconducting PAH, was found to exhibit superconductivity when intercalated with potassium, with transition temperatures of 7 K and 18 K, depending on the metal content [54]. Similar to C_{60} fullerene, corannulene is a strong electron acceptor [55]. Nuclear magnetic resonance spectroscopy studies in solution suggested that, each corannulene molecule can intercalate up to 5 alkali metal ions, *i.e*. Li [56–58], with the help of solvent molecules. Theoretical calculations of electron-intramolecular-phonon coupling by Kato *et al.* predicted that the transition temperature of corannulene monoanion can reach as high as 66 K [59]. It was also shown by Bauert *et al.* [60] that under UHV conditions, upon adsorption on a thick Cs film, submonolayers of corannulene accept 4 electrons per molecule from Cs into the two degenerate lowest unoccupied orbitals. Further annealing of thick layers of the molecules together with cesium film leads to the formation of a chemically stable compound film, consisting of corannulene quadruple anions and Cs cations.

Here in attempt of achieving the stable sandwiched compound consisting of corannulene and alkali metals, *in-situ* experiments concerning potassium and lithium have been conducted. XPS and TDS have been used in order to study the stoichiometry and thermal stability of alkali metal – corannulene compound.

3.1 Chemistry of corannulene with potassium on the Cu(111) surface

In order to achieve pure potassium films, potassium getters from Saes Getters were used. They were easy to handle and reliable to produce alkali metal thin films in UHV conditions. The potassium getter was spot-welded on a feedthrough and inserted into the UHV chamber. By applying a current up to its activation current beyond a defined threshold current, pure alkali metal, *i.e.* potassium vapor in this case, can be released from the getter, and deposited onto the sample placed directly facing the getter.

To degas the potassium getter, degassing currents starting from 1 A to 5 A with steps of 0.2 A were applied. The final pressure of the system during degassing at 5 A was below 5×10^{-9} mbar. During evaporation, the potassium getter was applied with an evaporation current I_a and pre-heated for a time t_p to achieve a stable potassium flux. Then a single crystal Cu(111) sample was placed directly facing the getter slot for an evaporating time t_e.

The difficulty with our setup using this Saes getter was that the thickness of evaporated potassium metal at the same applied current was not perfectly linear with the evaporation time, because within the considerable preheating time t_p, the evaporating rate is increasing slightly due to the increasing temperature. And also, the fairly slow process to move the sample manually to its evaporation position from a certain position far enough in the same UHV chamber where the sample will not be contaminated while pre-heating the getter, can cause minor inaccuracy. In our setup, the I_a was usually set to 4.8 A, t_p was 3 min, and the pressure in the UHV chamber during evaporating remained always below 3×10^{-9} mbar.

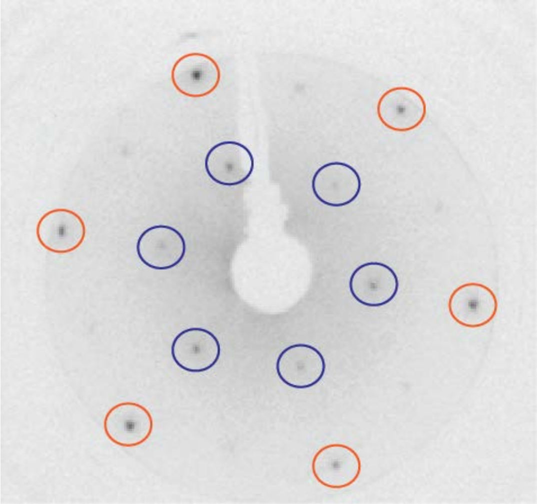

Figure 3.1: LEED pattern of K overlayer on Cu(111) at 66.1 eV. Spots circled orange are the Cu substrate diffraction pattern, while spots circled in blue are diffraction pattern from the potassium p(2×2) overlayer.

The (111) surface of the fcc copper single crystal was used as substrate here. An initial ordered overlayer of potassium atoms on Cu(111) has been reported to have the surface structure of p(2x2) [61]. The corresponding LEED pattern is shown in Figure 3.1. Here the initial layer with ordered p(2×2) structure is defined as 1 monolayer (ML), equivalent to ¼ of the number of (111) copper surface atoms of 1.768×10^{19} m^{-2}. No ordered overlayer LEED pattern can be observed if the coverage of potassium is larger than this initial layer [61]. The excess of monolayer of pure potassium desorbs from the copper surface at room temperature. So cooling of the substrate is required during deposition of potassium in order to get a thick potassium metal layer, as verified by the TDS (Figure 3.2a). The exact coverage can be determined by comparing the XPS peak areas of K and Cu after Shirley background subtraction and division with their atomic XPS sensitivity factors for the spectrometer used. In this way, the K coverage could be related to the LEED calibration of 1 ML. (Figure 3.2b). It can be seen, that the coverage of potassium on the surface was moderately linear with evaporation time. A reason of the slight non-linearity at larger coverage time could be due to the attenuation of Cu signal at higher coverages. The potassium coverage saturated at roughly ~1 ML when the Cu crystal was kept at room temperature. This also shows that the (2 × 2) indeed represents a potassium monolayer and that the adsorption energy is substantially lowered above the 1 ML coverage. Note that alkali adsorption induces substantial surface dipoles and work function decrease on metal surfaces due to charge transfer to the substrate [62].

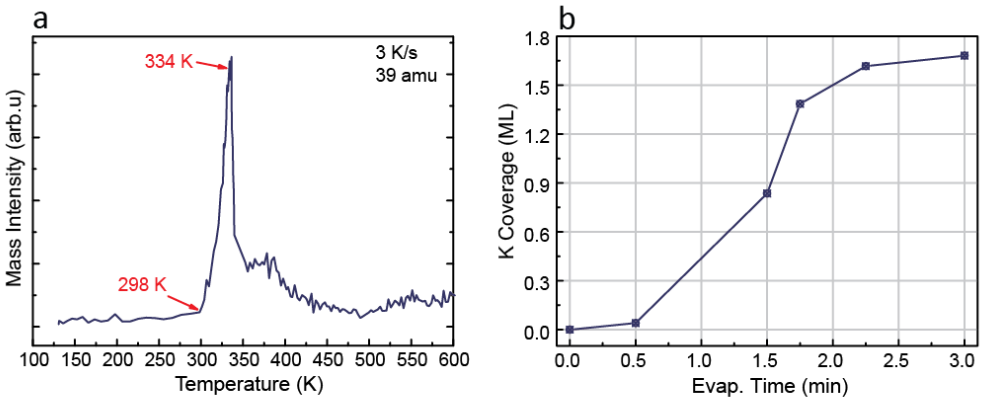

Figure 3.2: a) TDS of approximately 20 ML of potassium deposited on Cu(111) kept at 90 K. Potassium starts to desorb at 298 K; b) K coverage versus evaporation time on the Cu(111) surface at 295 K. Evaporation current of the potassium getter was 4.8 A.

The procedure of making potassium/COR films on the Cu surface was as follows: Cu(111) was cleaned by sputtering with ionized Ar gas (ion current is around 3.5 µA) for 60 min and annealed at 600°C for 4 min. The cleanness of the sample was verified by XPS. Potassium was evaporated by pre-heating the potassium getter for 3 min and subsequent evaporation on to sample for a certain time t_e while the substrate was kept at around 90 K. The evaporation current was 4.8 A. Then COR was evaporated on top of the pure potassium layer. At last, the sample was annealed to a certain temperature for at least 10 min and C1s, K2p, and Cu2p XP spectra were acquired.

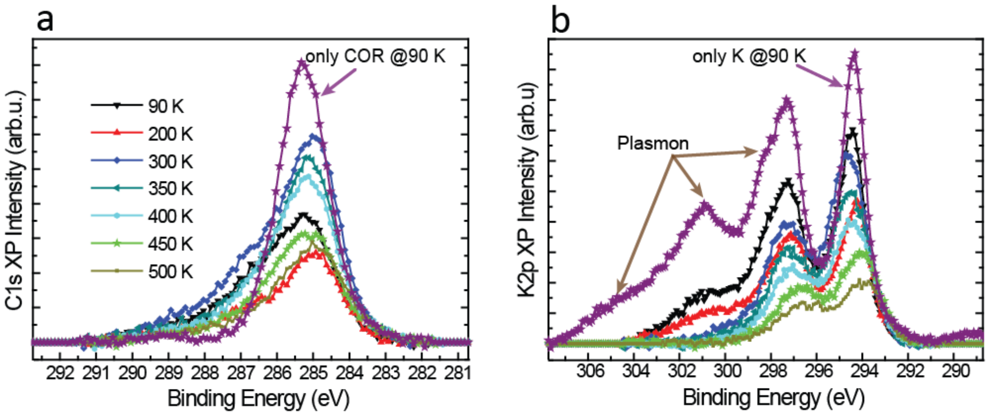

Figure 3.3: K2p and C1s XP spectra of the sample when annealed to different temperatures. Evaporation time for COR and potassium is 30 min and 3 min respectively. Shirley background has been subtracted. The data points in purple in each graph are acquired either with only potassium or with only corannulene on the copper substrate.

Fig. 3.3 shows representative K2p and C1s XP spectra from the same sample with corannulene and potassium layers annealed to different temperatures, with the corannulene molecular cell kept at 105 °C and for 3 min. A Shirley type background has been subtracted. The two peak positions of K2p at ~294 eV and ~296.5 eV both shifted slightly towards lower binding energy along with higher annealing temperatures. Yet the C1s peak did not show a clear shift at different temperatures. For about 60 ML pure potassium on Cu(111), the K2p region showed a clear shoulder and an additional peak at

301 eV. This is a plasmon excitation in the metallic potassium film and causes a lower kinetic energy of the outgoing photoelectron [63]. It was quenched significantly when the corannulene layer was deposited, and disappeared at higher annealing temperatures. Compared to the spectrum acquired with only COR evaporated in the same condition on the same sample, the C1s spectra with both COR and K have shown much broader peaks, probably indicating that the sample heterogeneity.

Table 1 Atomic composition (number of potassium or copper atoms per COR molecule as detected by XPS) on COR (105°c-30min)/K(4.8A-2min)/Cu(111) sample at different annealing temperatures. Due to the surface sensitivity of XPS, the intensity of the Cu signal with respect to the C1s signal was a measure of the COR film thickness.

T_a	K	Cu
90 K	5.7	3.2
300 K	4.8	4.0
350 K	4.6	3.7
400 K	4.3	4.1
450 K	3.5	11.7
500 K	3.8	11.7

The calibrated composition ratio of each element is given in Table 1. Since the COR has 20 carbon atoms per molecule, for the convenience in comparison of potassium versus molecule, the ratio here is always shown as potassium/copper atom per COR molecule. After deposition at 90 K, 6 potassium atoms per COR molecule are observed in average. It is already known that at RT, COR forms a (4 × 4) overlayer on the Cu(111) surface [51]. Thus this (4 × 4) overlayer is defined as 1 ML of COR on Cu(111). So with this definition, by comparing the K2p and C1s signal intensities of this sample, there are at least 40 ML of molecules and 60 ML of potassium. Due to the attenuation of the Cu2p XP signal in such a thick layer, this thickness is most likely an underestimation. Once annealed to 200 K, the ratio per COR molecule of each element fluctuates slightly. This means no desorption from the surface is observed. Although the single components desorb at 300 K from their multilayers, yet multilayer thickness of both molecules and potassium were still observed. Considering that COR on copper at RT can only be monolayer rather than multilayer [64], so does potassium, it can be concluded that, the potassium and COR can stabilize each other on copper surface by forming a compound. This has been verified by a TDS experiment monitoring mass 39 during heating (Figure 3.4). Two peaks, representing potassium desorption were observed. As for the clean potassium layer experiment, a peak at 341 K reveals again potassium multilayer desorption. In particular, the zero order desorption peak shape (the exponential increase and the abrupt decrease of desorption rate at the high temperature side) is indicative for multilayer desorption.

A second peak at 490 K is too high in order to be explained this with regular potassium desorption from the monolayer (Figure 3.2a). It is most-likely due to potassium released from the decomposed COR-K compound at that temperature. An analysis of all XPS annealing experiments (Appendix i) for a temperature between multilayer desorption and decomposition peak, *i.e*. 400 K, results in a K/COR ratio of 4. Hence it can be concluded here that, like in the case of cesium, COR forms a tetraanion. In analogy to Li and Cs, it is likely that four atoms are sandwiched in between two bowl molecules.

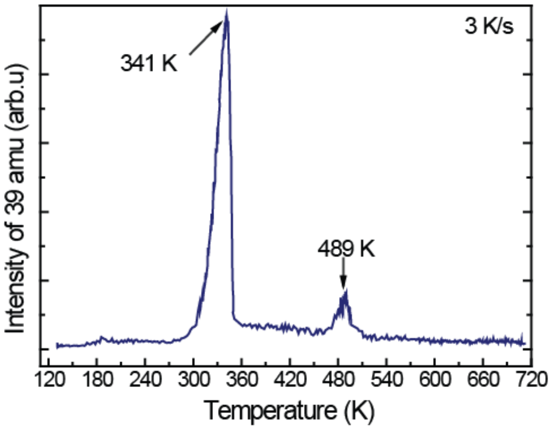

Figure 3.4: TDS of 39 amu, *i.e.* potassium desorption after co-deposition of K and COR. Evaporation time for COR and potassium is 30 min and 3 min, respectively. The heating rate during desorption was 3 K/s. Two desorption peaks are observed at 341 K and 489 K.

Notably, there is always an O1s signal after heating up to 300 K, suggesting a contamination of the sample. Yet the origin of the O element is not known. A guess would be O is taken from residual CO in the UHV system at low temperatures and plays a role in the K-COR compound formation process, since its content is always about 0.5 O per COR.

3.2 Chemistry of corannulene and Li as thin films on the Cu(111) surface

As indicated above, these experiments were motivated by the question if it is possible to synthesize a COR_2-Li_5 sandwich compound, as claimed in [56–58], or if again an exclusively tetraanionic compound is possible. As will be shown below, conclusive COR-Li chemistry cannot be derived from this *in-vacuo* synthesis approach.

The experiments were carried out with a similar set-up as used for the K/COR chemistry. Li was evaporated onto the surface using a Li SAES getter. In these experiments, the evaporation current was set to be 7 A, unless stated otherwise. Cu(111) was used as the substrate. The getter was degassed using an evaporation current untill the O1s XPS peak cannot be detected on a Li/Cu sample at low temperature.

TDS of Li on Cu(111) shows that Li atoms desorb at about 630 K (Figure 3.5.). Hence, Li adsorption does not necessarily require cooling of the substrate. Yet deposition at low temperature shows a substantially higher amount of Li on the surface, suggesting that at low temperature, Li atoms have a higher sticking coefficient onto the Li/Cu surface. In order to grow COR multilayers, the substrate was always cooled to 90 K (using liquid nitrogen as coolant) during Li and molecule deposition.

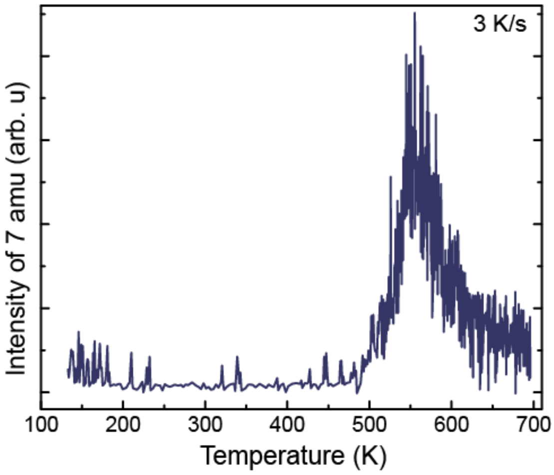

Figure 3.5: TDS of Li on Cu(111) surface, ramping rate was 3 K/s.

The XPS atomic sensitivity factor of Lithium is very small, *e.g.* compared to that of carbon and that of copper. The XPS signal of Li cannot be effectively distinguished from the background noise when there is only a thin layer on the top surface. So a thick layer is needed in this case. Figure 3.6 shows a typical XP spectrum and fitting of pure Li atoms on Cu(111) surface at 90 K. No LEED pattern of the Li ad-layers was ever observed, at low or room temperature. There were about 57 ML on this sample. The Li1s peak position on Cu is 55 eV with a shoulder at higher binding energy.

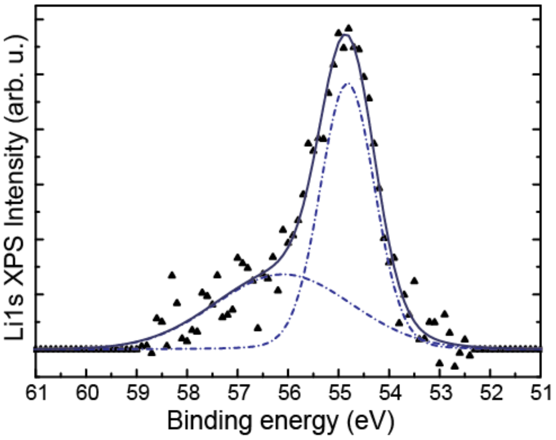

Figure 3.6: Spectrum and fitting of the Li 1s XPS peak on Cu(111).

The similar procedure as for the potassium experiments was applied in this case, yet with much thicker layers, due to the low sensitivity of Li in XPS. Because of the high Li desorption temperature the Li films were shortly annealed to 350 K, speculating that this will produce homogeneous Li films. This step was not applied when COR was deposited prior to Li.

Figure 3.7 shows typical XP spectra series at different annealing temperature. In set A, Li was evaporated first, and in set B, COR was evaporated first. All the other conditions remain the same. Table 3 shows the atomic ratio of Li, C, Cu and O on the sample in these two series of experiments.

Table 2 Amounts of Li, Cu and O per molecule for Cor/Li/Cu(111) and Li/Cor/Cu(111).

	A: COR (110 °C, 30 min) + Li (7 A, 5 min) (Li first)			**B: Li (7 A, 5 min) + COR (110 °C, 30 min) (COR first)**		
	Li	***Cu***	***O***	***Li***	***Cu***	***O***
90K (only one component: Li or COR)	2.4	1	-	-	2.4	-
90K (after annealing to 350K for 2min)	2.4	1	0.1	-	-	-
90K (with both COR and Li)	8.5	1.6	0.6	19.6	1.3	-
300K	13.7	2.0	0.6	14.7	2.6	0.7
350K	-	-	-	14.8	2.4	0.7
400K	20.1	2.6	0.6	-	-	-
450K	-	-	-	14.2	2.7	0.7
500K	19.8	2.2	0.6	-	-	-
550K	-	-	-	15.7	3.9	0.8
590K	19.4	3.5	0.7	-	-	-
650K	10.7	4.1	0.7	-	-	-

The annealing results for the two groups show different behaviors. When the Li is covered by the corannulene at initial 90 K (group A), the Li1s XPS peak is located at 54.1 eV. An additional peak at a higher appears when annealed to 300 K. This results in a very broad Li1s peak at this temperature. The shift is completed when annealed to 400 K and beyond, as only one peak at 56 eV is shown. This shifting suggests a chemical reaction on surface. However, when initially Li is evaporated on top of the molecules, there is no large peak shift regarding different annealing temperature. The peaks at 90 K and 350 K are a bit broad but there is always a major peak located at 56 eV, and growing more and more defines as the annealing temperatures go higher. This suggests that the reaction which happens in group B takes place already at 90 K. This is verified by the shifting of C1s XPS peaks.

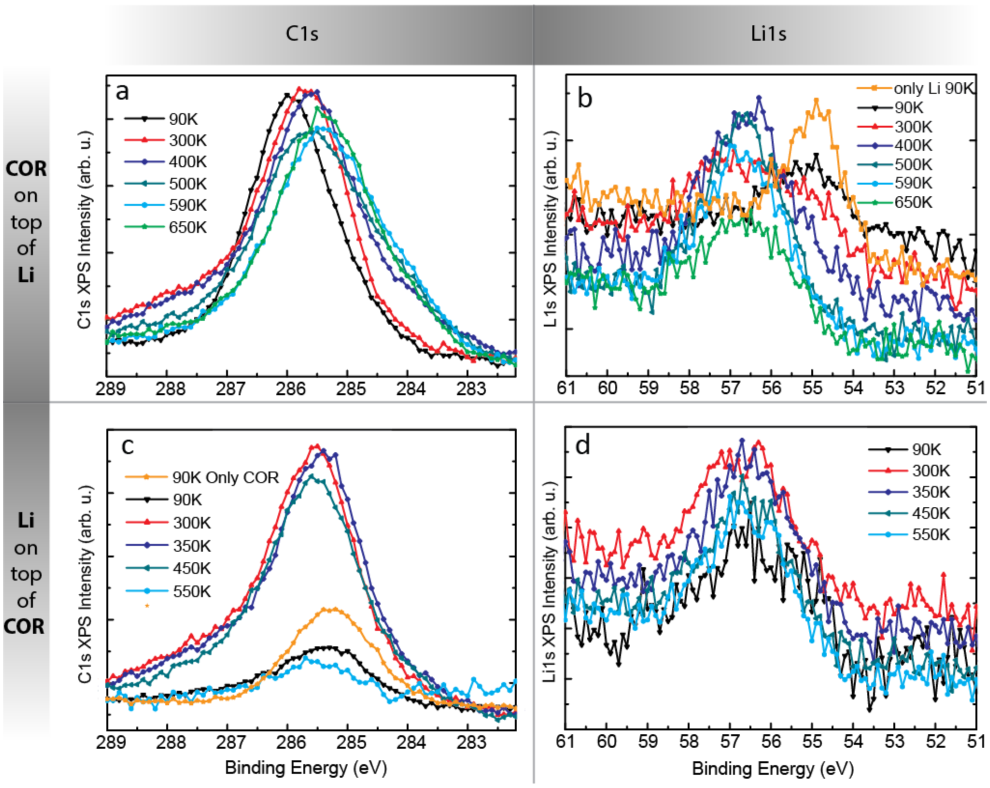

Figure 3.7: XP spectra of two samples, with COR evaporated on top of Li or Li on top of COR, respectively.

The qualitative calibration shows that the initial ratio of Li:COR is, in both cases, larger than 4 or 5, which is the expected value of Li/COR sandwich structure. From TDS experiments, it is known that a pure Li layer does not desorb from Cu(111) surface at room temperature yet COR does. This agrees with our calibrated atomic ratio in the group A and B. In A, the thick Li layer covered by a thick COR layer intermixes with the molecule layer when annealing from 90 K to room temperature, so XPS, as a surface sensitive method, shows a growing Li signal. This ratio remains around 19-20 until annealing as high as 650 K and decreases to about 11. This result also agrees with the previous result that, Li desorbs from Cu(111) at about 620 K. In group B, the ratio of Li:COR stabilizes at about 15 up to 550 K.

In both cases above 300 K, there exists a small O1s peak, with atomic ratio of about 0.6 and 0.7. This contamination cannot be ruled out and its origin is not known.

Since COR desorbs from the Cu surface at a much lower temperature than that of a Li layer, an considerably thick molecular layer is needed to give the initial ratio of Li:COR lower than 4, especially considering that the atomic sensitivity factor of Li is low. So a COR-first procedure is used. After COR evaporation, there is barely any Cu2p XP signal from the surface. Further results are shown in the Appendix ii. A typical Ci1s and Li1s XPS peaks from these experiments are shown in Figure 3.8.

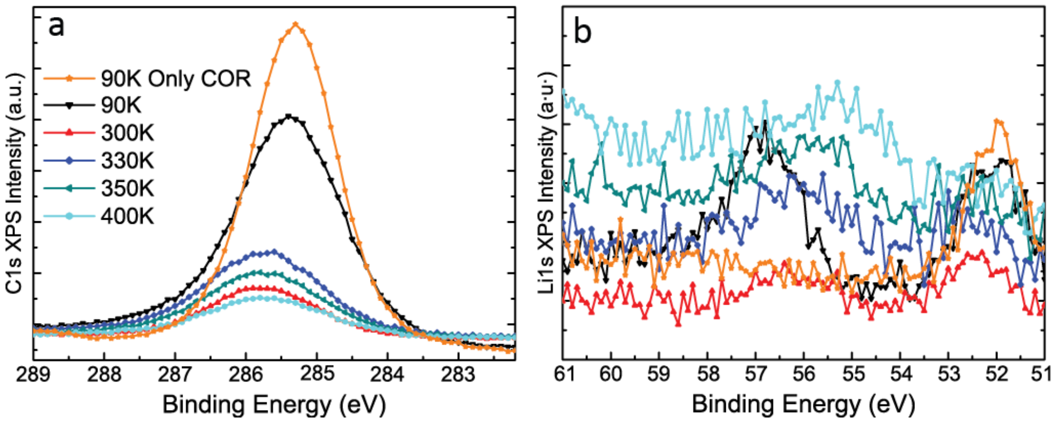

Figure 3.8: XPS of Li1s and C1s regions from annealing series with thick layered COR and Li. The orange plot is the data acquired with either COR or Li on surface. The intensity of spectra is rescaled for best visibility. The peak in b) at 52 eV is a C1s replica (see text).

From the data above, a peak at 52 eV in Li1s region is observed after COR molecules are evaporated. It remains its intensity at 90 K after Li is evaporated and decreases when annealed. It was not observed on clean Cu. Its binding energy is too low to be Li (normally ~55 eV) and it is correlated to the carbon concentration on surface. It is a C1s replica caused by a small amount of Al K α X-rays produced in addition to the desired Mg K α line. The difference between the photon energy of Al K alpha (1486.7 eV) and Mg K alpha (1253.7 eV) is -233.0 eV. So for the C1s peak, the Al K alpha energy will result in a C1s replica at 285 eV – 233 eV = 52 eV. Therefore, for the Li concentration shown in Table 4, this 52 eV peak is not considered. Due to the extremely small Li sensitivity for XPS, the Li1s peak is barely seen after annealing, thus, the calibration based on XPS has a large error bar.

The ratio is not reproducible in each experiment and no stable complex/compound is found. It is likely that COR molecules desorb from surface at about 320 K rapidly yet Li does not, so that the sandwich structure formation as stable compound is above this temperature.

Notably, there is always an O1s peak after annealing to 300 K and above, just as in the K case. Since the O1s is not there before the annealing at low temperature, our conclusion is that this O comes from the degassing of the hot surfaces in the UHV system during annealing. Since alkali metal is so active to oxidation, the degassing of the surfaces becomes critical in this case.

In order to achieve an adequate molecule quantity for the formation of a stable compound, another procedure was carried out to try to get stable compound. COR and Li were evaporated onto the surface while keeping the substrate at 90 K, then the sample was annealed to 330 K for 4 min and cooled down for XPS, then warmed again and kept for 330 K while evaporating additional COR to the surface for 20 min. The result is shown in Figure 3.9.

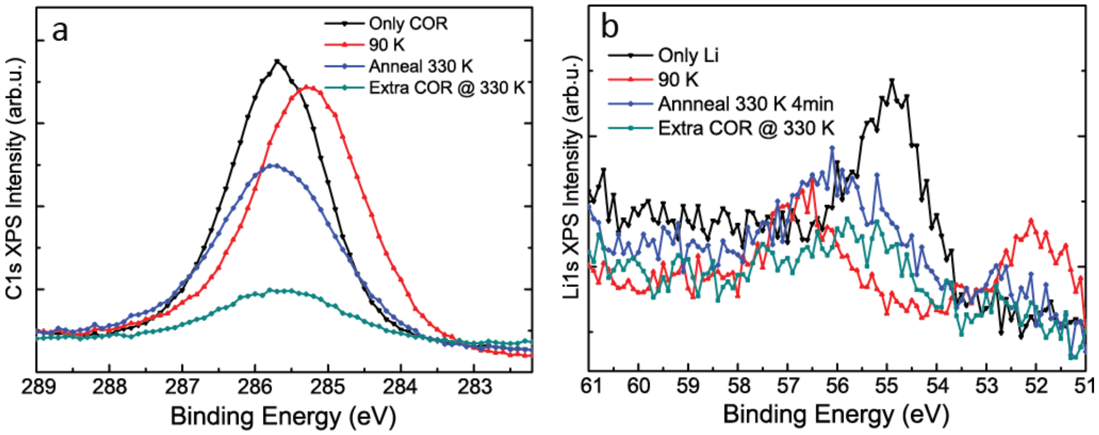

Figure 3.9: XPS of a sample consisting of thick layers of COR and Li being annealed and subsequently more COR evaporated. Spectra were measured at each step of the sample preparation. The spectrum in red is thick layer of COR and Li evaporated at 90 K. Then the sample was annealed to 330 K. The spectra in blue and in green are the result before and after evaporating additional COR onto the 330 K substrate respectively. The signal at 52 eV is a C1s replica (see text).

By comparing the XP spectra of native COR and COR with Li at 90 K, a down-shift together with peak broadening of the C1s peak can be observed. Meanwhile, the Li1s peak has an up-shift from 55 eV to 56.6 eV. Once annealed to 330 K, no matter before or after evaporation of additional COR molecule, no chemical shift of C1s or Li1s is observed.

Table 3 The atomic ratio of the samples shown in figure 3.9 per molecule

	Li	Cu	O
90 K	2.7	-	-
Anneal 330 K 4min	5.0	2.5	1.4
More COR at 330K	12.6	2.4	0.6

From figure 3.9 and table 5, it can be proved that deposition of additional molecules does not lead to a stable compound.

3.3 Conclusions

Adding Li to COR results in a downshift of the C1s signal by about 0.8 eV. In turn, Li embedded in COR has a ~1.5 eV higher binding energy compared to Li on Cu. The same trend can be observed also for potassium. This shows that there is significant charge transfer from the alkali atoms to the molecules and indicative for compound formation. In the case of potassium it has been shown that a stable compound is formed at 400 K with 4 potassium ions per COR molecule. In the case of Li no stable compound/complex could have been prepared, which was most likely because of the choice of the initial experimental conditions. The major difficulty was the high thermal stability of the Li layer. Hence, excess Li could not be removed without destroying the entire sample. When working with Li thin layers the lack of XPS sensitivity did not allow proper analysis of the stoichiometry. High sensitivity XPS would be available in Synchrotron-based experiments, in which, beside high brilliance of the source, resonant XPS is available by tunable photon energy [65].

Chapter 4 Self-assembly and metal coordination of surface-adsorbed pyrphyrin molecules

4.1 Metalation on Cu(111)

Surface-adsorbed macrocycles, such as porphyrins or phthalocyanines, present interesting platforms to study physical and chemical phenomena at interfaces, as well as potential materials for various applications at the nanoscale. The primarily planar macrocycles are particularly remarkable because they can coordinate a metal ion in their center, which makes them ideal on-surface model systems to study coordination chemistry [66–68]. In addition, the central metal ions can attach an axial ligand at the open site opposite to the surface [69,70]. Notably, this phenomenon of porphyrin-derived 2D layers holding different transition metals has been reported to process catalytic properties for water oxidation [71]. An alternative to the deposition of metal containing macrocycles is to achieve coordination of metal *in-situ* directly in UHV using metal atoms. This process is called metalation. The metalation is achieved either via adatoms from the substrate surface or by subsequent deposition of the desired metal [72–74,67,68]. In this chapter, on-surface metalation of the porphyrin-like molecule pyrphyrin (2HPyr, Scheme 4.1) is reported.

In contrast to molecules from the tetrapyrrole family, *i.e.* porphyrin or phthalocyanine, the pyrphyrin macrocycle consists of four fused pyridines instead of pyrrols [75,76]. Specifically, two *2,2'*-bipyridine subunits are bridged by cyano-methylene units to form a plane consisting of two iminic (=N-) and two pyridinic (-NH-) nitrogen atoms. After dehydrogenation in the core of free-base 2HPyr, the planar, tetradentate pyrphyrin ligand can coordinate ions such as Zn(II) [77,78], Mn(III)Cl [79], and Co(II) [76]. The formation of CoPyr has been also achieved on the Au(111) surface in presence of supplemented Co adatoms [80] provided by e-beam evaporation. In solution, CoPyr-derived complexes have been shown to catalyze the reduction of water under the illumination with light [76].

Based on the surface chemistry of cyano-functionalized molecules reported previously [81–84], it is anticipated that transition metals can also coordinate at the cyano groups. Such coordination at functional groups pointing away from the molecules generally leads to the formation of highly-ordered extended organometallic networks [85].

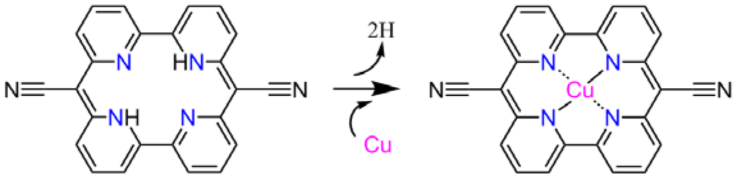

Scheme 4.1: Scheme of 2HPyr and its self-metalation to CuPyr

2HPyr (sub)monolayers with the coverage of approximately 1 ML were thermally evaporated from a Knudsen cell onto the Cu(111) substrate. Here 1 monolayer (ML) is defined as the most densely-packed layer of Pyr molecules on the Cu(111) surface without any molecules in the second layer. The evaporation temperature of the molecules was 330 °C. The molecular coverage was obtained from XPS by comparing the intensities of $Cu2p_{3/2}$ peaks and C1s peak calibration of the absolute coverage using STM.

For 1.0 ML of 2HPyr deposited on Cu(111) kept at room temperature (RT, 295 K), XP spectra (Figure 4.1) reveal a N1s signal with two distinctive peaks. Since there are three species of N atoms in each 2HPyr molecule, three peak components, standing for iminic (−NH−) at 400.7 eV, pyridic (=N−, 398.9 eV) and cyano (C≡N, 399.2 eV) nitrogen, have been fitted. These binding energies are consistent with the literature for 2HPyr [80] and free-base tetraphenylporphyrin (2HTPP) monolayers [67,68]. The experimental spectra are consistent with three components in a 1:1:1 ratio, indicating that the molecules were in their native state after evaporation onto the copper surface at room temperature. The cyano- and pyrido- signals are very close in energy and could be also assigned inversely. After annealing to 473 K for 10 min, a narrower N 1s peak is observed which can be decomposed into a N−Cu (398.9 eV) and a C≡N−Cu (399.8 eV) species in a 2:1 ratio [72,82,86,87]. The disappearance of the −NH− signal at the higher binding energy and the emergence of the narrower N1s peak are key features identifying the metalation reaction: through a dehydrogenation process of the two iminic groups in the molecular core, a copper atom has been incorporated in the macrocycle center of the molecule and hence leads to four equivalent pyridic nitrogen atoms. The binding energies agree with previous results on porphyrin metalation on copper surfaces [86] and with CoPyr/Au(111) [80]. Remarkably, the C≡N component shifts towards higher binding energy by 0.7 eV, indicating a significant modification of the cyano groups' chemical environment. A similar N1s peak up-shift has been observed after the coordination of Cu adatoms to cyano groups of a cyanohelicene derivative [82]. Therefore, the shift of the cyano-N indicates that Cu coordination at the cyano groups also occurs for pyrphyrin on Cu(111).

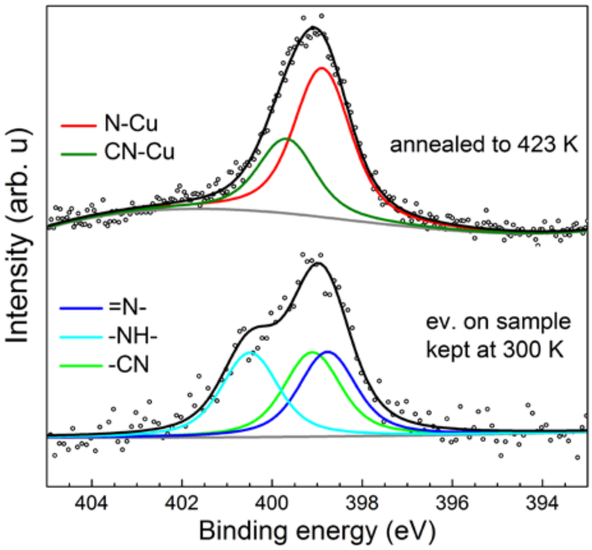

Figure 4.1: XP spectra in the N1s region revealing the metalation reaction of 2HPyr to CuPyr (1.0 ML). After deposition, the N1s signal can be deconvoluted into 3 components, *i.e.* iminic (−NH−, 400.5 eV), pyridinic (=N−, 398.8 eV) and cyano (C≡N, 399.1 eV) nitrogen. The cyano- and pyrido-signals are very close in energy and can be also assigned inversely. The narrower N1s peak observed after annealing can be deconvoluted in N−Cu (398.9 eV) and a C≡N−Cu (399.8 eV) species in the ratio of 2:1. The background of the clean sample has been subtracted.

By measuring the evolution of molecular hydrogen with TDS, further insight into the process of metalation is obtained. During the temperature ramp at rate of 3 K/s, two distinct H_2 desorption maxima α and β were observed at 377 K and 696 K, respectively (Figure 4.2). The spectrum obtained on the clean Cu(111) under identical conditions did not exhibit these features. Based on the observation of the complete metalation after annealing to 423 K using XPS, peak α is assigned to the dehydrogenation of the pyridinic nitrogens during metalation, consistent with the literatures on porphyrin metalation on Cu(111) [68,88,89]. The intense and broad TD peak β is assigned to thermally-induced dehydrogenation at the periphery of the molecules, *i.e.* C-H bond breaking. Such pyrolysis has also been observed for monolayers of tetrapyrrols adsorbed on metal surfaces [86,88,90–92].

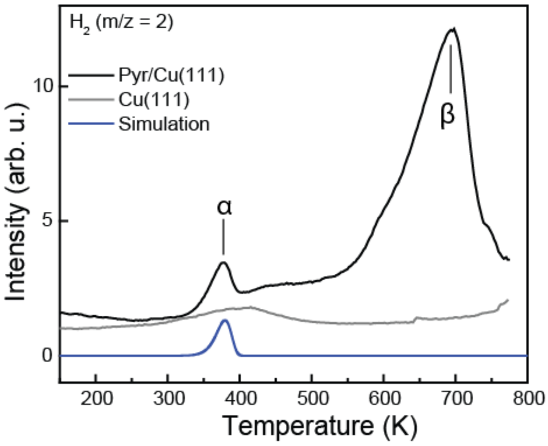

Figure 4.2: TDS for molecular hydrogen (m/z = 2) obtained for 1.2 ML of 2HPyr deposited on Cu(111) kept at 110 K. The heating rate was 3 K/s. Two distinct maxima α and β were observed at 377 K and 696 K, which are assigned to H_2 desorbing during metalation and dehydrogenation of the carbon backbone, respectively. The TD spectrum for the first order kinetics with the attempt frequency v_0 = 10^{15} Hz and an activation barrier E = 113 kJ / mol was numerically simulated (shown in blue).

The energy barrier for the dehydrogenation of the pyrphyrin core and therefore for metalation can be obtained by assuming that the hydrogen recombination to molecular hydrogen and desorption of H_2 are not the rate-determining steps of the entire process. This assumption is justified, because recombinant H_2-desorption on Cu(111) occurs at ~ 300 K [93]. The simulations were performed by numerically propagating the Polanyi-Wigner equation (3) (see introduction of TDS, chapter 2 section 3) [94,95] with a linear temperature ramp. Here, an arbitrary initial coverage θ for the first order kinetics was used. The reaction rate *r(t)* and the coverage θ*(t)* were evaluated step-wise while increasing the temperature T with every step. 10^4 time steps were sufficient, *i.e.* more time steps did not affect the rate. In the case of desorption, *r(t)* corresponds to the TDS signal measured.

For simplicity the attempt frequency v_0 is fixed to 10^{15} Hz, which has been obtained by Ditze *et al.* for metalation of 2HTPP on Cu(111) [89]. The simulated TD signal (Figure 4.2) for the activation energy E = 113 kJ / mol and for the first order kinetics reproduced the maximum temperature and shape of peak *α*. This value is significantly lower than the activation energy for metalation of 2HTPP/Cu(111), *i.e.* 143 kJ / mol [89] and 134 kJ / mol [88] with the same attempt frequency.

As discussed above, 2HPyr on Cu(111) can be transformed into the metalated CuPyr by moderate annealing at 423 K. It can be further transformed by dehydrogenation at the periphery at temperatures of approximately 520 K. In the following, STM data obtained in these 3 regimes is reported below.

Figure 4.3 displays STM images obtained for a 1.05 ML of 2HPyr deposited on a Cu(111) surface which was kept at 295 K (b and c), as well as the clean Cu(111) surface used (a). Under these conditions, the molecules were not metalated, verified by XPS. Using STM, self-assembled domains as well as disordered areas are obeserved. In (b), the streaks along the fast scan direction (horizontal) evidence the partial mobility of molecules in the disordered areas. The hexagonal symmetry of self-assembled domains reflects the symmetry of the Cu(111) substrate. The molecules appear nearly square-shaped with a depression in the center under these scanning conditions. As the cyano groups are not resolved, the exact orientation of each molecule cannot be determined. Some molecules appear fuzzy and roundish, presumably due to thermal rotation. Notably, the appearance of the molecules and their self-assembly pattern are very similar to those of 2HPyr on the Au(111) surface [80].

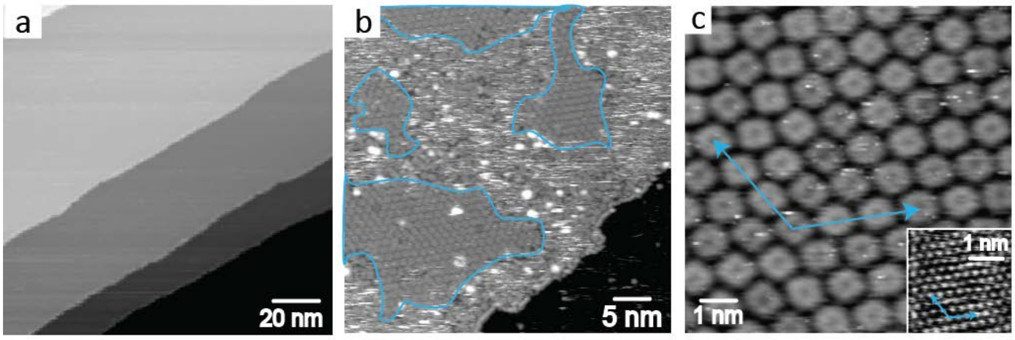

Figure 4.3: STM images of clean Cu(111) (a) and of 1.05 ML of 2HPyr deposited on Cu (111) kept at 295 K (b, c). (a) The large scale image of the clean Cu(111) (1250 mV, 60 pA, 295 K) exhibits extended terraces and smooth step edges; the inset displays atomic resolution (−4.6 mV, −2.9 nA, 295 K). (b) Self-assembled domains of molecules are observed (bordered by blue lines) as well as disordered areas (1277 mV, 20 pA, 295 K). Streaks appear along the fast scan direction (horizontal) in the disordered areas, indicating that the molecules are mobile. (c) Small scale image (940 mV, 20 pA, 295 K) showing the molecules in a self-assembled domain. Blue arrows in the inset in a) and in c) indicate the unit-cells of the substrate and the molecular layer, multiplied 3 times for better visibility.

Figure 4.4 shows STM images of metalated Pyr on Cu(111). The sample has been obtained with 0.7 ML 2HPyr deposited at 295 K, annealed to 423 K for 10 min and imaged at 130 K due to the high molecular mobility at the room temperature. The overview (a) reveals that metalated molecules assemble into two distinctive domains: honeycomb lattice and molecular chains (bordered by a blue line). Such morphology has been also observed for other molecules with two cyano groups attached at opposite sides of the same molecule [81–84]. As Cu ions have been reported to coordinate 4 ligands and form a square planar symmetry [96], as in the case of the core metal center in this molecule CuPyr, there is not enough room for 4 periphery cyano groups pointing into a single coordination site on the surface. Hence a threefold coordination pattern is the result. The similar honeycomb network induced by cyano groups have been also observed [83,97–100]. Some pores of the honeycomb lattice, as marked by blue arrows in (b), are filled with one additional molecule which rotates and has been observed to occasionally migrate from site to site during scanning. This is a consequence of the fact that these additional molecules cannot interact with neighbor molecules via coordinated Cu adatoms at the cyano groups. The dark appearance of the center of the molecules implies the absence of 3d states with predominantly out-of-plane character [101,102], consistent with the presence of a Cu(II)-ion in the center of the molecule.

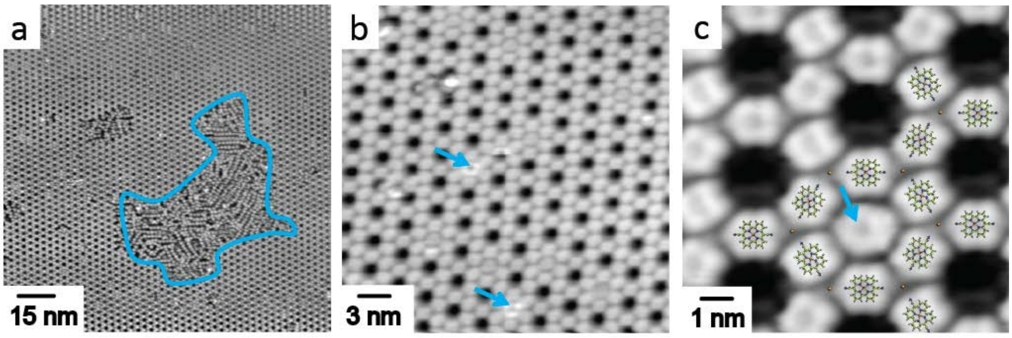

Figure 4.4: STM images obtained for 0.7 ML 2HPyr after annealing to 423 K and measured at 130 K. The large scale image (a) (58 mV, 17 pA) exhibits an extended honeycomb porous network. Small domains with linearly coordinated molecules appearing as chains are also present (domain bordered by the blue line). The detailed assembly is observed in image b) (363 mV, 20 pA) and c) (57 mV, 230 pA). Some pores of the honeycomb lattice are filled with molecules (indicated by blue arrows). The molecules filling the pores are observed to rotate at 130 K. c) displays overlaid CuPyr schemes and Cu adatoms to illustrate the organometallic honeycomb lattice.

Due to the quite robust nature of the honeycomb lattice, acquisition of images with a small bias voltage and a high tunneling current set point became possible. Under these conditions, the STM tip approached closer to the molecule, thereby the intramolecular resolution was increased and it could be tunneled into the in-plane orbitals [103]. Figure 4.5 exhibits a series of STM images obtained at a bias voltage of 57 mV and tunneling currents increasing from 40 pA to ~ 2 nA. At the tunneling current set points above 500 pA, a protrusion corresponding to the Cu(II) ion was visible in the center of the molecules (Figure 4.5d-f).

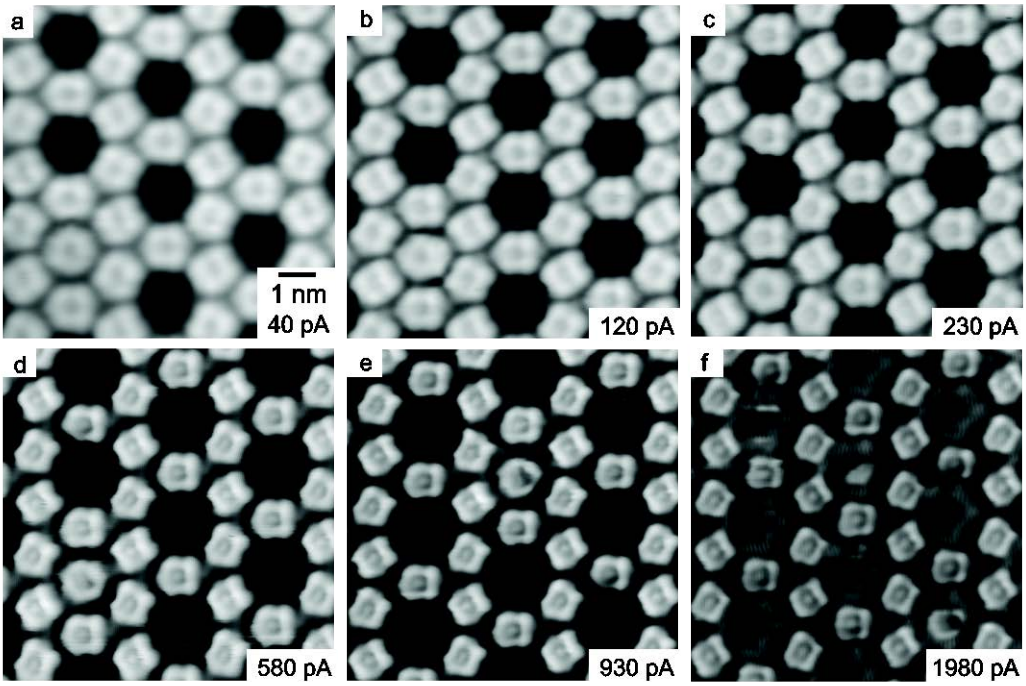

Figure 4.5: STM images obtained for 0.7 ML 2HPyr after annealing to 423 K at different tunneling current set points (tunneling voltage was kept at 57 mV, while varying tunnel set point currents are given in the figure, and all images were measured at 130 K). With the increasing current set points, more intramolecular details were resolved and the molecules appear smaller because the tip

approached closer, leading to a more localized tunneling process. At high current set points (> 500 pA), a protrusion in the central of the molecules can be identified. The images were not acquired from the same area. The scale bar applies to all images.

The third regime identified by XPS and TDS corresponds to molecules which are partially dehydrogenated at their periphery. The onset of this pyrolysis at the time scale of seconds relevant for TDS is at ~ 550 K. Because the sublimation of 2HPyr takes ~ 20 min, the sample was kept at 520 K during evaporation. These conditions were sufficient to observe a significantly different morphology of the dehydrogenated CuPyr molecules. Under these conditions, no self-assembly was observed and the molecules appeared with slightly irregular shapes (Figure 4.6). Such disordered layers and irregular appearance have been also observed previously for tetrapyrrol monolayers on Cu and Ag substrates which were dehydrogenated at the periphery when annealed to 500 to 640 K [86,88,90–92].

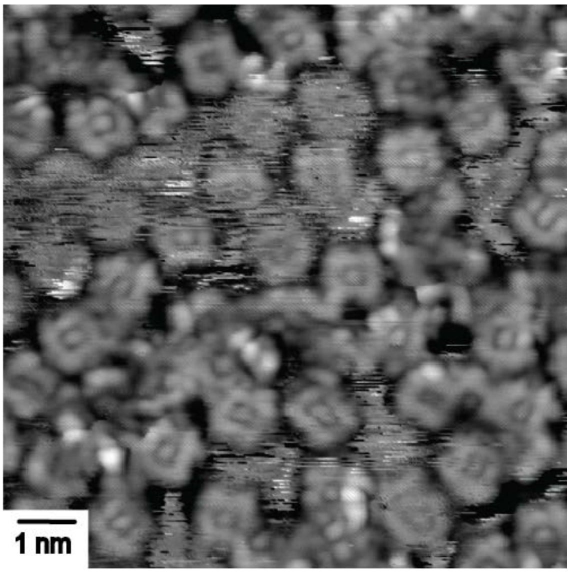

Figure 4.6: STM image (−1 V, −2.8 nA, 295 K) obtained when evaporated onto a sample kept at 520 K, *i.e.* close to the temperature regime where dehydrogenation occurs (0.9 ML). The molecules appear as slightly irregular shapes. No self-assembled layers were observed under these conditions.

Lastly, the direct evidence is also presented here, that the metalation of 2HPyr on Cu(111) proceeds also into the multilayer (Figure 4.7). TD spectra obtained for mass 386 amu (2HPyr) and 447 amu (CuPyr) for ~3 − 5 ML of 2HPyr deposited on Cu(111). The spectra resolve both 2HPyr and CuPyr desorbing at around 550 K from the multilayer as intact molecules. The lower desorption temperature compared to the sublimation temperature is attributed to the less compact packing commonly observed in multilayers compared to bulk [90]. These results are consistent with the literature, where metalation in the multilayer has also been observed for porphyrins [104,105].

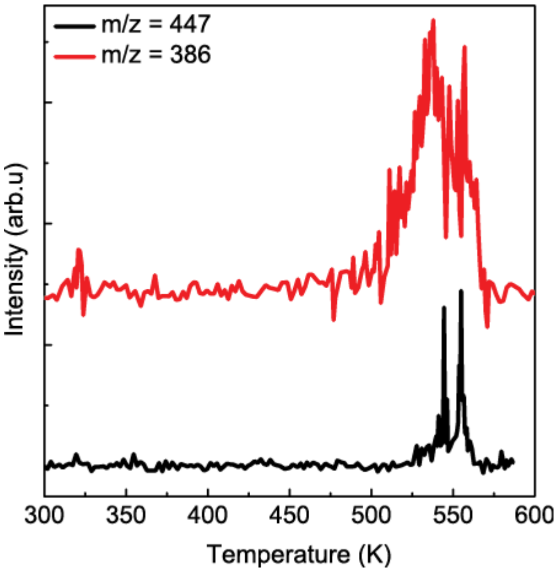

Figure 4.7: TDS for 2HPyr (*m/z* = 386) and CuPyr (*m/z* = 447) obtained on multilayers (~3 − 5 ML) of 2HPyr on Cu(111). The temperature ramp rate was 2 K/s. Both 2HPyr and CuPyr were detected, demonstrating that the metalation can occur in the multilayer. The 2HPyr spectrum was offset for clarity.

4.2 Coordination networks of CoPyr on Cu(111) and Au(111)

In order to further explore the functionality of metal-core of pyrphyrin and its cyano groups' role on metal surfaces, CoPyr molecules are evaporated onto the Cu(111) surface. The evaporation temperature of the CoPyr was 310 °C. The coverage of the molecules on the surface was always quantified by comparing the C1s peak intensity and the surface peak intensity (Au4f or Cu3p peaks), as well as STM images.

At sub-monolayer coverages, the molecules are too mobile at room temperature in order to get conclusive results with STM. Therefore, STM imaging was performed on a liquid nitrogen-cooled sample an at approximately 130 K. STM images of a sample with 0.7 ML CoPyr on the Cu(111) surface is shown in Figure 4.8a. Approximately half of the surface is covered by chains of CoPyr following three symmetry-equivalent directions. On the other half of the surface no long-range order is observed. An image at higher magnification with the intermolecular resolution is shown in Fig. 4.8b. As for the bright core, the four bright pyridine subunits within each molecule are clearly revealed. The center of the molecule appears to be bright to represent Co ions [101,102], consistent with a previous study of CoPyr on Au(111) [80]. This observation shows that no displacement reaction with copper atoms from the substrate has occurred. Because the molecule has a two-fold symmetry and is longer in the direction of cyano groups, the exact orientation of each molecule on these images could be determined by mapping the molecular symmetry. A few assignments are presented by superposition of molecular models with the STM appearance in Figure 4.8b.

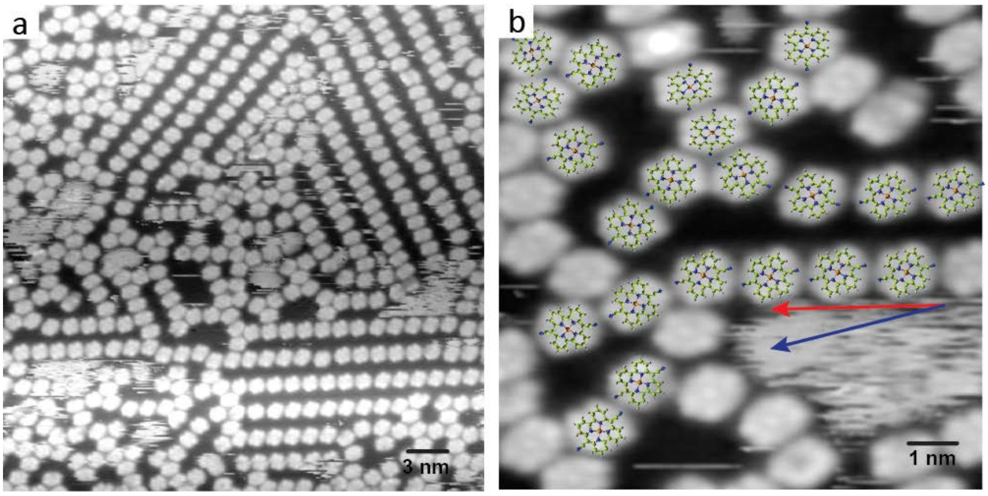

Figure 4.8: STM images of 0.7 ML of cobalt pyrphyrin on Cu(111) surface, measured at 130 K. a) Approximately half of the surface is covered by chains of CoPyr following three distinctive directions. No long-range order of molecules could be observed in the other areas (36.9 nm × 36.9 nm, 911.3 mV, 50 pA). b) Magnified image (10 nm × 10 nm, 911.3 mV, 40 pA) shows that each molecule appear with a bright center. Superposition of the molecular structures on the STM images is shown for a few cases. The red and blue arrows highlight the chain direction and molecular orientation, respectively.

As STM shows, along the chain directions cyano groups prefer to stay close to each other yet mostly not in a straight head-to-head fashion. The cyano groups commonly are tilted with respect to the chain direction, illustrated by the red and the blue arrows in Figure 4.8. This observation is consistent with the report by Pacchioni *et al*. [83], which has shown that on Cu(111) the cyano groups do not have to coordinate always exactly head on to a Cu adatom, but that the orientation of the molecules in the chain can be different because of the registry effects with the substrate. In our image, some molecules appear to have a disproportional aspect ratio due to thermal drift. Thus not all the molecular orientations could be determined. In the case of free-based pyrphyrin metalation on the Cu(111) surface, all three cyano groups coordinate one copper atom [14]. However, in the case of CuPyr, copper coordination could not be proven or excluded.

In order to explore the functionality of the metal adatoms with respect to self-assembly of pyrphyrin, small amounts of Ni (approximately one Ni atom per every three pyrphyrin molecules, as determined by XPS) were evaporated onto a sub-monolayer CoPyr/Cu(111) sample and subsequently annealed to 150 °C for 20 minutes. Interestingly, at room temperature, instead of being too mobile to be scanned, some molecules could be clearly resolved (Figure 4.9). They aggregate on the surface into clusters, indicating that these are immobilized pyrphyrin molecules, whereas the rest of the surface remains unresolved due to the high mobility at this temperature.

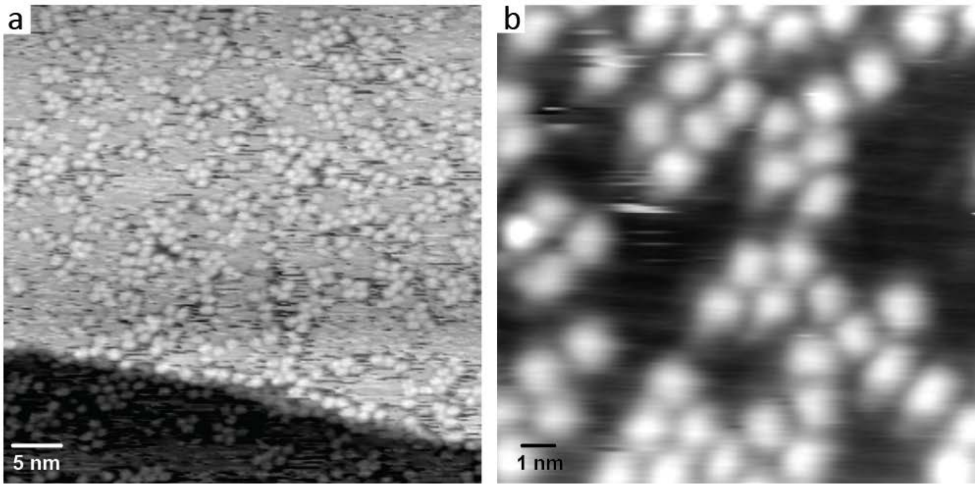

Figure 4.9: STM images of a sample in which Ni atoms were evaporated onto CoPyr molecules adsorbed on the Cu(111) surface, and subsequently annealed to 150 °C. The images were measured at room temperature. a) Molecule clusters were resolved without specific assembly. (50 nm × 50 nm, 1.7 V, 30 nA) b) At higher magnification clustering is revealed. (15 nm × 15 nm, -1.7 V, 40 mA).

Figure 4.10 shows STM images of similar experiments performed on a Au(111) surface, measured either at room temperature (a, b) or at 130 K (c). Some assembled patches are observed across the surface. A detailed image on the ordered structure reveals that, the molecules form a honeycomb structure. Some pores are empty, but many pores of the honeycomb lattice are occupied by a species appearing as a “doughnut”, *i.e.*, appearing as circles with a slightly bigger diameter than the network-molecules. A rotating molecule in the vacancy is responsible for such appearance [106]. Upon cooling, the doughnuts disappear and the honeycomb network becomes more ordered. At 130 K, the honeycomb structure could be nicely observed, suggesting that, just like in the case of CuPyr, the cyano groups interact with each other. The observed assembly is recognized as a so-called kagome tiling, whose basic elements are hexagons and triangles.

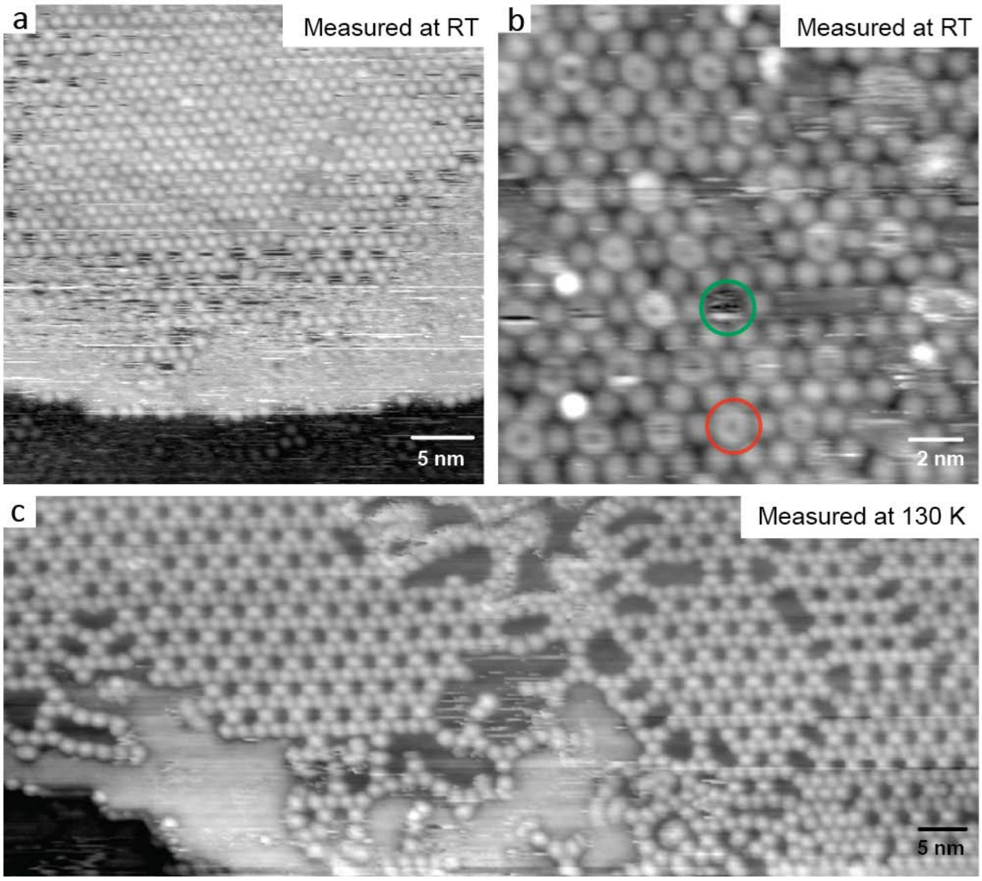

Figure 4.10: STM images taken after Ni atoms were evaporated onto CoPyr molecules on Au(111) surface, and subsequently annealed to 150 °C. The self-assembly pattern could be observed at room temperature (a, b) and at lower temperature 130 K (c). A hollow pore site and a filled pore with a rotating molecule were labeled with green and red circles in (b), respectively. Scanning parameters: a) 40 nm × 40 nm, 575 mV, 10 pA; b) 18.6 nm × 18.6 nm, 1.16 V, 10 pA; c) 105 nm × 41 nm, 1.25 V, 30 pA.

4.3 Pyrphyrin metalation with ruthenium

Studies have shown that ruthenium porphyrins have a high stability and better selectivity as a catalyst for various reactions [107–111]. Coordination of Ru atoms in the core of molecular pyrphyrin can result in a chemically stable catalyst.

In order to introduce ruthenium atoms onto surfaces in-situ, a ruthenium rod was used in an e-beam evaporator, which faced directly the gold substrate with a full monolayer of free-based pyrphyrin. Subsequent annealing up to 300 °C was conducted. The evaporation temperature for the 2HPyr was 330 °C. The results are shown in Figure 4.11.

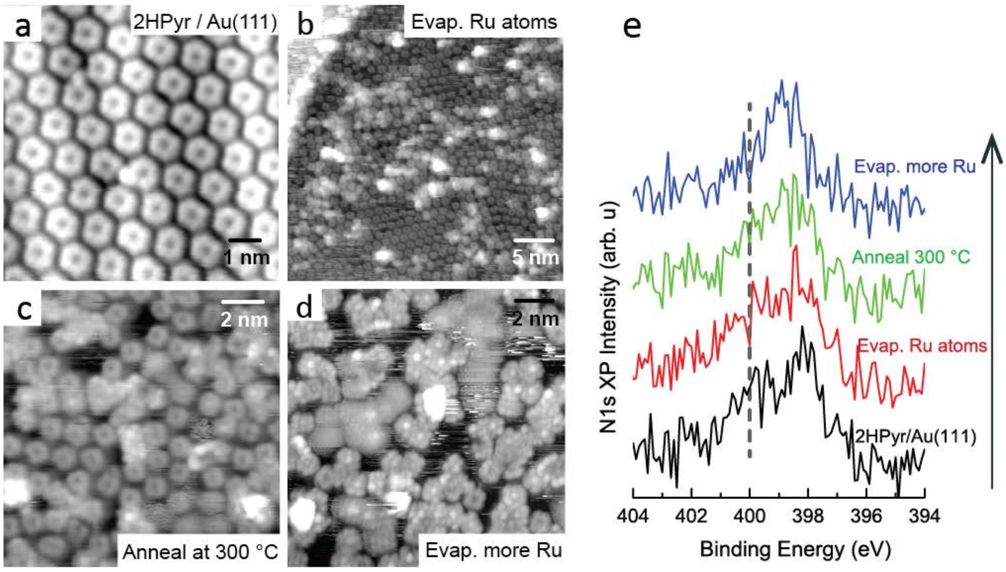

Figure 4.11: STM images of a series of experiments in the attempt to achieve ruthenium-metalated pyrphyrin. a) A monolayer of 2HPyr on Au (111) surface led to self-assembly of molecules, 9.3 nm × 9.3 nm, 758 mV, 300 pA; b) STM image after Ru atoms have been evaporated onto the sample shown in (a). Clusters of Ru can be seen as well as the molecules, which appear mostly hollow in the core, 37 nm × 37 nm, 385.7 mV, 20 pA; c) Annealing to 300 °C led to metalation of a limited number of molecules, suggested by the bright protrusion in the core of the molecules. 14 nm × 14 nm, 611.3 mV, 200 pA; d) Evaporating more Ru atoms onto the previous sample led to more molecules to appear with a bright core. 15 nm × 15 nm, -341.2 mV, -160 pA; e) XP spectra of the N1s region on the four samples. The disappearance of the shoulder at ~400 eV of the N1s peak (labeled by a dashed line) showed the metalation of pyrphyrin with Ru atoms. Spectra are shown after clean Au(111) surface background subtraction.

One monolayer of 2HPyr on Au(111) surface led to self-assembly of molecules, shown in Figure 4.11(a), as previously reported [80]. They adopt the hexagonal symmetry of the metal surface underneath. Each molecule appears to be hollow in the center. As shown in Figure 4.11(b), after ruthenium evaporation onto the molecules, the ruthenium atoms form clusters on top of molecules. The self-assembly of the molecule is locally disrupted. Where the ruthenium clusters are not found, the assembly is still preserved. The reason for the local disorder seems to be that, the molecules tend to bind to Ru atoms with their cyano groups or interact otherwise instead of metalation of the macrocycle. All molecules appear to be dark in the core, which suggests that they are not metalated by Ru. In order to metalate the molecules, the sample was annealed to 300 °C for 10 min. As shown in Figure 4.11(c), small amounts of molecules appear to have a fairly bright protrusion in their centers, while most still appear hollow, suggesting that only a small quantity of molecules get metalated. So the majority remains to be free-base pyrphyrin. The reason is probably the very high cohesive energy of Ru which results in strong clustering. Yet for metalation single atoms are needed. Moreover, a Ru atom is quite big in diameter, which makes it difficult to become coordinated into the pyrphyrin macrocycle for steric reasons. Figure 4.11(d) was obtained when more ruthenium atoms were evaporated onto the previous sample. It is clearly seen that the molecules become clustered and immobilized on surface. This indicates that the molecules are likely dehydrogenated in the periphery and probably fused together via covalent bonds. Judging by the bright protrusion of the molecular core, more molecules got metalated. This observation is verified by XPS, shown in Figure 4.11(e). The N1s peak becomes narrower as more Ru atoms are added onto the surface.

4.4 Conclusion

Proven by TDS, the self-metalation of one monolayer of free-base pyrphyrin on Cu(111) proceeds at 377 K in the time-scale of seconds. N1s XPS evidences that after annealing for 10 min at 423 K all molecules are metalated with copper adatoms from the substrate. The XP spectra also exhibit a distinct upshift of the binding energy of the cyano nitrogen, indicating the coordination of Cu adatoms at the cyano groups. The observation of a honeycomb lattice at slightly lower coverage is due to the coordination of Cu adatoms with three cyano groups of different molecules. In addition, dehydrogenation at the periphery of the molecules at elevated temperatures (~550 K) has been observed. For multilayers of pyrphyrin, intact metalated CuPyr can be desorbed by annealing of multilayer samples.

In conclusion, our results show that the processes of i) on-surface metalation, ii) formation of highly ordered organometallic 2D layers of molecules bridged by coordinated Cu adatoms and iii) dehydrogenation at the periphery at elevated temperatures proceeds in pyrphyrin on Cu(111) as expected on the basis of the published literature for porphyrins and phtahlocyanins.

The metalation of pyrphyrin with Ru atoms provided by metalation has also been demonstrated. The reaction does not proceed completely, *i.e*. Ru clusters are observed even though not all molecules are metalated. This is attributed to the high cohesive energy of Ru which leads to the formation of stable clusters. So far, metalation of tetrapyrroles with Ru has been achieved via exposure of Ru carbonyl [112]. As outlook, application of Ru carbonyl as the Ru source can prevent the cluster of Ru and thus probably leads to a better metalation of pyrphyrins.

The possibility of Ni atoms as “linkers” on Au and Cu surfaces for CoPyr molecules is also explored. While on Au(111) Ni atoms link the molecules via cyano groups to form honeycomb or chain structure, on Cu(111) surface this linkage pattern is not observed.

These results demonstrate that the concepts of metalation can be generalized and can be relied on towards the on-surface synthesis of specific organometallic layers and the development of model systems with potential catalytic functionality.

Chapter 5 An on-surface pathway from PAHs to graphene

Graphene is a single sheet of carbon atoms bonded by sp^2 hybridized orbitals into a hexagonal, planar crystal lattice. It has caught intense attention ever since it was first experimentally obtained 2004 by exfoliation of pyrolytic graphite [113]. Its remarkable physical properties, such as high electronic mobility, good heat conductivity, perfect two-dimensionality, optical transparency, and structural strength, are promising for future microelectronic applications.

For many applications, high-quality graphene layers with large area and few defects or domains are required. Several approaches have been deployed to develop graphene on transition metal surfaces, such as mechanical exfoliation [113], synthesis from gaseous hydrocarbon precursors on metal substrates [114–116], and annealing of silicon carbide single crystals [117]. Among these methods, chemical vapor deposition (CVD) is considered the most promising route towards wafer scale industrious production [118]. While graphene growth on Ni or Ru surfaces involves the segregation of carbon atoms from the bulk to the surface [21,119–121], graphene growth on *e.g.* Cu(111) does occurs entirely at the surface [119,122].

In most studies, the precursor used for graphene growth, *i.e.* the carbon source, on metal surfaces is a simple gaseous hydrocarbon such as methane [114,123] or ethane [124–126]. It has been realized that graphene can also be synthesized from larger PAHs such as coronene, pentacene and rubrene [21,22]. Remarkably, Wan *et al*. reported that when these molecules are used as precursor they strongly affect the quality of graphene sheets grown on polycrystalline Cu at 1000°C [22]. That is, they found that pentacene and rubrene precursors led to more defects in the graphene layer compared to coronene. The authors explained this effect with the relative stability of dehydrogenated carbon clusters which can contain 6-rings or 5-rings. Furthermore, a recent report [127], which showed that para- and meta-terphenylene led to graphene formation at ~400°C on Cu foils and yet ortho-terpyhenylene does not, also indicates that the structures of molecular precursors can play a decisive role in the properties of the produced graphene layers. These reported results suggested that, the initial precursor molecular structure could (in some cases) be partially preserved into graphene, rather than being completely fragmented.

In addition, many carbon allotropes with extended sp^3 hybridization have been synthesized in the past decades, such as fullerenes, carbon nanotubes, and nanoribbons [128]. They show unique physical properties and were of high scientific interest. There are also more carbon allotropes which have been predicted and not yet experimentally achieved. Among them similar to graphene are two types of single layers, *i.e.* pentagraphene and haeckelites. Pentagraphene is a layer of carbon atoms which only consists of pentagons, however, being situated in two different heights [129]. Haeckelites are a class of carbon layer which consists of an equal number of pentagons and heptagons, in addition to a certain number of hexagons [130]. Pentagraphene is predicted to be experimentally unattainable while for haeckelites it is predicted that they could be stabilized through significant charge transfer [131].

In this chapter, two different PAH molecules, *i.e.* pentaindenocorannulene and coronene, have been used as precursors to exploit the pathway of carbon allotrope formation on a Cu(111) surface. Typical defects in both cases are also presented. The intermediate states of PAH dehydrogenation on metal surfaces and initial nucleation of graphene flakes are shown here and the underlying dynamics is discussed. Particularly, attempts of attaching pentaindenocorannulene molecules to the edges of graphene flakes have been shown. Notably, in addition to graphene, another chemical species has been observed on different samples using either of the precursors.

5.1 Graphene from pentaindenocorannulene

Pentaindenocorannulene [132,133] (PICOR) is a PAH with the molecular formula $C_{50}H_{20}$. Its molecular structure is shown in Scheme 5.1. Like corannulene, PICOR is also a geodesic polyarene, with a structural curvature of 12.6°, which is larger than that of corannulene. More interestingly in our case, the molecule has six pentagonal rings, as well as a five-fold rotation axis. Whether these pentagonal carbon rings can introduce additional defects into the graphene sheet or alter the overall course of graphene formation mechanism, which is considered to be atom-by-atom or by carbon clusters [134,135], remain unanswered questions. It would shine some light to the fundamental study of chemical reactions on surfaces if any connection between the nature of the precursor and graphene structure can be drawn.

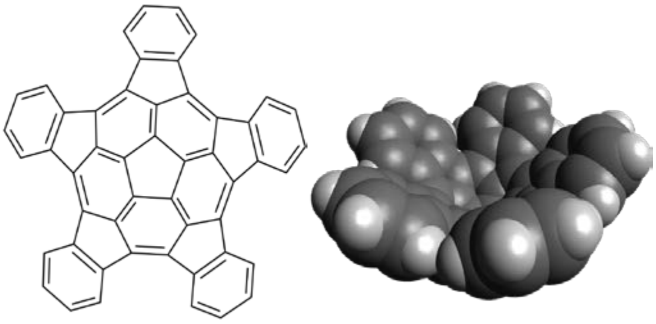

Scheme 5.1: Molecular models of pentaindenocorannulene

PICOR was thermally evaporated onto the single crystal Cu(111) surface which was kept at a certain temperature (T_C), followed by further annealing at the same temperature for 5 minutes. The crucible temperature and duration of the evaporation (typically 30 min) were chosen such that a significant amount of carbon (equivalent to ~0.6 – 1.5 graphene monolayers) could be observed by XPS. The sample was cooled down to room temperature for XPS and STM measurements. The cooling procedure was kept identical.

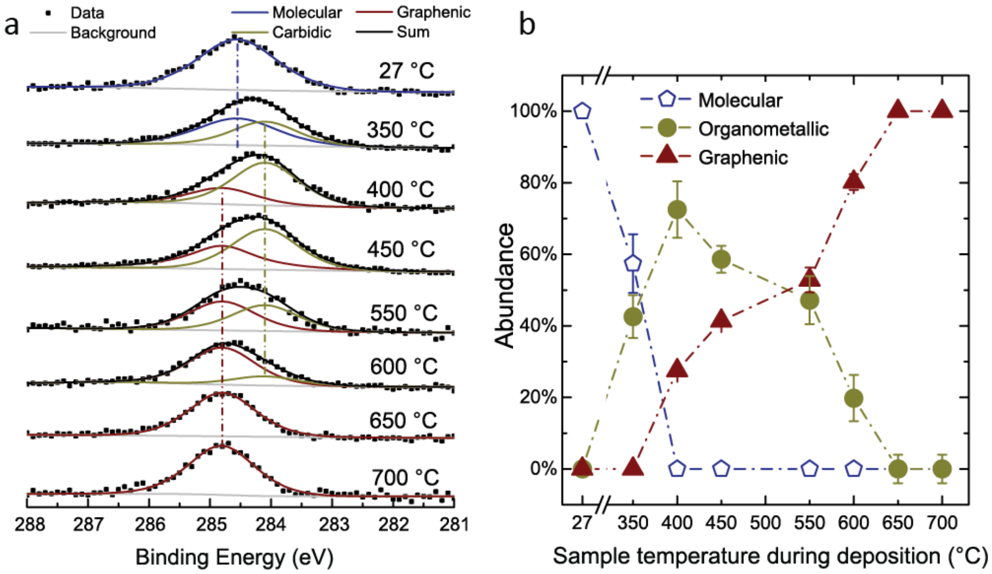

Figure 5.1: a) C1s XP spectra of the sample obtained at different temperatures (T_C) and measured at room temperature. Three distinctive peaks were fitted and assigned: molecular peak at 284.6 eV (blue), graphenic peak at 284.8 eV (red), and copper carbide peak at 284.1 eV (yellow), respectively. Graphenic peak and copper carbide peak have a full width at half maximum of 1.3 eV and molecular peak has one of 1.6 eV. The intensity of the signals was rescaled for comparison. b) Abundance of the three chemical species at different T_c.

Figure 5.1a presents C1s XP spectra obtained after the sublimation of PICOR on Cu(111) kept at different T_c ranging between 27°C (room temperature) to 700 °C. At 27 °C, the C1s signal presents a broad peak at 284.6 eV (fitted in blue, full with at half maximum (FWHM): 1.6 eV), consistent with the adsorbed PICOR molecules. At progressively higher temperatures, the C1s peak maxima shifted towards lower binding energies up to T_c = 450 °C. The observed downshift is consistent with the scission of C-H bonds on Cu surfaces [14]. The dehydrogenated molecules bind strongly to the surface and/or Cu ad-atoms, resulting in a lower C1s binding energy of this organometallic species [136,137]. For $T_c \geq$ 450 °C, the C1s peak maxima shifts to a higher value, reaching 284.8 eV for T_c = 700°C, consistent with graphene on Cu(111) [138]. As will be shown further below, the carbon has been transformed into graphene at this temperature. Consistent with these considerations, the C1s spectra are deconvoluted into three components, which are molecular (284.6 eV), organometallic (284.1 eV) and graphenic (284.8 eV) carbon. The abundance of these three components (the only free fit parameter) is shown in Figure 5.1b. The molecular signal completely disappears at T_c = 400°C, consistent with the complete dehydrogenation for other molecules reported to occur approximately at 230 to 550 °C [139]. The abundance of the graphenic species starts to rise at above 350 °C and become predominant for $T_c \geq$ 550 °C. For $T_c \geq$ 650 °C, the C1s spectra are entirely graphenic.

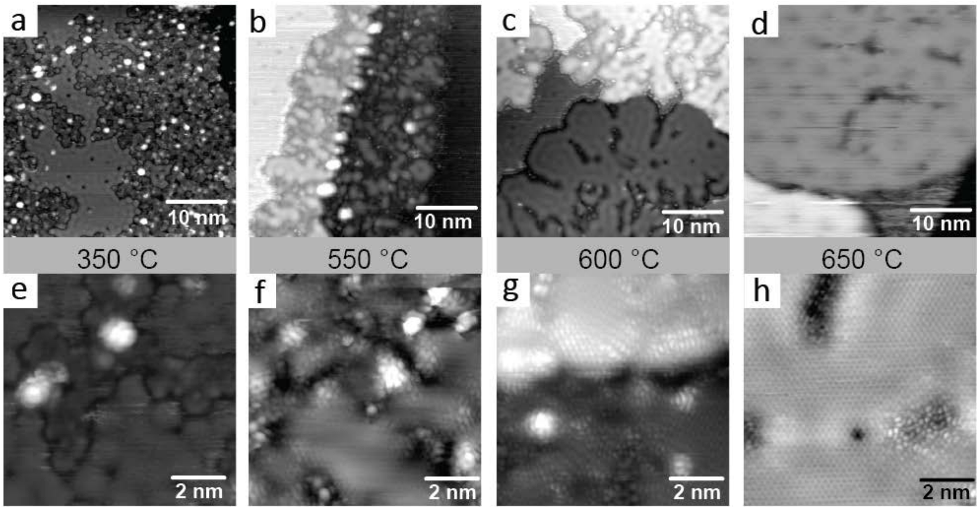

Figure 5.2: STM images of PICOR deposited onto a single Cu(111) surface kept at different temperatures. All images were measured at room temperature. a) 40 nm × 40 nm, 330 pA, 22.3 mV; b) 50 nm × 50 nm, 330 pA, 24.4 mV; c) 45 nm × 45 nm, 110 pA, 23.5 mV; d) 60 nm × 60 nm, 490 pA, 22.3 mV; e) 15 nm × 15 nm, 280 pA, 22.3 mV f) 7 nm × 7 nm, 310 pA, 20.1 mV; g) 12 nm × 12 nm, 270 pA, 28.4 mV; h) 20 nm × 20 nm, 250 pA, 23.5 mV.

Figure 5.2 compares the STM morphology of graphene after deposition at different T_c. All the images were acquired at room temperature. The images in the lower column show magnified areas for those directly above in the upper column.

In Figure 5.2 a), two areas on the surface can be noted, namely, mobile and immobile segments. In the immobile part, one can see interconnected structures merging from roundish lobes, developing into a fractal-like topology, and then fusing into larger pieces at a higher local coverage. These lobes have a diameter from 0.9 nm to 1.3 nm from half of its relative height (defined as the difference in height from its highest point to its local surrounding surface). Some of the exceedingly bright lobes' diameters vary from 0.8 nm to 1.6 nm (as shown in Figure 5.2 e)). These suggest that they are presumably pentagonal rings formed from the dehydrogenated PICOR molecules, which protrude from the surface due its structural curvature. The protrusions probably contain other non-hexagon rings as the counterpart for the convex, thus, maintaining a relatively flat structure in the long range. The fact that this type of molecular fragments with a curved-up geometry are so rarely observed here in the immobile section suggests that from an early annealing stage of 350 °C, the integrity of the pentagon core structure within the molecules has been largely lost or flattened. In addition, these exceedingly bright protrusions, presumably pentagonal rings, can also be formed by cyclodehydrogenation of adjacent hydrocarbons facilitated by the copper surface [140]. Interestingly, in the mobile part along the edge, one can see features with the diameter of 1.3 nm to 1.6 nm, *i.e*. close to the size of a precursor molecule. These are mostly likely to be mobile molecules which have a higher probability to appear at certain sites, especially at edges.

After the deposition at 550 °C, islands can be observed only at step edges while the other areas still contain mobile features. An enlarged image on the islands area shows that some graphene flakes started to form at this T_c, typically of the sizes of approximately 5 nm in diameter, yet there are many grain boundaries in this region, observed as the dark trenches in between the small graphene flakes. Next to these grain boundaries many irregular protrusions are observed. This finding can be explained such that, fragmented molecules, *i.e.* carbon clusters, have a larger mobility, but were immobilized at step edges, forming amorphous bands along the stepped region. The rest of the surface remains to have mobile “2D surface gas” which cannot be resolved by STM.

For the samples grown at 600 °C, graphene domains with bigger average size is observed. The grain boundaries in this case appear as dark trenches. Along the grain boundaries some brighter local defects can be seen. In the enlarged image g), one can see that graphene grows over the step edges. The phenomenon was also observed by Hollen *et al*. [141]. Many structural defects were observed.

When annealed at 650 °C, large domains of graphene are observed, and the resolved moiré pattern on one of the two domains shows that two different rotational domains exist, like previously reported [122]. On the large graphene flake, certain types of defects can be seen, such as long ridges and localized lattice defects, which will be discussed later. The rest of the surface, which is not covered with graphene, appears to be a mobile two-dimensional gas phase.

In summary, the warmer the reaction temperature is, the larger graphene domains grow. In addition there is always a 2D gas phase outside the graphene regions.

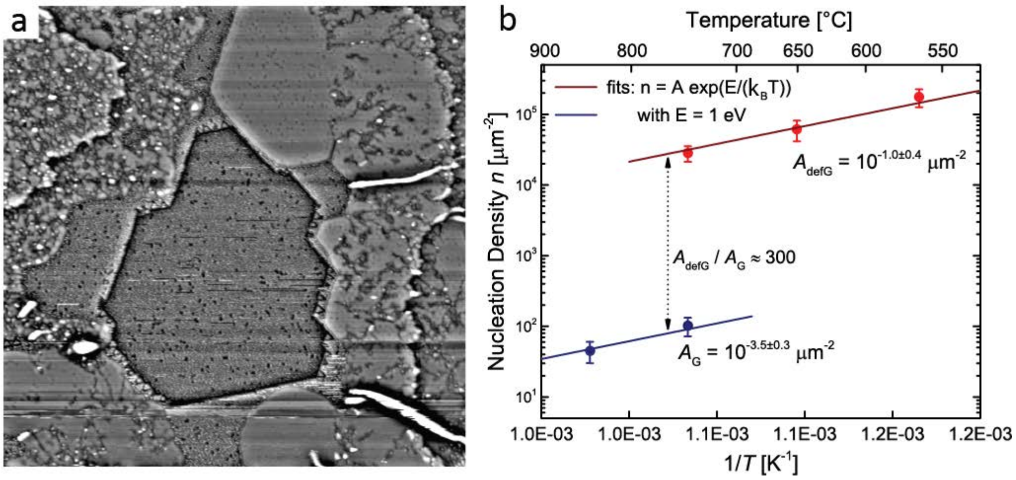

Figure 5.3: a) STM image acquired for T_c = 650 °C and a reaction time of 60 minutes. Image size is 140 nm × 140 nm. Scanning parameters are U = 26.6 mV and I = 410 pA. The image has been subtracted by its own Gaussian smoothed image for better inter-terrace contrast. b) Nucleation density as a function of sample temperature T_c during deposition. Data obtained with PICOR as precursor on single crystal Cu(111) substrate is shown. The activation energy was kept fixed to 1 eV, *i.e.* the value found by Kim *et al*., where growth of graphene was achieved by CVD on copper using methane as the precursor [142]. Only the prefactors are fitted to be A_G and A_{defG} for extended graphene (blue) and defective graphene (red), respectively.

Kim *et al.* [142] showed that one can determine the nucleation activation energy of graphene formation on Cu via CVD using methane as the precursor by plotting density of nuclei versus the reaction temperatures of the substrate during the nucleation process. They concluded that the activation energy was 1 eV for reaction temperatures below 850 °C, where the capture of carbon atoms by the graphene cluster played an crucial role and desorption of carbon clusters does not occur. Figure 5.3b shows here the plot of density of nuclei versus reaction temperature T_c on the Cu(111) surface from 700 °C down to 550 °C.. For 700°C and 650°C, the density of nuclei is determined by the number of extended graphene domains, separated by rotational domain boundaries, normalized by the entire image area. This extended graphene density is plotted in blue data points. For the formation temperature of 650 °C and lower, the density of nuclei is determined by the number of defective graphene flakes, which are fused and separated by distinctive grain boundaries, normalized by the total area of the defective graphene. These data points are plotted in red.

The nucleation densities of the extended graphene flakes obtained from PICOR on Cu(111) at high temperatures (700 °C and 650 °C) are highly consistent with the values obtained by Kim *et al.* [142], evidencing that the activation energy is the same in both cases, namely approximately 1 eV. At lower T_c, *i.e.* 550 °C, 600 °C and 650 °C, where defective graphene is observed, the density of the graphene flakes has also been evaluated. The overall nucleation density of defective graphene is much higher than for normal graphene, and the dependence of the nucleation densities with the inverse temperature is very similar. In both regimes the nucleation densities n can be fitted according to $n(T) = A \times \exp(\frac{E}{k_B T})$, where k_B is the Boltzmann constant and E is the activation energy (fixed to 1 eV). In this model the two regimes differ solely in the prefactors A which are $A_G = 10^{-3.5\pm0.3}$ µm^{-2} and $A_{defG} = 10^{-1.0\pm0.4}$ µm^{-2} for extended graphene and defective graphene, respectively. These two prefactors differ by a factor of about 300.

The similar activation energy suggests that, in this temperature regime, the underlying nucleation mechanism stays the same, regardless of the precursor species (being either single carbon molecules, such as methane, or PAH, such as pentaindenocorannulene). Considering that the molecules lands on a hot surface and dehydrogenate immediately, this similarity implies that, the molecular carbon-carbon bond breaking process occurs below 650 °C and the fragments consisting of pentagonal rings have already been broken into much smaller carbon clusters or even single atoms, which are then captured by the graphene flakes. As reported by Kim *et al.*, the prefactor at this temperature rigime indicates the geometric terms of capture and coalescence, as well as the partial pressure of the starting material, *i.e.* reactive carbon clusters in this case. The difference of the prefactors (indicated by the blue and red fits in the figure) is attributed to that, due to the incomplete C-C breaking process in the molecular precursor at lower temperatures, these incompletely broken molecules act as nucleation centers.

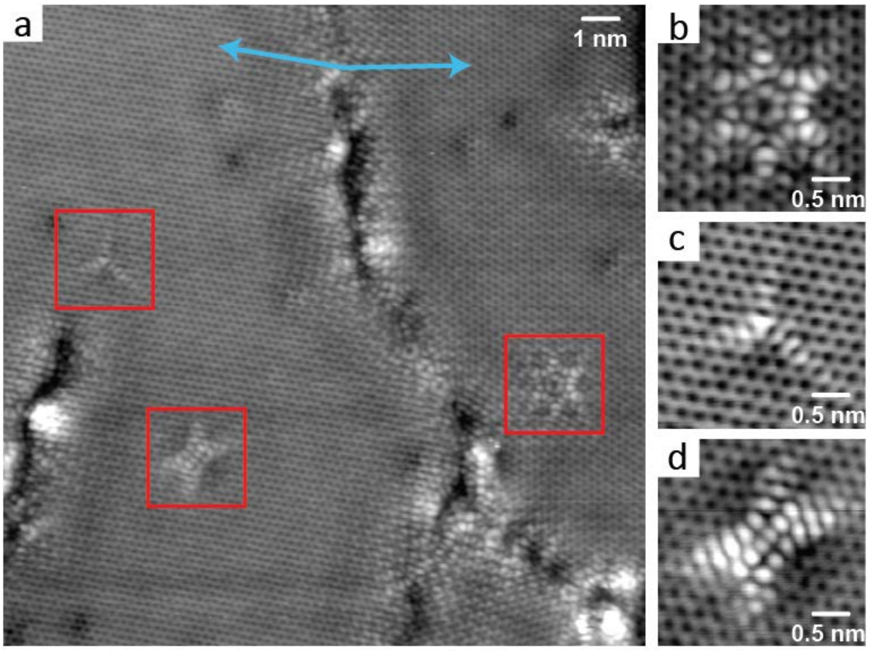

Figure 5.4: STM images of PICOR deposited onto a single Cu(111) surface kept at 650 °C during evaporation and subsequent annealed at 600 °C for one hour. Images were measured at room temperature. a) Blue arrows point to two graphene domains. The red squares show three typical defects also shown at higher magnification in b), c), and d).(STM conditions: a) 18.5 nm × 18.5 nm, 390pA, 22.9mV; b) 3nm × 3 nm, 1.15 nA, 24.4 mV; c) 3 nm × 3 nm, 49 pA, 22.8mV; d) 3 nm × 3 nm, 62 pA, 23.5 mV.)

Figure 5.4 shows some typical lattice defects on a corrugated region of graphene. In a) two different domains of graphene are clearly observed. They are rotated by approximately 13 degrees with respect to each other [118] and are separated by a grain boundary. The boundary has an irregular shape, which probably consists of lattice structural mismatch and local haeckelites structures [143]. Along the grain boundary modification of local electron states of the graphene sheets can be seen. This STM topology is caused by the electron scattering at the graphene domain boundary, producing a quantum interference effect [144].

In this region three different kinds of defects can be observed (marked in red squares). The defect shown in Figure 5.4b) is a grain boundary loop [145]. The lattice structure of this defect consists of six pairs of heptagonal and pentagonal rings, rotated by 60° with respect to each other, forming a loop circumventing one hexagon ring. It can also be considered as the smallest rotational domain. Here it appears slightly brighter in the left part than the right part, because of its proximity to the grain boundaries, which reduces the symmetry due to the redistribution of electrons. The defect shown in Figure 5.4c) is a three-fold rotational point defect. There are two reported point defects which present a similar three-fold symmetry. The first possibility is a vacancy created by a missing carbon atom in the lattice [146]. The second possibility is a pyridinic substitution of carbon by another atom, *e.g.* a nitrogen atoms [147]. In both cases the STM topology of the defects can vary depending on the tip condition and tunneling parameters [148]. The defect shown in Figure 5.4d) has D_{2h} symmetry. Note that the same defect may appear longer along the long 2-fold axis when different scanning voltages are used. This defect is most likely to be a Stone-Wales defect [149], which consists of two pairs of pentagonal and heptagonal rings. All these local defects can be formed during nucleation process as the internal crystal defect. They could be largely reduced in number if the temperature gradient while cooling down from reaction to room temperature was set to be substantially smaller. As shown in the next chapter, the origins of these defects do not depend on the nature of the molecular precursor.

In summary, thermal formation of graphene using pentaindenocorannulene molecules on copper (111) surface has been shown. Neither haeckelites nor pentagraphene in a controlled manner was obtained. The C-C breaking process does not alter the energy barrier of graphene nucleation, compared to the CVD method using a mono-carbon molecular source. Grain boundaries and limited local defects of graphene on Cu(111) have been experimentally observed.

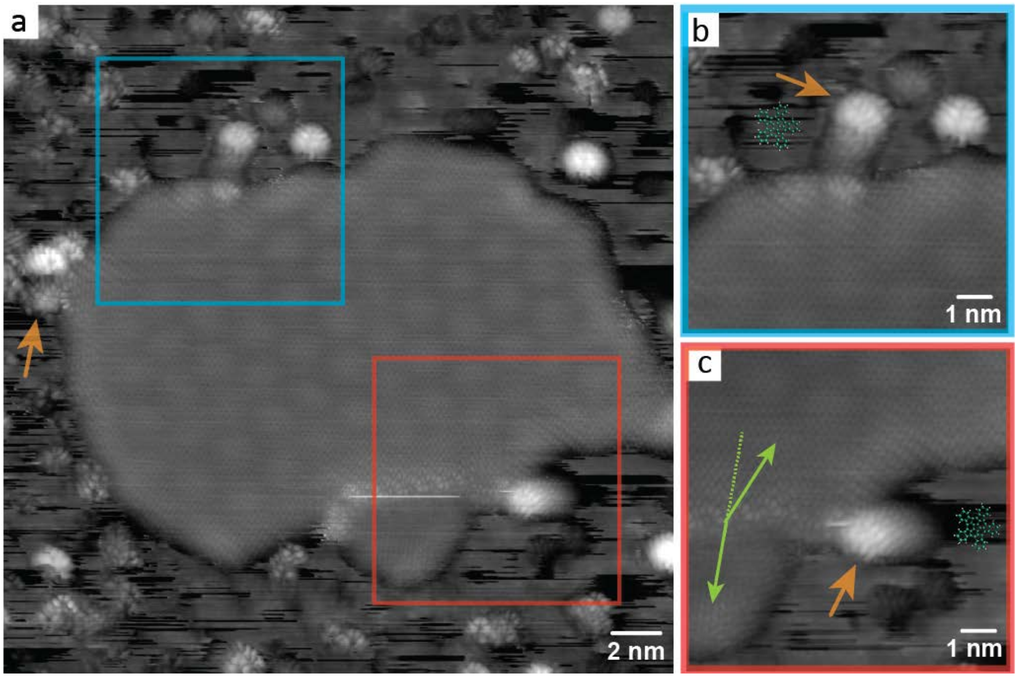

Figure 5.5: STM images on a sample which was first prepared at 650 °C and then cooled down to 350 °C for 60 minutes during evaporation of the precursor pentaindenocorannulene. A large graphene flake can be seen, as well as some probably fused fragments of molecules (orange arrows). Images b and c are enlarged areas labeled by blue and red on the edge of this graphene flake. Scaled schemes of pentaindenocorannulene molecules are also shown for comparison of its size. Green arrows in c indicate a grain boundary of two adjacent rotational domains of the graphene flake. A) 28 nm × 28 nm, 3.4 mV, 210 pA; b) 10 nm x 10 nm, 3.4 mV, 210 pA; c) 10 nm x 10 nm, 3.4 mV, 210 pA.

As discussed privously, PAH undergo dehydrogenation at about 350 °C, and turn into graphene gradually at temperatures above 450 °C. A technique to incorporate molecules into the edge of graphene flakes is to use different temperature regimes during evaporation. Inspired by He *et al.* [150], one way is to lower the reacting temperature from the graphene formation regime, *i.e.* 600 °C down to the dehydrogenation regime, where molecular backbone is not yet entirely destroyed, *i.e.* 350 °C. Figure 5.5 shows the sample produced via this approach. In an overview image a, a defect-free graphene domain can be clearly identified through its moiré Patten. It has an irregular shape with a dimension to be approximately 20 nm. A domain boundary could also be identified. Outside graphene of the area, the surface remained largely mobile with some spread chemical species, presumably dehydrogenated molecules. Along the boundary of graphene and mobile phases, there are some chemical species which appear to be round bright lobes (labeled by orange arrows), fully covalently bonded to graphene.

In order to confirm that the local defects do not origin from the pentagonal ring initially from PICOR molecular structure, similar experiments have been done also using coronene, which is a flat PAH without pentagonal ring in its molecular structure. These results are presented in the next section.

5.2 Graphene from coronene

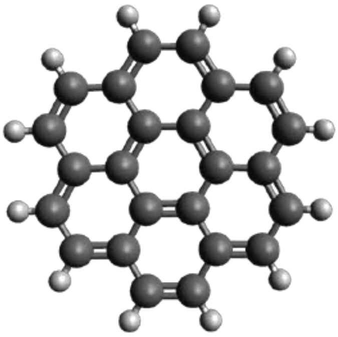

Scheme 5.2: Scheme of coronene molecule

Coronene is a PAH consisting of six perifused benzene rings. Its molecular structure is shown in Scheme 5.2. Since it is planar and aromatic, it can be seen as a subunit of graphene flakes. As a precursor, it appeared to improve the homogeneity of graphene acquired via CVD method. The reaction temperature of forming graphene was reported as low as 300 °C and the produced graphene had an enlarged grain size [151]. It was also found by DFT calculations that the complete dehydrogenated product of coronene has a delocalized π backbone and bind to the Ir(111) substrate with a dome-like shape [152]. This intermediate is energically favored and may be a crucial step of graphene growth before coalescence [153]. It has been shown that on Cu(111) the dehydrogenated species also acted as graphene seed, hence, it could facilitate island coalescence and suppress grain boundaries as a precursor [154]. Wan *et al*. [155] suggested that, on a copper foil, the graphene grown using coronene as precursor via CVD has a lower reaction temperature and a better quality in regards of its carrier mobility, compared to that using pentacene and rubrene as precursors.

Here the coronene molecule was thermally deposited from a Knusden cell onto a Cu(111) surface kept at T_c during the evaporation of 30 minutes and subsequently annealed for 5 min at the same temperature. The sample was cooled down to room temperature for STM imaging. Different T_c has been used and results are shown below and are compared to

PICOR results.

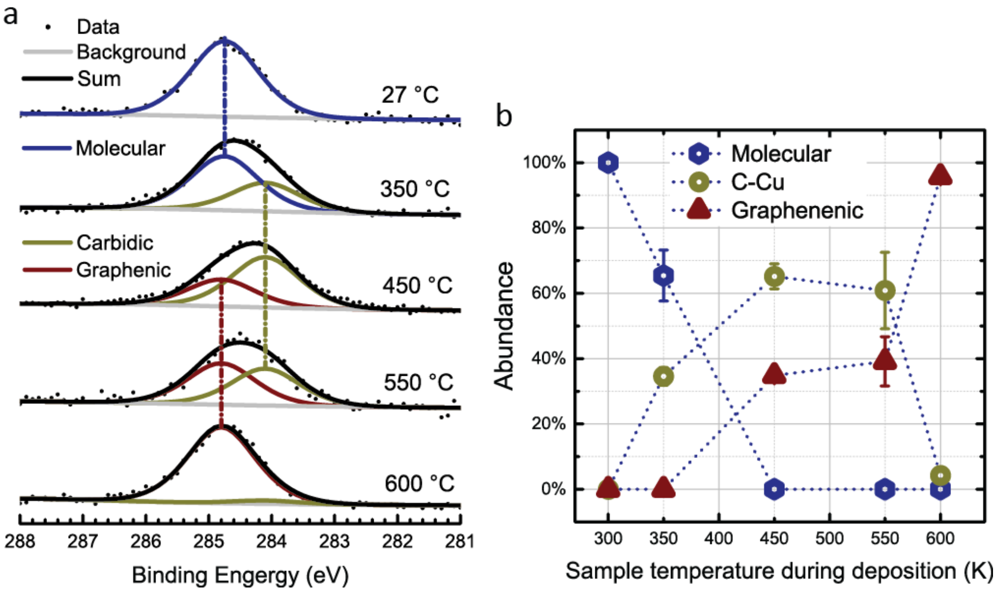

Figure 5.6: a) C1s XP spectra of the sample using coronene as precursor obtained at different T_C and measured at room temperature. Like in the case of PICOR, three distinctive peaks are fitted using the same parameters: molecular peak at 284.6 eV (blue), graphenic peak at 284.8 eV (red), and copper carbide peak at 284.1 eV (yellow). The intensity of the signal has been rescaled for clarity. B) Abundance of the three chemical species at different T_c.

XP C1s spectra at different T_c are shown in Figure 5.6a. The C1s binding energy of molecular coronene is 284.8 eV. If deposited on the substrate kept at 350 °C, the binding energy experienced a down shift to 284.5 eV. When the substrate was kept at 600 °C, the peak shifted up to 284.7 eV and became narrower. Here the peaks are fitted using the same fitting parameters (FMVH, peak position and shape, *etc.*) as used for pentaindenocorannulene. Only the binding energy of the molecular peak is slightly different. The analysis yields similar results as for PICOR. The carbidic peak starts to appear at 350 °C and increases in its intensity untill 450 °C, when the intensity starts to decrease, as the graphene component takes over. The carbidic component finally vanished at 600 °C. This overall trend, in which the C1s peak undergoes a downshift and then an upshift with increasing temperatures, has also been seen in the case of pentaindenocorannulene. As shown below by STM, at 350 °C the coronene molecules are dehydrogenated and at 600 °C large graphene flakes are produced.

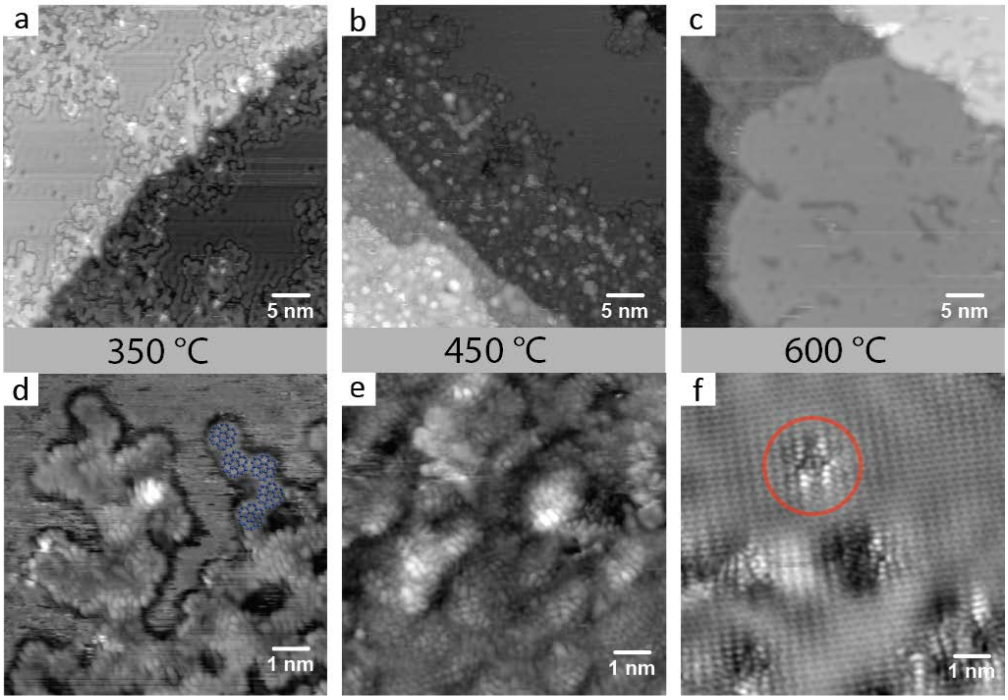

Figure 5.7: STM images acquired after coronene deposition onto Cu(111) surface kept at different T_C. Scaled schemes of dehydrogenated coronene superimposed on the fractal branch of image d for comparison. The red circle indicates a grain boundary loop defect. STM parameters: a, b, c are 46.6 nm × 46.6 nm and d, e, f are 10 nm × 10 nm. A) 29.3 mV, 210 pA; b) 23.5 mV, 410 pA; c) 29.3 mV, 530 pA; d) 35.3 mV, 290 pA; e) 36.3 mV, 250 pA; f) 25.9 mV, 490 pA.

In the case of T_C = 350 °C (Figure 5.7a), a fractal graphene topology, with the growth apparently originating at step edges, is observed in STM. The rest of the surface contains mobile species. Notably, there are many bright lobes emerging from the fractal region. While molecular coronene only consists of hexagons and is planar, Wan *et al*. [155] showed that when dehydrogenated, the periphery of coronene bends down to copper surface and form carbon-copper bonds, thus presenting a dome-like shape. The irregular protrusion observed here can also be attributed to be pentagonal rings which are formed via cyclodehydrogenation. This feature was also observed in the case of pentaindenocorannulene. A magnification of the fractal region (Figure 5.7d) shows that the average motif size on the edges is approximately 0.8 to 1 nm. Considering that coronene has the diameter of 0.7 nm when dehydrogenated, overlapping the dehydrogenated flat coronene fragments on the STM image suggests that the motifs that grow into fractals are indeed coronene based nano-graphene flakes, even though the detailed orientation cannot be determined.

Further integration of molecular fragments into graphene is explored via STM for the case of T_C = 350 °C (Figure 5.7 b and e). The fractal shapes disappear and a corrugated topology along step edges can be seen. At T_C = 600 °C (Figure 5.7 c and f), extended graphene flakes as well as defective graphene can be observed. Also grain loop boundary can be observed on one of the graphene flakes, as indicated by the red circle in Figure 5.7f. Remarkably, these results resemble the case of pentaindenocorannulene.

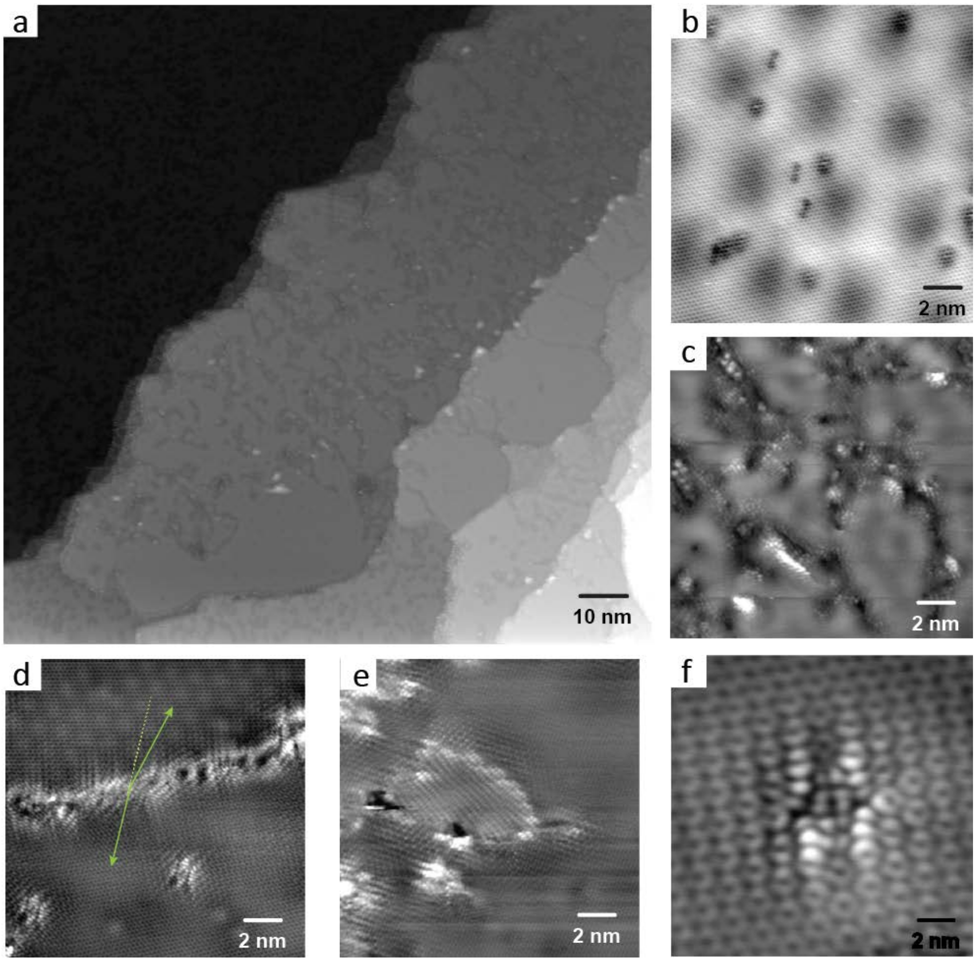

Figure 5.8: STM images after coronene deposition on a 600 °C Cu(111) surface measured at room temperature. a) Overview of different terraces. 140 nm × 140 nm, 27.5 mV, 240 pA; b) Graphene with its moiré STM appearance. 17 nm × 17 nm, 24.4 mV, 500 pA; c) STM image (17 nm × 17 nm, 22.9 mV, 520 pA) of defective graphene.; d) STM image (17 nm × 17 nm, 22.3 mV, 320 pA) showing two different rotational domains (green arrows), separated by a grain boundary.; e) A rotational domain circumcised by grain boundaries. 17 nm × 17 nm, 23.5 mV, 210 pA; f) A local defect found on defective graphene region. 4 nm × 4 nm. 22.3 mV, 480 pA.

At T_c = 600 °C, graphene flakes with diameters of approximately 20 nm to 50 nm can be observed (Figure 5.8a). On different terraces, different island sizes are observed. There are three types of regions: extended graphene, defective graphene, and a region containing mobile species, similar as in the case of PICOR. Interestingly, the step edges act in most cases as the boundaries between these three different regions. Figure 5.8b shows a magnified region of extended graphene. The moiré pattern with honeycomb structure is clearly observed. There are also some darker areas, which do not distort the structure of the graphene. Figure 5.8c shows the defective graphene region. The average nuclei size is approximately 5 nm. The grain boundaries can be considered to be fused by different nuclei. In Figure 5.8d, two different domains are shown, labeled by green arrows. They are rotated by about 12° with respect to each other. Two different moiré patterns can also be observed due to the rotational angles of the graphene lattice alignment with respect to the Cu(111) substrate. The periodicity of the moiré pattern is about 2 nm (upper domain) and 6 nm (lower domain), which are consistent with the findings previously presented by

Gao *et al*. [122]. Figure 5.8e shows a smaller domain with irregular shape surrounded by a larger domain. Figure 5.8f shows a grain boundary loop [145], similar to the one found in the case of pentaindenocorannulene.

In summary, using coronene as precursor leads to a similar topology like for PICOR. At the dehydrogenation temperature of 350 °C, the similarity of bright protrusion structures suggests that PICOR molecules lose their less stable pentagonal rings at very early stage of the surface-assisted reaction, probably together or even before dehydrogenation. The similar fractal topology and dimension suggests that for both precursors the fragments undergo a diffusion-limited aggregation.

5.3 Self-assembly of excess carbon: a new unknown species

In the process of making graphene with these highly rotationally symmetric graphenic molecules, an interesting phenomenon has been reported: there appeared ball-shaped unknown species along edges of the mobile regions on many different samples.

Each "ball" has the diameter of approximately 0.5 nm. They only appeared on the mobile regions at the step edges, either adjacent to another terrace containing only mobile species or close to the rim of a graphene flake. When T_c is 600 °C, the balls conglomerate in adjacent to graphene flakes, not following any specific directions (c), while T_c = 650 °C, they form chains along the step edges with certain directions with 120 degrees difference with respect to each other (b). Notably, in Figure 5.9b, these directions are the lattice directions of the Cu(111) surface.

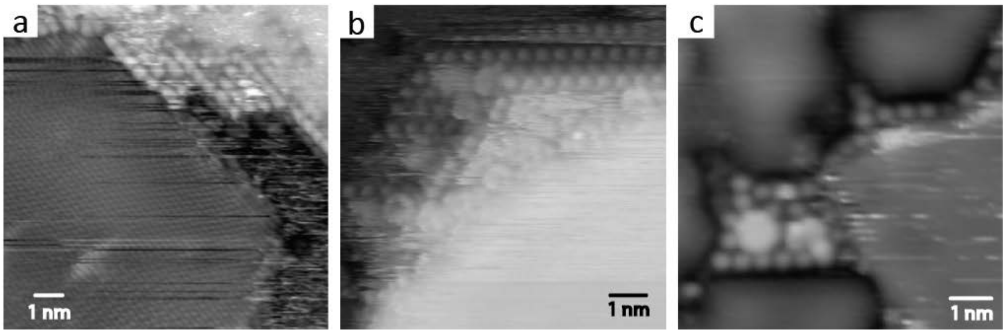

Figure 5.9: Detailed STM images on the unknown species found in the mobile areas on different samples using pentaindenocorannulene as the precursor. A) T_c =650 °C followed by 60 minutes annealing at 600 °C, 12 nm × 12 nm, 21.7 mV, 380 pA. b) T_c = 650 °C, 9 nm × 9 nm, 23.5 mV, 340 pA. c) T_c = 600 °C, 8 nm × 8 nm, 23.5 mV, 110 pA.

In particular, one sample was acquired with both pentaindenocorannulene and coronene as precursors at 550 °C and subsequent annealing to 650 °C, resulting in a considerably more carbon quantity, *i.e*. equivalent of 1.5 monolayer of densely-packed PICOR on Cu(111). On this sample, the surface was fully covered with the three types of characteristic regions like in the previous cases: defective graphene, large graphene flakes and mobile areas. Defective graphene areas are much prominent than extended graphene flakes. In addition, the sizes of graphene flakes are averagely much smaller than the standard samples with a lower carbon quantity. Notably an assembly pattern of the unknown species is formed, shown in Figure 5.10. Two rotational domains have been found, with a 79° difference with respect to each other (Figure 5.10 a and b). Both domains consist of chains, which, in the case of a, was rotated 18° (labeled by blue arrow) from the underlying Cu(111) lattice direction. In the case of b, the rotational angle is 97° (labeled by yellow arrow). Both domains have certain vacancies. Two characteristic directions can be determined from this assembly pattern (Figure5.10c): the line direction along the chains (blue, d), which is closely packed with the periodic distance to be 0.5 nm, and the column direction of adjacent chains (green, e), with the periodic distance to be 0.9 nm.

On image a), around the edges of this self-assembled region, peculiar triangles can be observed. A close look (f) shows that they are formed by a bright equilateral triangular terrace circumcised by arrays of unknown particles which has the diameter of 0.5 nm. The triangles follow the Cu(111) lattice directions (labeled by red arrows).

The exact chemical formation of these “balls” cannot be determined by STM. Here two possible situations are proposed and discussed. Since carbon fragments are the main ingredients, it is suitable to assume that the balls could be fullerenes.

One of the most common fullerenes, C_{60}, can be decomposed into three patches of dehydrogenated corannulene molecules, which is exactly a fragment of pentaindenocorannulene. Notably, the diameter of C_{60} fullerenes is 0.7 nm, and self-assemble on the Cu(111) surface into a (4 × 4) over layer following the $<1\bar{1}0>$ direction with the nearest neighbor distance to be 1 nm [156]. Notably, Bauert has reported a very similar assembly pattern on a sample which used pentamethyl-corannulene molecule as the precursor and the copper (111) substrate was held at approximately 660 K during deposition [64]. Yet in the case of the unknown balls here using PICOR, the nearest neighbor distance is 0.5 nm, suggesting that they are not C_{60} fullerene.

Another possible assumption is the smallest fullerene, C_{20} cage. It consists of only pentagons and has a large curvature. Since its structure violates Kroto’s “isolated pentagon rule”, the C_{20} fullerene is extremely unstable [157]. C_{20} ions have been experimentally synthesized by replacing H atoms with weakly bonded Br in its perhydrogenated form, dodecahedron $C_{20}H_{20}$, and subsequently debrominating in gas-phase [158]. Though it is not stable in its isolated form, they may process a large charge transfer when adsorbed on metal surfaces, and thus stabilize exist as charged ions.

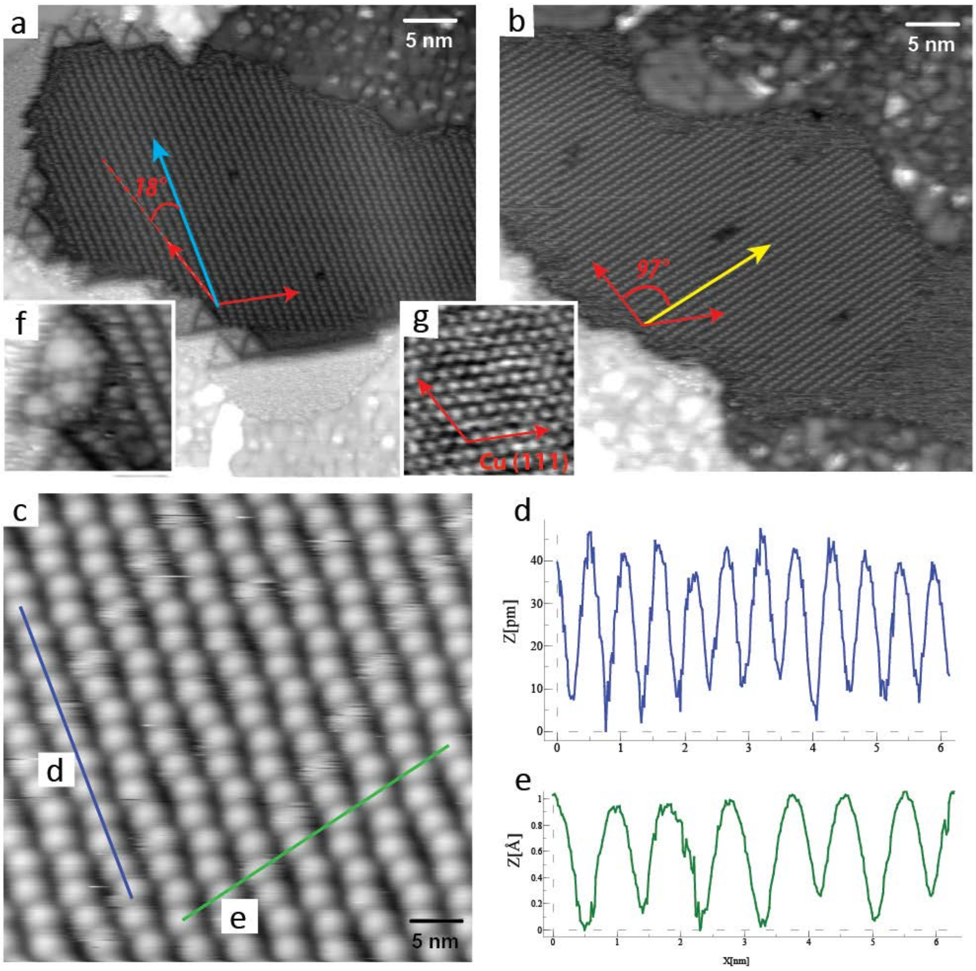

Figure 5.10: Self-assembly patterns of unknown species in a sample, which has both coronene and pentaindenocorannulene evaporated for 30 minutes on a 550 °C Cu(111) surface and then has been annealed at 650 °C for 30 minutes. a (46.6 nm × 46.6 nm, 24.4 mV, 180 pA) and b (46.6 nm × 46.6 nm, 28.4 mV, 340 pA) show two different rotational domains. Red arrows are the lattice directions of Cu(111) surface. The self-assembled regions are rotated 18° and 97°, respectively. c (9.3 nm × 9.3 nm, 1.5V, 370 pA) shows the enlarged assembly pattern and two height profiles along the two distinct directions (d and f); g shows the Cu(111) surface.

5.4 Conclusion

Pathways of thermally grown graphene in UHV on Cu(111) using two PAH precursors have been studied. The fact that using either flat or curved molecular precursor leads to similar growth pattern suggests that the PAH's original structure has broken at a low temperature before graphene flake formation starts. Thus, it is not possible to introduce defects with pentagonal rings in a controlled manner into the later produced graphene with this method. Nevertheless, attachment of dehydrogenated molecules to the peripheries of graphene flakes has been realized at a lower temperature.

Chapter 6 Ullmann Coupling of bromo-helicenes on metal surfaces

Chirality of molecules are of great interest in various topics in the field of surface science, such as enantioselective heterogeneous catalysis [159], biomineralization [160], and crystallization of chiral molecules [161]. As a class of chirality, molecular helicity, plays an important role in molecular biology [162]. The on-surface crystallization of such chiral molecules has raised a lot of scientific attention in the past decades [163–166]. Among these molecules are helicenes, a group of PAH with [a,c]-annulated benzene rings such that helical chirality arises. They have caught special interest, with potential applications in organic thin film electronics or as light sensors and spin filters [167,168]. In order to achieve the molecular functionality for applications, the formation of stable films is required, maybe by covalent bonding into extended networks.

Ullmann coupling [23] generates carbon-carbon bonds of adsorbed molecules on solid copper and has become a popular reaction for creation of larger covalently-bonded motifs at surfaces [24–26,28–31,169–182]. The Ullmann coupling takes place in two steps. Firstly, a carbon–halogen bond in the molecule undergoes a scission assisted by the surface metal atoms, typically copper, gold or silver, so a carbon–metal binding motif is formed. Secondly, when annealed at higher temperatures, the metal atoms are set free and new carbon–carbon bonds between two reactants are formed.

In this chapter, the dimerization and trimerization of bromo[4]helicenes via Ullmann coupling on copper and gold surfaces and the subsequent 2D assembly of products are demonstrated by means of STM and XPS.

6.1 2-Bromo[4]helicene on Cu (100)

Tetrahelicene consists of four benzene rings forming a helix due steric overcrowding of two hydrogen atoms (blue dashed ellipses in Scheme 6.1). As the inversion barrier is about 4 kcal/Mol (calculated from [183]), the sense of helicity is inverted rapidly at room temperature. In order to introduce Ullmann coupling, approximately 1.5 ML of 2-bromohelicene **1** was deposited onto Cu(100) and subsequent annealed to 463 K. Under these conditions, molecules in the second layer became desorbed. For STM imaging at room temperature, a densely packed monolayer of the product bishelicene **2** was required, so that sufficient molecular immobility was induced. Samples with a lower coverage or before reaction could not be imaged at temperatures above 130 K.

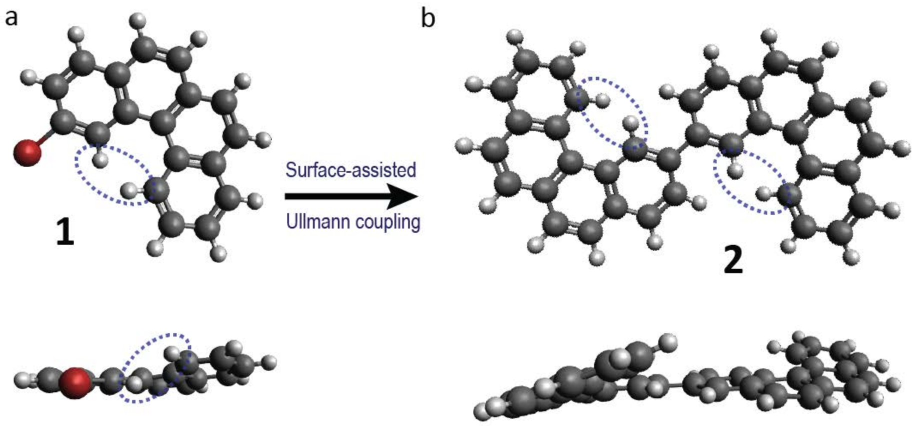

Scheme 6.1: Ullmann coupling between two 2-bromo[4]helicenes (**1**) leading to 2,2'-bis[4]helicene (**2**). The main products formed on the Cu(100) surface are anti-(P,P)-**2** and anti-(M,M)-**2**. Blue dashed ellipses label the two hydrogen atoms, which repel each other.

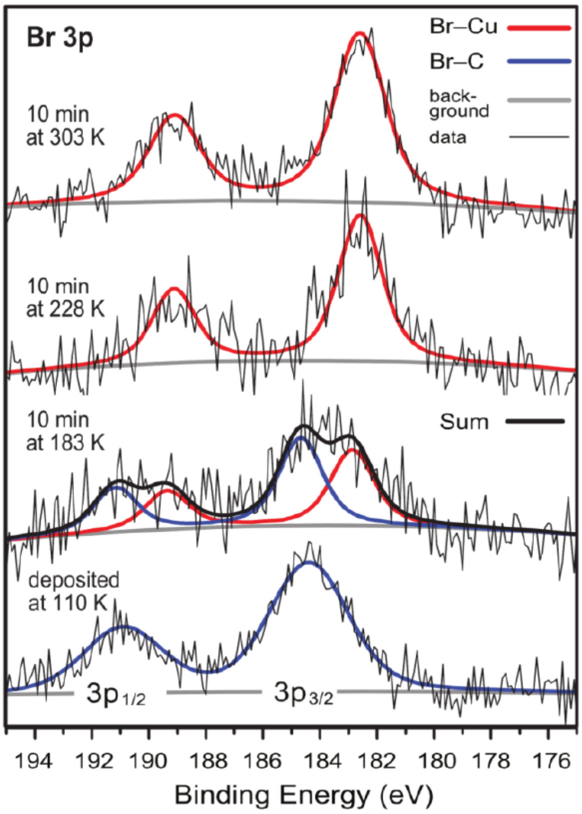

Figure 6.1: Series of XP spectra of the Br3p region after deposition of **1** on Cu(100) which was kept at 110 K, and subsequently annealed to higher temperatures as shown in the figure. The background, which is obtained from the clean Cu(100) surface, has been subtracted. The Br3p electron binding energies are characteristic of the chemical states of the bromine atom. When bromine atom is attached to the carbon atom in the intact helicene, it has its $3p_{3/2}$ peak maximum at 184.4 eV binding energy (blue curves), but shifts by 1.6 eV to a lower energy in the dissociated state and bound to the surface copper atoms (red curves).

The Br3p XP spectra (Figure 6.1) clearly revealed the peak shift before and after the first step of the reaction, namely dissociation of the bromine atoms off the carbon frame. Upon the deposition at 110 K, the binding energy of the Br3p$_{3/2}$ peak is 184.4 eV, consistent with intact C–Br bonds [173,174]. A peak shift to a lower binding energy has been observed after annealing, indicating the disassociation of the Br atom from the molecule. The spectra here show that this C–Br bond scission happens in part already at 183 K and is accomplished completely at 228 K. This finding is confirmed by a previous report on 4,4''-dibromoterphenylene on Cu(111) (170 K < T < 240 K) [173].

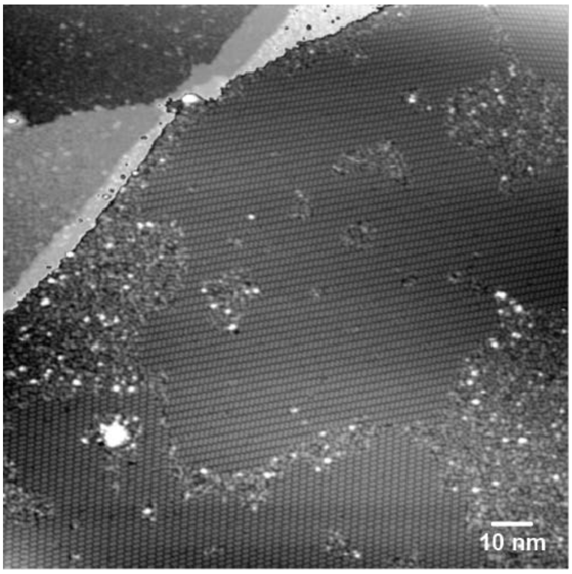

Figure 6.2: Large scale STM image acquired after deposition of **1** on Cu(100) and annealing to 463 K (150 nm × 150 nm, 1.2 V, 30 pA, measured at 295 K). The image's grey scale was folded for better contrast over the step edge. About 60% of the surface is covered with self-assembled domains of (*P, P*)-**2** and (M,M)-**2**.

Figure 6.2 and 6.3 show STM images recorded after annealing at 463 K, where C-C bond formation is expected to occur. The product molecules are bishelicenes, appearing as ''*S*'' and ''*Z*'' shaped on the surface (Figure 6.3). At full monolayer coverage, the product self-assembled into four ordered domains, which covered approximately 60% of the entire surface. For either "S" or "Z", there are four rotational domains accordingly. In addition, there are areas that show no long-range order.

In an image obtained with different scanning parameters and a different tip condition (Figure 6.3b), the benzo groups at opposite ends of each bishelicenes were clearly visible as bright protrusions. In constant current scanning mode, those molecular parts further away from the surface are coded by the computer with larger brightness. Therefore, both ends of the bishelicenes spiral away from the surface in a clockwise fashion. This also means the central part of the product is located closer to the surface. These are left-handed spirals (blue arrows in Figure 6.3b), to be labeled as (*M*)-enantiomer according to the Cahn-Ingold-Prelog rules. The (*M,M*)-**2** product unoccupied orbitals have been simulated with extended Hückel Theory and optimized on Cu (100) (Figure 6.3c). This observation explicitly leads to the conclusion that the ''*S*'' bishelicene is a (*M,M*)-enantiomer. Hence, the "Z" shaped ones are (*P,P*)-**2**.

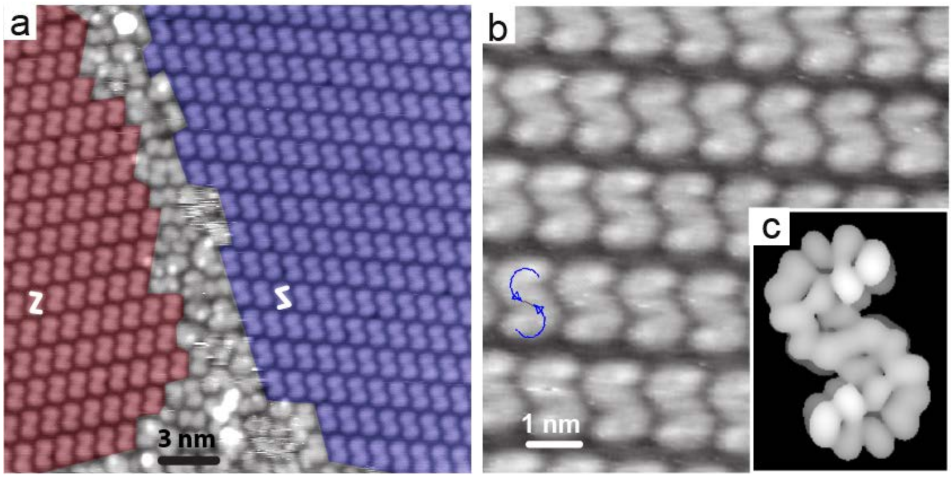

Figure 6.3: STM images recorded after deposition of **1** on Cu(100) and annealing to 463 K. (a) A large-scale image (1.2 V, 30 pA, RT) shows self-assembly of (*P,P*)-**2** (labeled red) and (*M,M*)-**2** (labeled blue). (b) STM image (1.8 V, 30 pA, RT) of a domain of (*M,M*)-**2** with intramolecular resolution. The blue circular arrows indicate the counterclockwise left-handedness of the helices. (c) Electron density of the lowest 3 unoccupied states of the bishelicene simulated with extended Hückel theory.

If stereoselectivity during the Ullmann reaction is not taken consideration, a 2 : 1 : 1 ratio would be expected for all three possible products (*P,M*)-**2** : (*P,P*)-**2** : (*M,M*)-**2**, respectively. However, no (*P,M*)-**2** isomers can be found on the surface. Therefore, the dynamics of this reaction can be explained as follows.

In the intermediate states where the helical molecular motif is bonded to copper surface ad-atoms, the helix bends up away from the surface. Upon further annealing, the ad-atom is released, and bishelicenes are formed with the central part, *i.e.* the reacting site, closer to the surface. Due to the low inversion barrier of 4 kcal/mol, however, the handedness of both helices should switch constantly at such high reaction temperature. The diasterioselective outcome, *i.e.* homochiral products instead any *syn-(P,M)* or *anti-(P,M)* isomers must be therefore assigned to the post-reaction phase of cooling and self-assembly, when the helices flip into the most favored conformation dictated by the better stereo-alignment on the surface.

Note that approximately 40% of the surface was covered with a disordered layer of molecules, which presented many configurations in the STM images. Most of them resemble the bishelicenes in shape and size in the ordered domains. Nevertheless, a few of them differ in their sizes and appearances. Two typical species have been highlighted in Figure 6.4. While the characteristic length of **2** is 14.6 ± 0.4 Å, these two species have the length of 17.0 ± 0.3 Å (Figure 6.4b) and 16.2 ± 0.4 Å (Figure 6.4c), respectively.

In order to identify these two chemical species, *anti*- and *syn*-bishelicenes both as organic product (*i.e.* the product **2**) and the intermediate species with Cu ad-atom (C–Cu–C) [33] have been simulated. The simulated characterizing length of *anti*-bishelicenes agrees well with the elongated bishelicenes model with the presence of copper atom in the long *anti*-species. Hence, the conclusion can be drawn that the observed two distinctive chemical species in Figure 6.4 are actually organometallic intermediates.

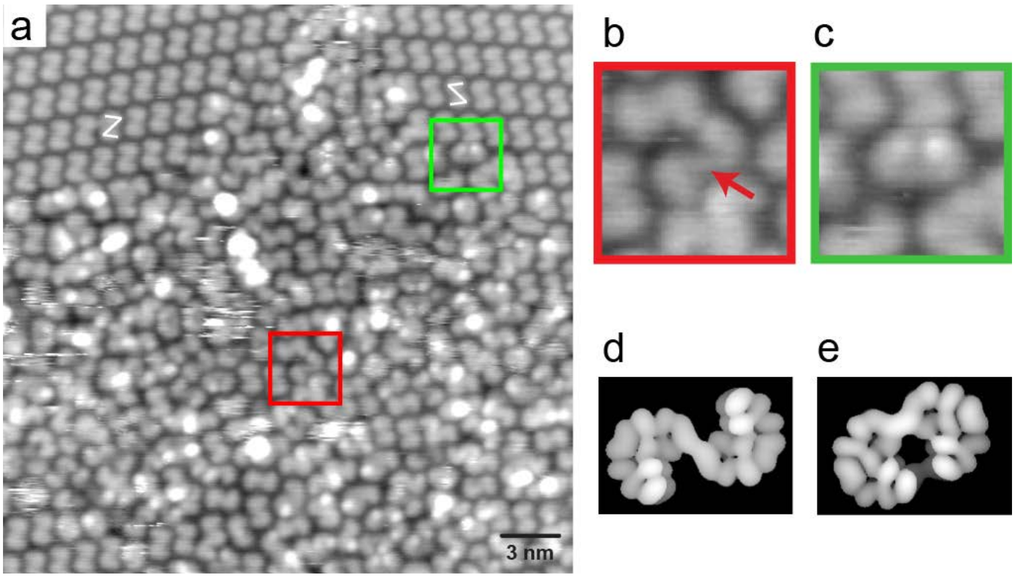

Figure 6.4: (a) STM image (30 nm × 30 nm, 1.2 V, 30 pA, RT) of a disordered area next to the self-assembled domains. An elongated *anti*-species (b) and a *syn*-species (c) have been repeatedly detected in the disordered area. (b) and (c) are magnifications from image (a) showing these two species. (d) and (e) are the molecular mechanics simulations [175,182] of their C–Cu–C intermediates respectively. Here the density of the lowest three unoccupied molecular orbitals have been simulated using the extended Hückel theory for the *anti-(P,P)* (d) and *syn-(M,P)* (e) intermediates species with one copper atom located between the two helicene ligands.

Similar experiments have also been performed on oxygen-reconstructed Cu(100), as this surface was reported to facilitate Ullmann coupling with a higher reaction temperature [184]. As shown in Figure 6.5a, the temperature for C–Br bond dissociation on O/Cu(111) is 338 K, higher than that on Cu(110). This observation agrees with conclusions made in the literature, *i.e.* C–Br bond scission of aryl bromides on oxidized copper surfaces at RT [182,185].

Upon annealing to 463 K, there is no long-range ordered self-assembled domain observed, whereas bishelicenes in *anti*- and *syn*- configurations are found in an non-ordered fashion, as shown in the STM image in Figure 6.5b. It can be concluded from the lengths of these molecules on O/Cu (100) (16.5 ±0.6 Å and 15.5 ±0.5 Å, respectively) that they are again organometallic intermediates.

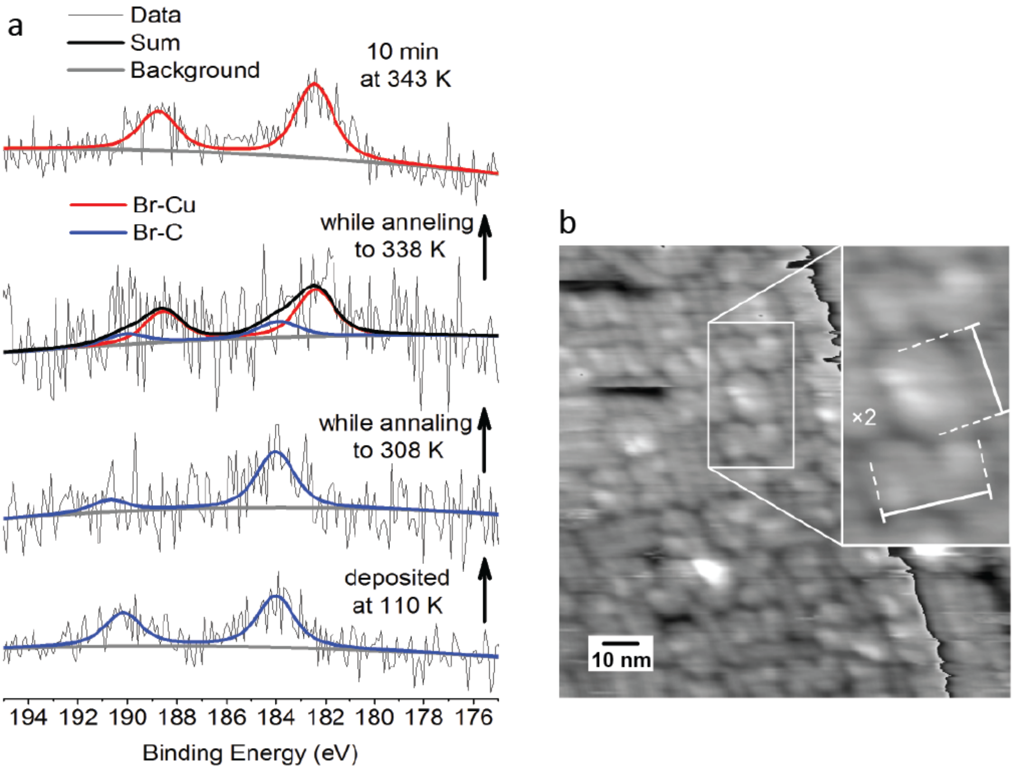

Figure 6.5: a) Br3p XP spectra of ~1 ML of bromo[4]helicene evaporated and annealed onto the oxidized Cu(100) surface. The background has been subtracted from a clean O/Cu(100) surface. The Br3p$_{3/2}$ peak position shifts from 184.0 eV (labeled in blue) to 182.4 eV (labeled in red) between 308 K and 338 K. b) STM image measured at 130 K (12.7 nm × 12.7 nm, 1.5 V, 10 pA) acquired on this sample after annealing to 463 K. The image's gray scale is folded across the step edge for clarification. The *anti*- and *syn*-bishelicenes have lengths of 16.5 ± 0.6 Å and 15.5 ± 0.5 Å, respectively. The method to determine the length has been indicated in the inset.

In conclusion, in the case of 2-bromo[4]-helicenes, the Ullmann reaction on copper surfaces leads only to homochiral bishelicenes, with their two ends spiraling away from the surface. The two enantiomers of the produced bishelicenes assemble into conglomerates of homochiral domains. *Syn*-bishelicene diastereomers are only for organometallic intermediates observed.

6.2 Trishelicenes from 2,3 -dibromo[4]helicene on Au(111)

The 2,3-dibromo[4]helicene molecule **3** (Scheme 6.2) is a [4]helicene with two bromine atoms at adjacent substitution sites at the end of the helix. When undergoing Ullmann coupling, it is possible that three of **3** couple into a trimer **4** or **5** by forming a new hexagon ring (indicated with the green dots). A similar reaction to form a 6-membered ring in a trimeric fashion has been reported [186,187], where 2,3-dibromoanthracene was used and tris-product were observed on Au (111) after Ullmann coupling.

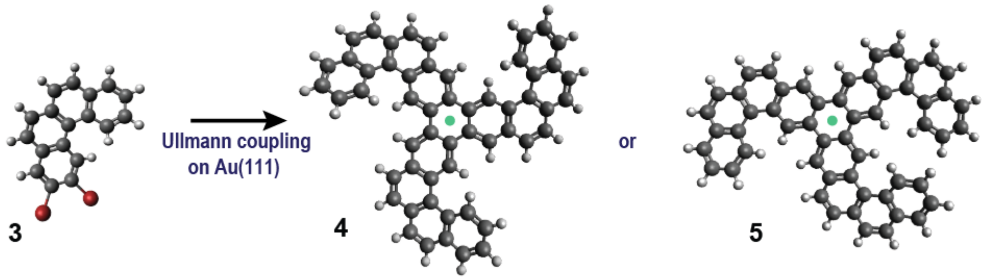

Scheme 6.2: 2,3-dibromo[4]helicene molecules **3** couple to each other in a trimeric fashion, leading to the primary product of a threefold chiral wheel-shaped molecule **4** or **5**. The green dots label the newly formed six-membered ring.

Unlike the case of 2,3-dibromoanthracene, where there is only one possible tris-product after coupling, one can think of diastereomers as possible products in the case of 2,3-dibromo[4]helicene after the Ullmann coupling. Namely, one helical arm could spiral into the opposite direction with respect to two other arms (see species **5** in Scheme 6.2). Thus, there are four diastereomers (*PPP, MMM, MMP, PPM*) that could form in this Ullmann reaction. Other than for bishelicene discussed above, these conformational configurations are not interchangeable. Although, the inversion barrier of the helix is still very low, the intermolecular *syn*- or *anti*-arrangments are fixed due to two covalent bonds.

At first the Au(111) surface was chosen, as it is known that it supports Ullmann coupling as well, but provides higher mobility for the organic product. In addition, it allows desorption of bromine at elevated temperature, which is not possible on copper surfaces. A full monolayer of **3** was deposited on Au(111), and subsequently annealed to 473 K for 10 minutes. XPS was measured at RT. The STM images were recorded at 108 K.

XPS (Figure 6.6) shows the Br3p peaks before and after annealing to 423 K. The $Br3p_{3/2}$ peak experiences a down-shift from 183.6 eV to 182 eV. This peak shift corresponds to the scission of Br-C bond. This feature is consistent with previous results with 2-bromo[4]helicene [33]. As Au-adatoms have a lower reactivity, the molecules remain intact upon evaporation onto Au at room temperature and the temperature needed to dissociate Br atoms from the molecule is higher on gold than on Cu surfaces. This dissociation temperature is consistent with previous reports for Ullmann coupling on Au(111) [181,188–190].

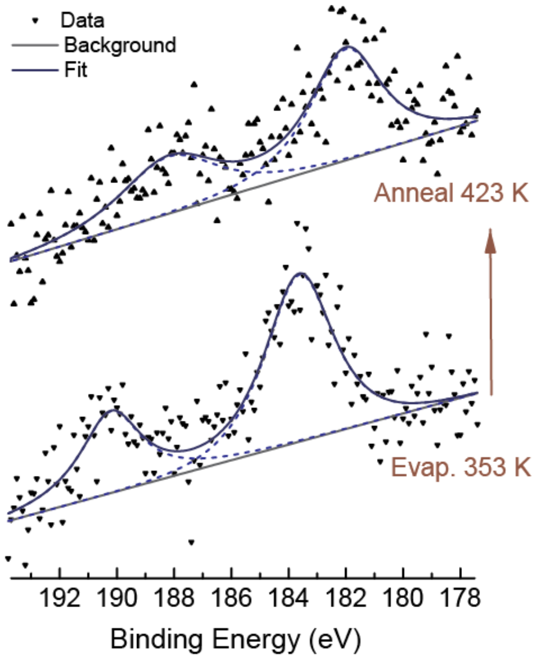

Figure 6.6: XP spectra of the Br3p region after deposition of **3** onto Au(111) at 353 K, and subsequent annealing to 423 K. The 3p electron binding energies reveal characteristic chemical states of the bromine atoms.

Figure 6.7 shows the STM images of the sample after annealing to 473 K, and was recorded at 108 K. There is a large self-assembled domain consisting of only **4** as carbon-containing product (Figure 6.7). In addition, there are Br atoms between trishelicenes. This domain is approximately 200 nm in diameter and is surrounded with a low-ordered area, which is covered by other species. In the entire domain there are trishelicenes, appearing as counterclockwise pinwheels, surrounded by Br atoms. The ratio of the molecules **4** and Br atoms is exactly 1:6, which corresponds precisely to three dibromo-helicenes **3** before the reaction. Such an assembled domain, which consisted only of clockwise chiral pinwheels of **4**, is also found on other areas in this sample (see Appendix). Under this scanning condition, the trimers are scanned as flat stars. A closer look at its chemical structure reveals that each star has 13 benzene rings in total. It is not clear how the helix in each of the three terminal benzo groups relax itself, whether they point away from the surface or not, judging by this images. Naturally, it can be assumed that all the helix spiral out of plane, as shown in Figure 6.7c, because this way there are 10 benzene rings that can align according to the underneath lattice.

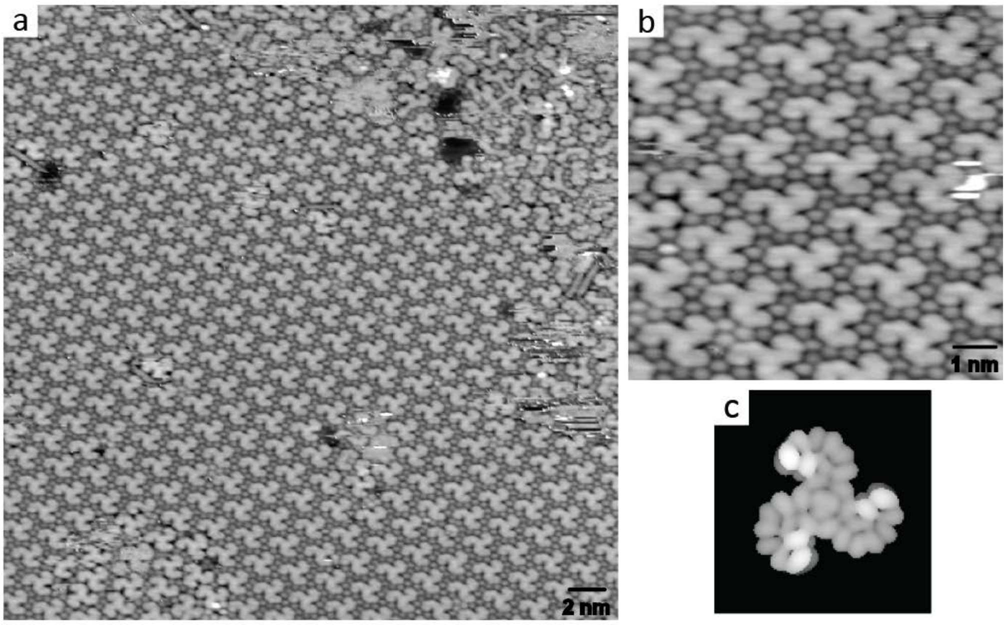

Figure 6.7: STM image (35 nm x 35 nm, 4.8 mV, 160 pA) recorded at 108 K on Au(111) after prior annealing to 473 K. a) Large homochiral domain of crystalized stars **4** surrounded by Br atoms. b) STM image (9 nm x 9 nm, 3.6 mV, 150 pA) of the self-assembled layer consisting of **4** and Br atoms. c) Unoccupied frontier orbitals of **4** simulated using extended Hückel theory, with the three benzo tips farthest away from the surface.

In addition to homochiral trisheciene, other products are observed on this surface, including bis- and tetrakis products. They are found basically only in low-ordered, but densely packed areas, including Br atoms (Figure 6.8). There are lines observed that are not identified, presumably impurities in the precursor material. A closer look at this region (Figure 6.8b) reveals detailed structures of these other species. Some of them are likely to be *PPM* and *MPP* diastereomers **5** (green ellipses). Besides homochiral trishelicene, there are also diasteriomeric bis-species with a cyclobutadiene ring, either heterochiral (**6**, pink ellipses) or homochiral (**7**, blue ellipses) or even with four helical units (8, yellow ellipse). For the latter, a metal-organic species with a single gold atom in the center is proposed. Accordingly, the STM image shows bright contrast in the center. Many dimers could also be found within the disordered area, the typical ones are *pm* dimer **6** and *pp* or *mm* dimer **7**. These dimers are the consequence of C-C bond formation of two [4]helicenes.

There was also one tetramer observed (in yellow circle). Since it is very unlikely that an 8-fold ring can form, the exact chemical structure cannot be determined. Notably, there is a bright protrusion in the center of this species, which appeared to be extremely similar to the organometallic compound 2,2-binaphthalene [191]. Thus this observed tetramer is probably an organometallic tetra-[4]helicene fused by a metal atom in the center, as shown in the figure.

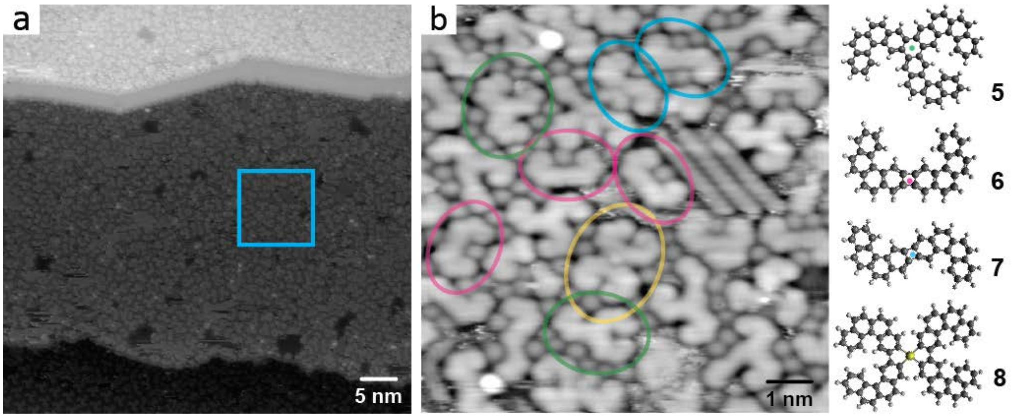

Figure 6.8: a) STM image of a low-ordered area with different product species. The blue square marks the location of image b. b) Different products of the reaction are labeled with ellipses and possible structures have been proposed: *PPM* and *PMM* trishelicenes (**5**, green), *PM* dimers (**6**, pink) plus *PP* and *MM* dimer (**7**, blue). The yellow ellipse is tetrakis product, and its possible organometallic structure is indicated (**8**). Image sizes and scanning parameters: (a) 60 nm × 60 nm, 6.7 mV, 190 pA; (b) 9.3 nm × 9.3 nm, 4.6 mV, 160 pA.

In some areas, another types of self-assembly is observed (shown in Appendix iv). They are mostly likely to be Br atoms. As Br atoms have a lower diffusion barrier than the molecules, they conglomerated and crystalize into domains.

6.3 Conclusion and Outlook

Stereoselective Ullmann coupling reactions have been realized using bromo-helicene molecules on metal surfaces. 2-bromo[4]helicenes couple into a dimer by forming a new single C-C bond. The centers of the product molecules are close parallel to the surface and the helix ends point away from the surface. 2,3-dibromo[4]helicenes form a tris-helicene product by generating a new C6 aromatic ring on Au(111). In both cases of dimerization or trimerization, homochiral combinations of the precursors are observed and the produced enantiomers assemble into 2D conglomerates of homochiral domains. More experiments on a helicenes with a higher helix-inversion barrier can be helpful in providing more insights on the topic of controllable covalent on-surface chemistry.

One idea is using dibromo-pentahelicene molecules, to perform Ullmann coupling and dehydrogenation in a highly controlled fashion (shown in scheme 6.3). Ullmann coupling produce the tris-product, which then forms by dehydrogenation a tris-coronene. Such end product has 22 aromatic rings in total but has still three tetrahelical features – a chiral graphene flake molecule!

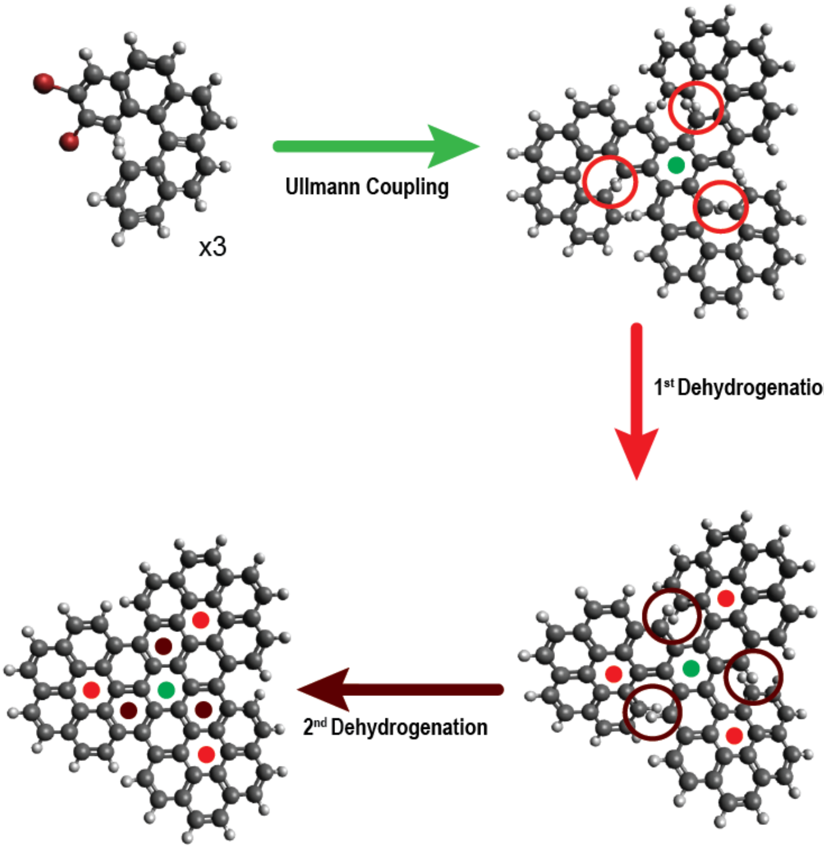

Scheme 6.3: Scheme showing Ullmann coupling and dehydrogenation reactions starting with 2,3-dibromo[5]helicene. Ullmann coupling will generate a new aromatic ring (labeled by the green dot) like in the case of [4]helicene. Then three C-C bonds will form via the 1st step dehydrogenation and thus three new benzene rings are formed (shown in bright red circles and dots). Afterwards the adjacent three pairs of overlapping hydrogen atoms can be form three more C-C bonds and thus lead to three new aromatic rings (labeled by dark red circles and dots). At the rim, there are still three points with steric overcrowding similar as in tetrahelicene.

Appendix

i. Atomic composition of different samples in potassium atoms per COR molecule deposited on Cu(111) kept at 90 K. Highlighted numbers show the stable ratio of 4 at or close to 400 K annealing temperature.

	#1: K (4.8 A, 2 min) + COR (105 °C, 30 min)			**#2: COR (105°C, 30 min) + K (4.8 A, 2 min)**			**#3: COR (105°C, 30 min) + K (4.8A, 1min)**		
	K	Cu	O	K	Cu	O	K	Cu	O
90 K	4.9	1.5	-	5.7	3.2	0.4	1.5	6.2	-
300 K	4.7	4.5	-	4.8	4.0	0.5	2.5	15.8	0.5
350 K	4.7	3.3	0.63	4.6	3.7	0.9	4.6	30.3	0.7
400 K	4.1	2.8	1.0	4.3	4.1	0.7	4.4	37.8	-
450 K	4.3	7.6	1.6	3.5	11.7	0.9	5.6	53.8	0.7
500 K	3.7	9.8	1.4	3.8	21.7	0.5	5.2	72.8	-

	#4: COR (105°C, 30 min) + K (4.8A, 1min)			**#5: COR (105°C, 30 min) + K (4.8A, 5min)**			**#6: COR (105°C, 30min) +K (4.8A, 5min)**		
	K	Cu	O	K	Cu	O	K	Cu	O
90 K	3.6	5.5	-	10.2	2.1	-	9.0	2.5	-
300 K	3.4	5.0	-	5.0	4.2	0.5	4.7	4.5	0.5
350 K	3.8	4.9	0.5	4.6	4.2	0.5	4.6	4.7	0.6
400 K	3.9	4.9	0.5	4.1	4.5	0.7	4.1	4.9	1.0
450 K	-	-	-	-	-	-	4.0	14.1	0.7
500 K	-	-	-	-	-	-	-	-	-

	#7: K (4.8A, 5min) +COR (105 °C, 30min)			**#8: K (5.2 A, 5 min) + COR (110 °C, 30 min)**			**#9: K (5.4 A, 5 min) + COR (110 °C, 30 min)**		
	K	Cu	O	K	Cu	O	K	Cu	O
90 K	4.6	0.7	-	4.23	0.11	-	6.15	-	-
300 K	4.6	6.4	-	4.13	1.16	(0.45)	5.36	1.11	(0.41)
350 K	4.7	5.7	0.5	4.23	2.17	(0.45)	4.66	2.89	(0.22)
400 K	3.8	4.8	0.7	3.54	2.27	(0.42)	4.14	2.55	(0.56)
450 K	3.6	12.6	0.5	3.04	6.56	(0.65)	-	-	-
500 K	-	-	-	-	-	-	-	-	-

	#10: K (5.4 A, 5 min) + COR (110°C, 30 min)		
	K	Cu	O
90 K	4.51	-	-
300 K	4.37	0.70	(0.30)
350 K	-	-	-
400 K	-	-	-
450 K	-	-	-
500 K	-	-	-

ii. Atomic composition of different samples in lithium atoms per COR molecule deposited on Cu(111) kept at 90 K.

	#1: COR (120 °C, 40 min) + Li (7 A, 5 min)			**#2: COR (120 °C, 60 min) + Li (7 A, 5 min)**			**#3: COR (120 °C, 90 min) + Li (7 A, 5 min)**		
	Li	**Cu**	**O**	**Li**	**Cu**	**O**	**Li**	**Cu**	**O**
90 K	6.0	-	-	6.3	-	-	5.4	-	-
300 K	4.8	0.05	0.6	4.5	-	0.4	4.2	-	0.4
350 K	6.4	0.3	0.6	6.2	0.3	0.7	-	-	-
400 K	7.8	0.7	0.9	-	-	-	-	-	-
450 K	-	-	-	-	-	-	-	-	-
500 K	8.3	1.3	0.8	-	-	-	-	-	-

	#4: COR (120 °C, 40 min) + Li (7A, 5 min)			**#5: COR (120 °C, 90 min) + Li (7 A, 3 min)**			**#6: COR (120 °C, 90 min) + Li (7 A, 3 min)**		
	Li	**Cu**	**O**	**Li**	**Cu**	**O**	**Li**	**Cu**	**O**
90 K	3.5	-	-	3.1			3.2	-	-
300 K	3.1	0.5		2.7	-	0.7	3.7	-	-
350 K	-	-	-	(4.4)	2.0	1.1	5.9	2.9	-
400 K	-	-	-	(7.5)	6.2	2.3	12.5	9.4	-
450 K	-	-	-	-	-	-	-	-	-
500 K	-	-	-	-	-	-	-	-	-

	#7: COR (120 °C, 120 min) + Li (7 A, 3 min)			**#8: COR (120 °C, 120 min) + Li (7 A, 3 min)**			**#9: COR (120 °C, 150 min) + Li (7 A, 3 min)**		
	Li	**Cu**	**O**	**Li**	**Cu**	**O**	**Li**	**Cu**	**O**
90 K	2.6	-	-	3.1	-	-	2.7	-	(0.2)
300 K	2.0	-	0.8	2.7	0.06	0.7	1.9	-	0.9
330 K	4.7	2.4	1.0	4.6	4.4	1.0	5.2	4.4	1.4

	#10: COR (120 °C, 150 min) + Li (7 A, 3 min)			**#11: COR (120 °C, 180 min) + Li (7A, 3.5 min)**		
	Li	**Cu**	**O**	**Li**	**Cu**	**O**
90 K	2.2	-	-	3.2	-	-
300 K	-	-	-	2.9	-	-
310 K	-	-	-	3.1	0.1	1.0
320 K	-	-	-	4.3	1.1	1.1
330 K	5.7	4.9	1.3	5.8	2.1	1
350 K	9.2	8.6	1.9	-	-	-
400 K	13.3	18.7	2.1	-	-	-

iii. A large domain of clockwise trimer originated from *PPP* 2,3-bromo[4]helicene on Au(111) surface. STM recorded at 108 K. images size 18.6 nm x 18.6 nm, measured with U_t = 267 mV and I_t = 10 pA. Br atoms are not resolved under this tip condition.

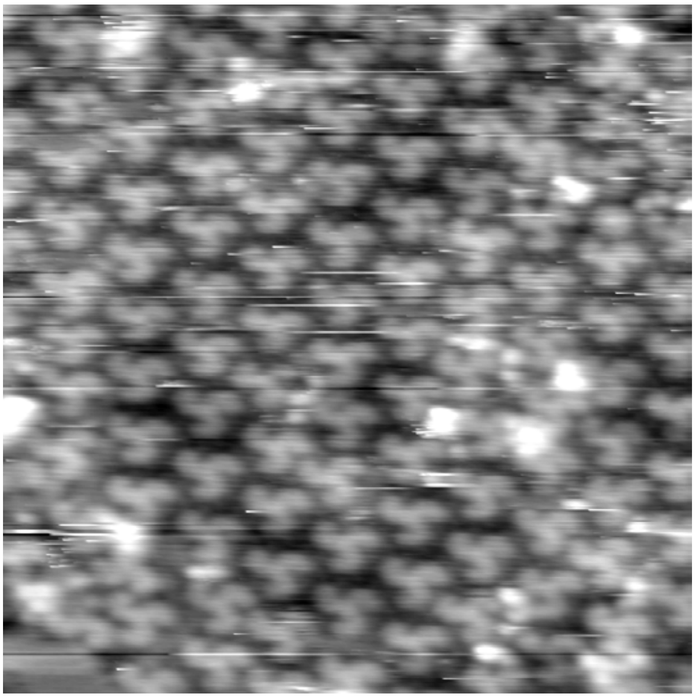

iv. A STM image showing Br atom assembly on a sample, made by evaporating 2,3-dibromo[4]helicene onto a Au(111) surface at room temperature, subsequently annealed to 473 K, and measured at 108K. Images size: 14 nm × 14 nm. Scanning parameters: U_t = 10.7 mV, I_t = 80 pA.

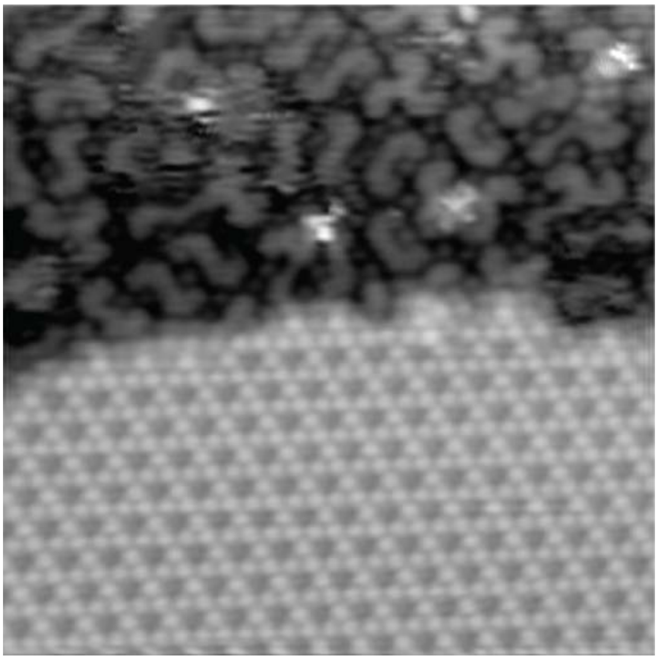

References

1 J. M. Gottfried, K. Flechtner, A. Kretschmann, T. Lukasczyk and H.-P. Steinrück, Direct Synthesis of a Metalloporphyrin Complex on a Surface, *J. Am. Chem. Soc.*, 2006, **128**, 5644–5645.

2 S. Lin, C. S. Diercks, Y.-B. Zhang, N. Kornienko, E. M. Nichols, Y. Zhao, A. R. Paris, D. Kim, P. Yang, O. M. Yaghi and C. J. Chang, Covalent organic frameworks comprising cobalt porphyrins for catalytic CO_2 reduction in water, *Science*, 2015, **349**, 1208–1213.

3 A. B. Sorokin, Phthalocyanine Metal Complexes in Catalysis, *Chem. Rev.*, 2013, **113**, 8152–8191.

4 Y. Gurdal, S. Luber, J. Hutter and M. Iannuzzi, Non-innocent adsorption of Co-pyrphyrin on rutile(110), *Phys. Chem. Chem. Phys.*, 2015, **17**, 22846–22854.

5 K. Baberschke, Magnetic switching of Fe-porphyrin molecules adsorbed on surfaces: An XAFS and XMCD study, *J. Phys. Conf. Ser.*, 2009, **190**, 012012.

6 M. E. Ali, B. Sanyal and P. M. Oppeneer, Tuning the Magnetic Interaction between Manganese Porphyrins and Ferromagnetic Co Substrate through Dedicated Control of the Adsorption, *J. Phys. Chem. C*, 2009, **113**, 14381–14383.

7 C. Wäckerlin, D. Chylarecka, A. Kleibert, K. Müller, C. Iacovita, F. Nolting, T. A. Jung and N. Ballav, Controlling spins in adsorbed molecules by a chemical switch, *Nat. Commun.*, 2010, **1**, 1–7.

8 N. Ballav, C. Wäckerlin, D. Siewert, P. M. Oppeneer and T. A. Jung, Emergence of On-Surface Magnetochemistry, *J. Phys. Chem. Lett.*, 2013, **4**, 2303–2311.

9 C. Wäckerlin, K. Tarafder, J. Girovsky, J. Nowakowski, T. Hählen, A. Shchyrba, D. Siewert, A. Kleibert, F. Nolting, P. M. Oppeneer, T. A. Jung and N. Ballav, Ammonia Coordination Introducing a Magnetic Moment in an On-Surface Low-Spin Porphyrin, *Angew. Chem. Int. Ed.*, 2013, **52**, 4568–4571.

10 D. den Boer, M. Li, T. Habets, P. Iavicoli, A. E. Rowan, R. J. M. Nolte, S. Speller, D. B. Amabilino, S. De Feyter and J. A. A. W. Elemans, Detection of different oxidation states of individual manganese porphyrins during their reaction with oxygen at a solid/liquid interface, *Nat. Chem.*, 2013, **5**, 621–627.

11 N. T. M. Hai, S. Furukawa, T. Vosch, S. D. Feyter, P. Broekmann and K. Wandelt, Electrochemical reactions at a porphyrin–copper interface, *Phys. Chem. Chem. Phys.*, 2009, **11**, 5422–5430.

12 J. S. Foster and J. E. Frommer, Imaging of liquid crystals using a tunnelling microscope, *Nature*, 1988, **333**, 542–545.

13 J. P. Rabe and S. Buchholz, Commensurability and Mobility in Two-Dimensional Molecular Patterns on Graphite, *Science*, 1991, **253**, 424–427.

14 J. Li, C. Wäckerlin, S. Schnidrig, E. Joliat, R. Alberto and K.-H. Ernst, On-Surface Metalation and 2D Self-Assembly of Pyrphyrin Molecules Into Metal-Coordinated Networks on Cu(111), *Helv. Chim. Acta*, 2017, **100**, e1600278.

15 T. A. Jung, R. R. Schlittler and J. K. Gimzewski, Conformational identification of individual adsorbed molecules with the STM, *Nature*, 1997, **386**, 696–698.

16 J.-M. Lehn, Supramolecular Chemistry—Scope and Perspectives Molecules, Supermolecules, and Molecular Devices (Nobel Lecture), *Angew. Chem. Int. Ed. Engl.*, 1988, **27**, 89–112.

17 J.-M. Lehn, Perspectives in Supramolecular Chemistry—From Molecular Recognition towards Molecular Information Processing and Self-Organization, *Angew. Chem. Int. Ed. Engl.*, 1990, **29**, 1304–1319.

18 B. F. Machado and P. Serp, Graphene-based materials for catalysis, *Catal. Sci. Technol.*, 2011, **2**, 54–75.

19 D. Datta, J. Li, N. Koratkar and V. B. Shenoy, Enhanced lithiation in defective graphene, *Carbon*, 2014, **80**, 305–310.

20 D. Er, E. Detsi, H. Kumar and V. B. Shenoy, Defective Graphene and Graphene Allotropes as High-Capacity Anode Materials for Mg Ion Batteries, *ACS Energy Lett.*, 2016, **1**, 638–645.

21 L. E. Dinca, F. De Marchi, J. M. MacLeod, J. Lipton-Duffin, R. Gatti, D. Ma, D. F. Perepichka and F. Rosei, Pentacene on Ni(111): room-temperature molecular packing and temperature-activated conversion to graphene, *Nanoscale*, 2015, **7**, 3263–3269.

22 X. Wan, K. Chen, D. Liu, J. Chen, Q. Miao and J. Xu, High-Quality Large-Area Graphene from Dehydrogenated Polycyclic Aromatic Hydrocarbons, *Chem. Mater.*, 2012, **24**, 3906–3915.

23 F. Ullmann and J. Bielecki, Ueber Synthesen in der Biphenylreihe, *Berichte Dtsch. Chem. Ges.*, 1901, **34**, 2174–2185.

24 M. Xi and B. E. Bent, Mechanisms of the Ullmann coupling reaction in adsorbed monolayers, *J. Am. Chem. Soc.*, 1993, **115**, 7426–7433.

25 L. Grill, M. Dyer, L. Lafferentz, M. Persson, M. V. Peters and S. Hecht, Nano-architectures by covalent assembly of molecular building blocks, *Nat. Nanotechnol.*, 2007, **2**, 687–691.

26 M. Bieri, M. Treier, J. Cai, K. Aït-Mansour, P. Ruffieux, O. Gröning, P. Gröning, M. Kastler, R. Rieger, X. Feng, K. Müllen and R. Fasel, Porous graphenes: two-dimensional polymer synthesis with atomic precision, *Chem. Commun.*, 2009, **0**, 6919–6921.

27 M. M. Blake, S. U. Nanayakkara, S. A. Claridge, L. C. Fernández-Torres, E. C. H. Sykes and P. S. Weiss, Identifying Reactive Intermediates in the Ullmann Coupling Reaction by Scanning Tunneling Microscopy and Spectroscopy, *J. Phys. Chem. A*, 2009, **113**, 13167–13172.

28 J. A. Lipton-Duffin, O. Ivasenko, D. F. Perepichka and F. Rosei, Synthesis of Polyphenylene Molecular Wires by Surface-Confined Polymerization, *Small*, 2009, **5**, 592–597.

29 J. Cai, P. Ruffieux, R. Jaafar, M. Bieri, T. Braun, S. Blankenburg, M. Muoth, A. P. Seitsonen, M. Saleh, X. Feng, K. Müllen and R. Fasel, Atomically precise bottom-up fabrication of graphene nanoribbons, *Nature*, 2010, **466**, 470–473.

30 Q. Fan, C. Wang, Y. Han, J. Zhu, W. Hieringer, J. Kuttner, G. Hilt and J. M. Gottfried, Surface-Assisted Organic Synthesis of Hyperbenzene Nanotroughs, *Angew. Chem. Int. Ed.*, 2013, **52**, 4668–4672.

31 P. Ruffieux, S. Wang, B. Yang, C. Sánchez-Sánchez, J. Liu, T. Dienel, L. Talirz, P. Shinde, C. A. Pignedoli, D. Passerone, T. Dumslaff, X. Feng, K. Müllen and R. Fasel, On-surface synthesis of graphene nanoribbons with zigzag edge topology, *Nature*, 2016, **531**, 489–492.

32 Q. Fan, T. Wang, J. Dai, J. Kuttner, G. Hilt, J. M. Gottfried and J. Zhu, On-Surface Pseudo-High-Dilution Synthesis of Macrocycles: Principle and Mechanism, *ACS Nano*, 2017, **11**, 5070–5079.

33 C. Wäckerlin, J. Li, A. Mairena, K. Martin, N. Avarvari and K.-H. Ernst, Surface-assisted diastereoselective Ullmann coupling of bishelicenes, *Chem. Commun.*, 2016, **52**, 12694–12697.

34 C. Nordling and K. Siegbahn, A New Precision Spectroscopy of Atoms and Molecules, *Rev. Roum. Phys.*, 1966, **11**, 797-.

35 K. Siegbahn, D. Hammond, H. Fellner-Feldegg and E. F. Barnett, Electron Spectroscopy with Monochromatized X-rays, *Science*, 1972, **176**, 245–252.

36 J. C. Vickerman and I. Gilmore, *Surface Analysis: The Principal Techniques*, Wiley, 2009.

37 G. Binnig and H. Rohrer, Scanning Tunneling Microscopy, *Helvetica Phys. Acta*, 1982, **55**, 726–735.

38 G. Binnig, H. Rohrer, C. Gerber and E. Weibel, Surface Studies by Scanning Tunneling Microscopy, *Phys. Rev. Lett.*, 1982, **49**, 57–61.

39 G. Binnig, H. Rohrer, C. Gerber and E. Weibel, Tunneling through a controllable vacuum gap, *Appl. Phys. Lett.*, 1982, **40**, 178–180.

40 P. Hansma and J. Tersoff, Scanning Tunneling Microscopy, *J. Appl. Phys.*, 1987, **61**, R1–R23.

41 C. J. Chen, *Introduction to Scanning Tunneling Microscopy*, Oxford University Press, 2007.

42 I. Horcas, R. Fernández, J. M. Gómez-Rodríguez, J. Colchero, J. Gómez-Herrero and A. M. Baro, WSXM: A software for scanning probe microscopy and a tool for nanotechnology, *Rev. Sci. Instrum.*, 2007, **78**, 013705.

43 P. A. Redhead, Thermal desorption of gases, *Vacuum*, 1962, **12**, 203–211.

44 M. Polanyi and E. Wigner, Bildung und Zerfall von Molekülen, *Z. Für Phys.*, 1925, **33**, 429–434.

45 X. Li, F. Kang and M. Inagaki, Buckybowls: Corannulene and Its Derivatives, *Small*, 2016, **12**, 3206–3223.

46 A. M. Butterfield, B. Gilomen and J. S. Siegel, Kilogram-Scale Production of Corannulene, *Org. Process Res. Dev.*, 2012, **16**, 664–676.

47 M. J. Buerger, *Elementary crystallography: an introduction to the fundamental geometrical features of crystals*, John Wiley and Sons, 1967.

48 L. Merz, M. Parschau, J. S. Siegel and K.-H. Ernst, Condensation of Fivefold-Symmetric Molecules in Two Dimensions, *Chim. Int. J. Chem.*, 2009, **63**, 214–216.

49 L. Merz, M. Parschau, L. Zoppi, K. K. Baldridge, J. S. Siegel and K.-H. Ernst, Reversible Phase Transitions in a Buckybowl Monolayer, *Angew. Chem. Int. Ed.*, 2009, **48**, 1966–1969.

50 M. Parschau, R. Fasel, K.-H. Ernst, O. Gröning, L. Brandenberger, R. Schillinger, T. Greber, A. P. Seitsonen, Y.-T. Wu and J. S. Siegel, Buckybowls on Metal Surfaces: Symmetry Mismatch and Enantiomorphism of Corannulene on Cu(110), *Angew. Chem. Int. Ed.*, 2007, **46**, 8258–8261.

51 T. Bauert, L. Merz, D. Bandera, M. Parschau, J. S. Siegel and K.-H. Ernst, Building 2D Crystals from 5-Fold-Symmetric Molecules, *J. Am. Chem. Soc.*, 2009, **131**, 3460–3461.

52 M. J. Rosseinsky, A. P. Ramirez, S. H. Glarum, D. W. Murphy, R. C. Haddon, A. F. Hebard, T. T. M. Palstra, A. R. Kortan, S. M. Zahurak and A. V. Makhija, Superconductivity at 28 K in RbxC60, *Phys. Rev. Lett.*, 1991, **66**, 2830–2832.

53 A. Y. Ganin, Y. Takabayashi, Y. Z. Khimyak, S. Margadonna, A. Tamai, M. J. Rosseinsky and K. Prassides, Bulk superconductivity at 38 K in a molecular system, *Nat. Mater.*, 2008, **7**, 367–371.

54 R. Mitsuhashi, Y. Suzuki, Y. Yamanari, H. Mitamura, T. Kambe, N. Ikeda, H. Okamoto, A. Fujiwara, M. Yamaji, N. Kawasaki, Y. Maniwa and Y. Kubozono, Superconductivity in alkali-metal-doped picene, *Nature*, 2010, **464**, 76–79.

55 M. Baumgarten, L. Gherghel, M. Wagner, A. Weitz, M. Rabinovitz, P.-C. Cheng and L. T. Scott, Corannulene Reduction: Spectroscopic Detection of All Anionic Oxidation States, *J. Am. Chem. Soc.*, 1995, **117**, 6254–6257.

56 A. S. Filatov, A. V. Zabula, S. N. Spisak, A. Y. Rogachev and M. A. Petrukhina, Clamshell Opening in the Mixed-Metal Supramolecular Aggregates Formed by Fourfold Reduced Corannulene for Maximizing Intercalated Metal Content, *Angew. Chem.-Int. Ed.*, 2014, **53**, 140–145.

57 A. V. Zabula, S. N. Spisak, A. S. Filatov and M. A. Petrukhina, Pentadecker Supramolecules with a Lithium Alkoxo Nanobelt Sandwiched between Two Highly Charged Buckybowl Surfaces, *Angew. Chem. Int. Ed.*, 2012, **51**, 12194–12198.

58 A. V. Zabula, S. N. Spisak, A. S. Filatov and M. A. Petrukhina, Self-Assembly of Charged Supramolecular Sandwiches Formed by Corannulene Tetraanions and Lithium Cations, *Organometallics*, 2012, **31**, 5541–5545.

59 T. Kato and T. Yamabe, Electron–intramolecular-phonon coupling and possible superconductivity in negatively charged coronene and corannulene, *J. Chem. Phys.*, 2002, **117**, 2324–2331.

60 T. E. Bauert, L. Zoppi, G. Koller, J. S. Siegel, K. K. Baldridge and K.-H. Ernst, Quadruple anionic buckybowls by solid-state chemistry of corannulene and cesium, *J. Am. Chem. Soc.*, 2013, **135**, 12857–12860.

61 R. Dudde, K. Frank and B. Reihl, Unoccupied Electronic Band-Structure of an Ordered

Potassium Layer on Copper - Cu(111)-(2x2)k, *Phys. Rev. B*, 1990, **41**, 4897–4900.

62 K. H. Ernst and C. T. Campbell, A reversal in dipole moment for adsorbed hydrocarbons on Pt(111) due to coadsorbed alkali, *Surf. Sci. Lett.*, 1991, **259**, L736–L738.

63 J. F. Moulder, *Handbook of X-ray Photoelectron Spectroscopy: A Reference Book of Standard Spectra for Identification and Interpretation of XPS Data*, Physical Electronics Division, Perkin-Elmer Corporation, 1992.

64 T. Bauert, Ph.D Dissertation, University of Zurich, 2011.

65 L. Zhang, Y. Ye, D. Cheng, H. Pan and J. Zhu, Intercalation of Li at the Graphene/Cu Interface, *J. Phys. Chem. C*, 2013, **117**, 9259–9265.

66 W. Auwärter, D. Écija, F. Klappenberger and J. V. Barth, Porphyrins at interfaces, *Nat. Chem.*, 2015, **7**, 105–120.

67 J. M. Gottfried, Surface chemistry of porphyrins and phthalocyanines, *Surf. Sci. Rep.*, 2015, **70**, 259–379.

68 K. Diller, A. C. Papageorgiou, F. Klappenberger, F. Allegretti, J. V. Barth and W. Auwärter, In vacuo interfacial tetrapyrrole metallation, *Chem Soc Rev*, 2016, **45**, 1629–1656.

69 K. Flechtner, A. Kretschmann, H.-P. Steinrück and J. M. Gottfried, NO-Induced Reversible Switching of the Electronic Interaction between a Porphyrin-Coordinated Cobalt Ion and a Silver Surface, *J. Am. Chem. Soc.*, 2007, **129**, 12110–12111.

70 N. Ballav, C. Wäckerlin, D. Siewert, P. M. Oppeneer and T. A. Jung, Emergence of On-Surface Magnetochemistry, *J. Phys. Chem. Lett.*, 2013, **4**, 2303–2311.

71 B. Wurster, D. Grumelli, D. Hötger, R. Gutzler and K. Kern, Driving the Oxygen Evolution Reaction by Nonlinear Cooperativity in Bimetallic Coordination Catalysts, *J. Am. Chem. Soc.*, 2016, **138**, 3623–3626.

72 J. M. Gottfried, K. Flechtner, A. Kretschmann, T. Lukasczyk and H.-P. Steinrück, Direct Synthesis of a Metalloporphyrin Complex on a Surface, *J. Am. Chem. Soc.*, 2006, **128**, 5644–5645.

73 W. Auwärter, A. Weber-Bargioni, S. Brink, A. Riemann, A. Schiffrin, M. Ruben and J. V. Barth, Controlled Metalation of Self-Assembled Porphyrin Nanoarrays in Two Dimensions, *ChemPhysChem*, 2007, **8**, 250–254.

74 J. Nowakowski, C. Wäckerlin, J. Girovsky, D. Siewert, T. A. Jung and N. Ballav, Porphyrin metalation providing an example of a redox reaction facilitated by a surface reconstruction, *Chem. Commun.*, 2013, **49**, 2347–2349.

75 S. Ogawa, R. Narushima and Y. Arai, Aza Macrocycle that selectively binds lithium ion with color change, *J. Am. Chem. Soc.*, 1984, **106**, 5760–5762.

76 E. Joliat, S. Schnidrig, B. Probst, C. Bachmann, B. Spingler, K. K. Baldridge, F. von Rohr, A. Schilling and R. Alberto, Cobalt complexes of tetradentate, bipyridine-based macrocycles: their structures, properties and photocatalytic proton reduction, *Dalton Trans*, 2016, **45**, 1737–1745.

77 R. Ibrahim, S. Tsuchiya and S. Ogawa, A Color-Switching Molecule: Specific Properties of New Tetraaza Macrocycle Zinc Complex with a Facile Hydrogen Atom, *J. Am. Chem. Soc.*, 2000, **122**, 12174–12185.

78 Z. Zhu, K. Takano, A. Furuhama, S. Ogawa and S. Tsuchiya, Theoretical Study of Geometries and Electronic Transition of Color-Switching Molecules: Tetra-Aza Macrocycle and Its Zinc Complexes, *Bull. Chem. Soc. Jpn.*, 2007, **80**, 686–693.

79 C. Pierre, J.-M. Vincent, J.-B. Verlhac, C. Courseille, A. Dautant and C. Mathoniere, First synthesis and crystal structure of a Mn3+ complex derived from the Ogawa porphyrin-like ligand, *New J. Chem.*, 2001, **25**, 522–524.

80 G. Mette, D. Sutter, Y. Gurdal, S. Schnidrig, B. Probst, M. Iannuzzi, J. Hutter, R. Alberto and J. Osterwalder, From porphyrins to pyrphyrins: adsorption study and metalation of a molecular catalyst on Au(111), *Nanoscale*, 2016, **8**, 7958–7968.

81 G. Pawin, K. L. Wong, D. Kim, D. Sun, L. Bartels, S. Hong, T. S. Rahman, R. Carp and M. Marsella, A Surface Coordination Network Based on Substrate-Derived Metal Adatoms with Local Charge Excess, *Angew. Chem. Int. Ed.*, 2008, **47**, 8442–8445.

82 A. Shchyrba, M.-T. Nguyen, C. Wäckerlin, S. Martens, S. Nowakowska, T. Ivas, J. Roose, T. Nijs, S. Boz, M. Schär, M. Stöhr, C. A. Pignedoli, C. Thilgen, F. Diederich, D. Passerone and T. A. Jung, Chirality Transfer in 1D Self-Assemblies: Influence of H-Bonding vs Metal Coordination between Dicyano[7]helicene Enantiomers, *J. Am. Chem. Soc.*, 2013, **135**, 15270–15273.

83 G. E. Pacchioni, M. Pivetta and H. Brune, Competing Interactions in the Self-Assembly of NC-Ph3-CN Molecules on Cu(111), *J. Phys. Chem. C*, 2015, **119**, 25442–25448.

84 M. Pivetta, G. E. Pacchioni, E. Fernandes and H. Brune, Temperature-dependent self-assembly of NC–Ph5–CN molecules on Cu(111), *J. Chem. Phys.*, 2015, **142**, 101928.

85 J. V. Barth, Fresh perspectives for surface coordination chemistry, *Surf. Sci.*, 2009, **603**, 1533–1541.

86 J. Xiao, S. Ditze, M. Chen, F. Buchner, M. Stark, M. Drost, H.-P. Steinrück, J. M. Gottfried and H. Marbach, Temperature-Dependent Chemical and Structural Transformations from 2H-tetraphenylporphyrin to Copper(II)-Tetraphenylporphyrin on Cu(111), *J. Phys. Chem. C*, 2012, **116**, 12275–12282.

87 M. Röckert, S. Ditze, M. Stark, J. Xiao, H.-P. Steinrück, H. Marbach and O. Lytken, Abrupt Coverage-Induced Enhancement of the Self-Metalation of Tetraphenylporphyrin with Cu(111), *J. Phys. Chem. C*, 2014, **118**, 1661–1667.

88 M. Röckert, M. Franke, Q. Tariq, D. Lungerich, N. Jux, M. Stark, A. Kaftan, S. Ditze, H. Marbach, M. Laurin, J. Libuda, H.-P. Steinrück and O. Lytken, Insights in Reaction Mechanistics: Isotopic Exchange during the Metalation of Deuterated Tetraphenyl-21,23 *D* -porphyrin on Cu(111), *J. Phys. Chem. C*, 2014, **118**, 26729–26736.

89 S. Ditze, M. Stark, M. Drost, F. Buchner, H.-P. Steinrück and H. Marbach, Activation Energy for the Self-Metalation Reaction of 2H-Tetraphenylporphyrin on Cu(111), *Angew. Chem. Int. Ed.*, 2012, **51**, 10898–10901.

90 C. Ruggieri, S. Rangan, R. A. Bartynski and E. Galoppini, Zinc(II) Tetraphenylporphyrin on Ag(100) and Ag(111): Multilayer Desorption and Dehydrogenation, *J. Phys. Chem. C*, 2016, **120**, 7575–7585.

91 A. Wiengarten, J. A. Lloyd, K. Seufert, J. Reichert, W. Auwärter, R. Han, D. A. Duncan, F. Allegretti, S. Fischer, S. C. Oh, Ö. Sağlam, L. Jiang, S. Vijayaraghavan, D. Écija, A. C. Papageorgiou and J. V. Barth, Surface-Assisted Cyclodehydrogenation; Break the Symmetry, Enhance the Selectivity, *Chem. - Eur. J.*, 2015, **21**, 12285–12290.

92 O. Snezhkova, F. Bischoff, Y. He, A. Wiengarten, S. Chaudhary, N. Johansson, K. Schulte, J. Knudsen, J. V. Barth, K. Seufert, W. Auwärter and J. Schnadt, Iron phthalocyanine on Cu(111): Coverage-dependent assembly and symmetry breaking, temperature-induced homocoupling, and modification of the adsorbate-surface interaction by annealing, *J. Chem. Phys.*, 2016, **144**, 094702.

93 G. Anger, A. Winkler and K. D. Rendulic, Adsorption and desorption kinetics in the systems H2/Cu(111), H2/Cu(110) and H2/Cu(100), *Surf. Sci.*, 1989, **220**, 1–17.

94 D. A. King, Thermal desorption from metal surfaces: A review, *Surf. Sci.*, 1975, **47**, 384–402.

95 A. M. de Jong and J. W. Niemantsverdriet, Thermal desorption analysis: Comparative test of ten commonly applied procedures, *Surf. Sci.*, 1990, **233**, 355–365.

96 J. E. Huheey, E. A. Keiter, R. L. Keiter and O. K. Medhi, *Inorganic Chemistry: Principles of Structure and Reactivity*, Pearson Education, 2006.

97 D. Kühne, F. Klappenberger, R. Decker, U. Schlickum, H. Brune, S. Klyatskaya, M. Ruben and J. V. Barth, High-Quality 2D Metal–Organic Coordination Network Providing Giant Cavities within Mesoscale Domains, *J. Am. Chem. Soc.*, 2009, **131**, 3881–3883.

98 U. Schlickum, F. Klappenberger, R. Decker, G. Zoppellaro, S. Klyatskaya, M. Ruben, K. Kern,

H. Brune and J. V. Barth, Surface-Confined Metal–Organic Nanostructures from Co-Directed Assembly of Linear Terphenyl-dicarbonitrile Linkers on Ag(111), *J. Phys. Chem. C*, 2010, **114**, 15602–15606.

99 M. Marschall, J. Reichert, A. Weber-Bargioni, K. Seufert, W. Auwärter, S. Klyatskaya, G. Zoppellaro, M. Ruben and J. V. Barth, Random two-dimensional string networks based on divergent coordination assembly, *Nat. Chem.*, 2010, **2**, 131–137.

100 T. A. Pham, F. Song, M. N. Alberti, M.-T. Nguyen, N. Trapp, C. Thilgen, F. Diederich and M. Stöhr, Heat-induced formation of one-dimensional coordination polymers on Au(111): an STM study, *Chem. Commun.*, 2015, **51**, 14473–14476.

101 K. W. Hipps, X. Lu, X. D. Wang and U. Mazur, Metal d-Orbital Occupation-Dependent Images in the Scanning Tunneling Microscopy of Metal Phthalocyanines, *J. Phys. Chem.*, 1996, **100**, 11207–11210.

102 X. Lu and K. W. Hipps, Scanning Tunneling Microscopy of Metal Phthalocyanines: d6 and d8 Cases, *J. Phys. Chem. B*, 1997, **101**, 5391–5396.

103 L. E. Dinca, F. De Marchi, J. M. MacLeod, J. Lipton-Duffin, R. Gatti, D. Ma, D. F. Perepichka and F. Rosei, Pentacene on Ni(111): room-temperature molecular packing and temperature-activated conversion to graphene, *Nanoscale*, 2015, **7**, 3263–3269.

104 F. Buchner, K. Flechtner, Y. Bai, E. Zillner, I. Kellner, H.-P. Steinrück, H. Marbach and J. M. Gottfried, Coordination of Iron Atoms by Tetraphenylporphyrin Monolayers and Multilayers on Ag(111) and Formation of Iron-Tetraphenylporphyrin, *J. Phys. Chem. C*, 2008, **112**, 15458–15465.

105 K. Diller, F. Klappenberger, M. Marschall, K. Hermann, A. Nefedov, C. Wöll and J. V. Barth, Self-metalation of 2H-tetraphenylporphyrin on Cu(111): An x-ray spectroscopy study, *J. Chem. Phys.*, 2012, **136**, 014705.

106 M. Wahl, M. Stöhr, H. Spillmann, T. A. Jung and L. H. Gade, Rotation–libration in a hierarchic supramolecular rotor–stator system: Arrhenius activation and retardation by local interaction, *Chem. Commun.*, 2007, **0**, 1349–1351.

107 R. Zhang, W.-Y. Yu, K.-Y. Wong and C.-M. Che, Highly Efficient Asymmetric Epoxidation of Alkenes with a D4-Symmetric Chiral Dichlororuthenium(IV) Porphyrin Catalyst, *J. Org. Chem.*, 2001, **66**, 8145–8153.

108 J. T. Groves and R. Quinn, Aerobic epoxidation of olefins with ruthenium porphyrin catalysts, *J. Am. Chem. Soc.*, 1985, **107**, 5790–5792.

109 E. Galardon, P. L. Maux and G. Simonneaux, Cyclopropanation of alkenes with ethyl diazoacetate catalysed byruthenium porphyrin complexes, *Chem. Commun.*, 1997, **0**, 927–928.

110 R. Zhang, W.-Y. Yu, T.-S. Lai and C.-M. Che, Enantioselective epoxidation of trans-disubstituted alkenes by D2-symmetric chiral dioxoruthenium(VI) porphyrins, *Chem. Commun.*, 1999, **0**, 409–410.

111 C. Ho, W.-H. Leung and C.-M. Che, Kinetics of C–H bond and alkene oxidation by trans-dioxoruthenium(VI) porphyrins, *J. Chem. Soc. Dalton Trans.*, 1991, 2933–2939.

112 A. C. Papageorgiou, K. Diller, S. Fischer, F. Allegretti, F. Klappenberger, S. C. Oh, Ö. Sağlam, J. Reichert, A. Wiengarten, K. Seufert, W. Auwärter and J. V. Barth, In Vacuo Porphyrin Metalation on Ag(111) via Chemical Vapor Deposition of Ru3(CO)12: Mechanistic Insights, *J. Phys. Chem. C*, 2016, **120**, 8751–8758.

113 K. S. Novoselov, A. K. Geim, S. V. Morozov, D. Jiang, Y. Zhang, S. V. Dubonos, I. V. Grigorieva and A. A. Firsov, Electric Field Effect in Atomically Thin Carbon Films, *Science*, 2004, **306**, 666–669.

114 X. Li, W. Cai, J. An, S. Kim, J. Nah, D. Yang, R. Piner, A. Velamakanni, I. Jung, E. Tutuc, S. K. Banerjee, L. Colombo and R. S. Ruoff, Large-Area Synthesis of High-Quality and Uniform Graphene Films on Copper Foils, *Science*, 2009, **324**, 1312–1314.

115 K. S. Kim, Y. Zhao, H. Jang, S. Y. Lee, J. M. Kim, K. S. Kim, J.-H. Ahn, P. Kim, J.-Y. Choi and B. H. Hong, Large-scale pattern growth of graphene films for stretchable transparent electrodes, *Nature*, 2009, **457**, 706–710.
116 Z. Luo, Y. Lu, D. W. Singer, M. E. Berck, L. A. Somers, B. R. Goldsmith and A. T. C. Johnson, Effect of Substrate Roughness and Feedstock Concentration on Growth of Wafer-Scale Graphene at Atmospheric Pressure, *Chem. Mater.*, 2011, **23**, 1441–1447.
117 C. Berger, Z. Song, X. Li, X. Wu, N. Brown, C. Naud, D. Mayou, T. Li, J. Hass, A. N. Marchenkov, E. H. Conrad, P. N. First and W. A. de Heer, Electronic Confinement and Coherence in Patterned Epitaxial Graphene, *Science*, 2006, **312**, 1191–1196.
118 T. Niu, M. Zhou, J. Zhang, Y. Feng and W. Chen, Growth Intermediates for CVD Graphene on Cu(111): Carbon Clusters and Defective Graphene, *J. Am. Chem. Soc.*, 2013, **135**, 8409–8414.
119 L. Lin and Z. Liu, Graphene synthesis: On-the-spot growth, *Nat. Mater.*, 2016, **15**, 9–10.
120 J. Lahiri, T. Miller, L. Adamska, I. I. Oleynik and M. Batzill, Graphene Growth on Ni(111) by Transformation of a Surface Carbide, *Nano Lett.*, 2011, **11**, 518–522.
121 J. Wintterlin and M.-L. Bocquet, Graphene on metal surfaces, *Surf. Sci.*, 2009, **603**, 1841–1852.
122L. Gao, J. R. Guest and N. P. Guisinger, Epitaxial Graphene on Cu(111), *Nano Lett.*, 2010, **10**, 3512–3516.
123 X. Li, C. W. Magnuson, A. Venugopal, R. M. Tromp, J. B. Hannon, E. M. Vogel, L. Colombo and R. S. Ruoff, Large-Area Graphene Single Crystals Grown by Low-Pressure Chemical Vapor Deposition of Methane on Copper, *J. Am. Chem. Soc.*, 2011, **133**, 2816–2819.
124 J. Coraux, A. T. N‘Diaye, C. Busse and T. Michely, Structural Coherency of Graphene on Ir(111), *Nano Lett.*, 2008, **8**, 565–570.
125 J. Coraux, A. T. N’Diaye, M. Engler, C. Busse, D. Wall, N. Buckanie, F.-J. M. zu Heringdorf, R. van Gastel, B. Poelsema and T. Michely, Growth of graphene on Ir(111), *New J. Phys.*, 2009, **11**, 023006.
126 L. Zhao, K. T. Rim, H. Zhou, R. He, T. F. Heinz, A. Pinczuk, G. W. Flynn and A. N. Pasupathy, Influence of copper crystal surface on the CVD growth of large area monolayer graphene, *Solid State Commun.*, 2011, **151**, 509–513.
127 K. Gharagozloo-Hubmann, N. S. Müller, M. Giersig, C. Lotze, K. J. Franke and S. Reich, Requirement on Aromatic Precursor for Graphene Formation, *J. Phys. Chem. C*, 2016, **120**, 9821–9825.
128 A. Hirsch, The era of carbon allotropes, *Nat. Mater.*, 2010, **9**, 868–871.
129 S. Zhang, J. Zhou, Q. Wang, X. Chen, Y. Kawazoe and P. Jena, Penta-graphene: A new carbon allotrope, *Proc. Natl. Acad. Sci.*, 2015, **112**, 2372–2377.
130 H. Terrones, M. Terrones, E. Hernández, N. Grobert, J.-C. Charlier and P. M. Ajayan, New Metallic Allotropes of Planar and Tubular Carbon, *Phys. Rev. Lett.*, 2000, **84**, 1716–1719.
131 C. P. Ewels, X. Rocquefelte, H. W. Kroto, M. J. Rayson, P. R. Briddon and M. I. Heggie, Predicting experimentally stable allotropes: Instability of penta-graphene, *Proc. Natl. Acad. Sci.*, 2015, **112**, 15609–15612.
132 E. A. Jackson, B. D. Steinberg, M. Bancu, A. Wakamiya and L. T. Scott, Pentaindenocorannulene and Tetraindenocorannulene: New Aromatic Hydrocarbon π Systems with Curvatures Surpassing That of C_{60}, *J. Am. Chem. Soc.*, 2007, **129**, 484–485.
133 S. Lampart, L. M. Roch, A. K. Dutta, Y. Wang, R. Warshamanage, A. D. Finke, A. Linden, K. K. Baldridge and J. S. Siegel, Pentaindenocorannulene: Properties, Assemblies, and C60 Complex, *Angew. Chem. Int. Ed.*, 2016, **55**, 14648–14652.
134 J. Gao, J. Yip, J. Zhao, B. I. Yakobson and F. Ding, Graphene Nucleation on Transition Metal Surface: Structure Transformation and Role of the Metal Step Edge, *J. Am. Chem. Soc.*, 2011, **133**, 5009–5015.
135 E. Loginova, N. C. Bartelt, P. J. Feibelman and K. F. McCarty, Evidence for graphene growth

by C cluster attachment, *New J. Phys.*, 2008, **10**, 093026.

136 Y.-Q. Zhang, N. Kepčija, M. Kleinschrodt, K. Diller, S. Fischer, A. C. Papageorgiou, F. Allegretti, J. Björk, S. Klyatskaya, F. Klappenberger, M. Ruben and J. V. Barth, Homo-coupling of terminal alkynes on a noble metal surface, *Nat. Commun.*, 2012, **3**, 1286.

137 K. A. Simonov, N. A. Vinogradov, A. S. Vinogradov, A. V. Generalov, E. M. Zagrebina, G. I. Svirskiy, A. A. Cafolla, T. Carpy, J. P. Cunniffe, T. Taketsugu, A. Lyalin, N. Mårtensson and A. B. Preobrajenski, From Graphene Nanoribbons on Cu(111) to Nanographene on Cu(110): Critical Role of Substrate Structure in the Bottom-Up Fabrication Strategy, *ACS Nano*, 2015, **9**, 8997–9011.

138 D. G. Matei, N.-E. Weber, S. Kurasch, S. Wundrack, M. Woszczyna, M. Grothe, T. Weimann, F. Ahlers, R. Stosch, U. Kaiser and A. Turchanin, Functional Single-Layer Graphene Sheets from Aromatic Monolayers, *Adv. Mater.*, 2013, **25**, 4146–4151.

139 M. Röckert, M. Franke, Q. Tariq, S. Ditze, M. Stark, P. Uffinger, D. Wechsler, U. Singh, J. Xiao, H. Marbach, H.-P. Steinrück and O. Lytken, Coverage- and Temperature-Dependent Metalation and Dehydrogenation of Tetraphenylporphyrin on Cu(111), *Chem. – Eur. J.*, 2014, **20**, 8948–8953.

140 J. Liu, T. Dienel, J. Liu, O. Groening, J. Cai, X. Feng, K. Müllen, P. Ruffieux and R. Fasel, Building Pentagons into Graphenic Structures by On-Surface Polymerization and Aromatic Cyclodehydrogenation of Phenyl-Substituted Polycyclic Aromatic Hydrocarbons, *J. Phys. Chem. C*, 2016, **120**, 17588–17593.

141 S. M. Hollen, G. A. Gambrel, S. J. Tjung, N. M. Santagata, E. Johnston-Halperin and J. A. Gupta, Modification of electronic surface states by graphene islands on Cu(111), *Phys. Rev. B*, 2015, **91**, 195425.

142 H. Kim, C. Mattevi, M. R. Calvo, J. C. Oberg, L. Artiglia, S. Agnoli, C. F. Hirjibehedin, M. Chhowalla and E. Saiz, Activation Energy Paths for Graphene Nucleation and Growth on Cu, *ACS Nano*, 2012, **6**, 3614–3623.

143 A. Luican-Mayer, J. E. Barrios-Vargas, J. T. Falkenberg, G. Autès, A. W. Cummings, David Soriano, G. Li, M. Brandbyge, O. V. Yazyev, S. Roche and E. Y. Andrei, Localized electronic states at grain boundaries on the surface of graphene and graphite, *2D Mater.*, 2016, **3**, 031005.

144 H. Yang, A. J. Mayne, M. Boucherit, G. Comtet, G. Dujardin and Y. Kuk, Quantum Interference Channeling at Graphene Edges, *Nano Lett.*, 2010, **10**, 943–947.

145 E. Cockayne, G. M. Rutter, N. P. Guisinger, J. N. Crain, P. N. First and J. A. Stroscio, Grain boundary loops in graphene, *Phys. Rev. B*, 2011, **83**, 195425.

146 M. M. Ugeda, I. Brihuega, F. Guinea and J. M. Gómez-Rodríguez, Missing Atom as a Source of Carbon Magnetism, *Phys. Rev. Lett.*, 2010, **104**, 096804.

147 A. R. Botello-Méndez, S. M.-M. Dubois, A. Lherbier and J.-C. Charlier, Achievements of DFT for the Investigation of Graphene-Related Nanostructures, *Acc. Chem. Res.*, 2014, **47**, 3292–3300.

148 G. Mándi and K. Palotás, Chen's derivative rule revisited: Role of tip-orbital interference in STM, *Phys. Rev. B*, 2015, **91**, 165406.

149 E. Cockayne, Graphing and grafting graphene: Classifying finite topological defects, *Phys. Rev. B*, 2012, **85**, 125409.

150 Y. He, M. Garnica, F. Bischoff, J. Ducke, M.-L. Bocquet, M. Batzill, W. Auwärter and J. V. Barth, Fusing tetrapyrroles to graphene edges by surface-assisted covalent coupling, *Nat. Chem.*, 2017, **9**, 33–38.

151 T. Wu, G. Ding, H. Shen, H. Wang, L. Sun, Y. Zhu, D. Jiang and X. Xie, Continuous graphene films synthesized at low temperatures by introducing coronene as nucleation seeds, *Nanoscale*, 2013, **5**, 5456–5461.

152 D. Curcio, L. Omiciuolo, M. Pozzo, P. Lacovig, S. Lizzit, N. Jabeen, L. Petaccia, D. Alfè and A. Baraldi, Molecular Lifting, Twisting, and Curling during Metal-Assisted Polycyclic Hydrocarbon Dehydrogenation, *J. Am. Chem. Soc.*, 2016, **138**, 3395–3402.

153 B. Wang, X. Ma, M. Caffio, R. Schaub and W.-X. Li, Size-Selective Carbon Nanoclusters as Precursors to the Growth of Epitaxial Graphene, *Nano Lett.*, 2011, **11**, 424–430.

154 W. Chen, H. Chen, H. Lan, P. Cui, T. P. Schulze, W. Zhu and Z. Zhang, Suppression of Grain Boundaries in Graphene Growth on Superstructured Mn-Cu(111) Surface, *Phys. Rev. Lett.*, 2012, **109**, 265507.

155 X. Wan, K. Chen, D. Liu, J. Chen, Q. Miao and J. Xu, High-Quality Large-Area Graphene from Dehydrogenated Polycyclic Aromatic Hydrocarbons, *Chem. Mater.*, 2012, **24**, 3906–3915.

156 T. Sakurai, X. D. Wang, T. Hashizume, V. Yurov, H. Shinohara and H. W. Pickering, Adsorption of fullerenes on Cu(111) and Ag(111) surfaces, *Appl. Surf. Sci.*, 1995, **87**, 405–413.

157 H. W. Kroto, The stability of the fullerenes Cn, with n = 24, 28, 32, 36, 50, 60 and 70, *Nature*, 1987, **329**, 529–531.

158 H. Prinzbach, A. Weiler, P. Landenberger, F. Wahl, J. Wörth, L. T. Scott, M. Gelmont, D. Olevano and B. v Issendorff, Gas-phase production and photoelectron spectroscopy of the smallest fullerene, C20, *Nature*, 2000, **407**, 60–63.

159 H.-U. Blaser, Enantioselective synthesis using chiral heterogeneous catalysts., *Tetrahedron Asymmetry*, 1991, **2**, 843–866.

160 L. Addadi and S. Weiner, Biomineralization: Crystals, asymmetry and life, *Nature*, 2001, **411**, 753–755.

161 L. Pérez-García and D. B. Amabilino, Spontaneous resolution, whence and whither: from enantiomorphic solids to chiral liquid crystals, monolayers and macro- and supra-molecular polymers and assemblies, *Chem. Soc. Rev.*, 2007, **36**, 941–967.

162 R. S. Cahn, C. Ingold and V. Prelog, Specification of Molecular Chirality, *Angew. Chem. Int. Ed. Engl.*, 1966, **5**, 385–415.

163 K.-H. Ernst, Molecular chirality at surfaces, *Phys. Status Solidi B*, 2012, **249**, 2057–2088.

164 R. Raval, in *Chirality at the Nanoscale*, ed. D. B. Amabilino, Wiley-VCH Verlag GmbH & Co. KGaA, 2009, pp. 191–213.

165 K.-H. Ernst, Stereochemical Recognition of Helicenes on Metal Surfaces, *Acc. Chem. Res.*, 2016, **49**, 1182–1190.

166 M. Gingras, One hundred years of helicene chemistry. Part 3: applications and properties of carbohelicenes, *Chem. Soc. Rev.*, 2013, **42**, 1051–1095.

167 Y. Yang, R. C. da Costa, M. J. Fuchter and A. J. Campbell, Circularly polarized light detection by a chiral organic semiconductor transistor, *Nat. Photonics*, 2013, **7**, 634–638.

168 V. Kiran, S. P. Mathew, S. R. Cohen, I. Hernández Delgado, J. Lacour and R. Naaman, Helicenes—A New Class of Organic Spin Filter, *Adv. Mater.*, 2016, **28**, 1957–1962.

169 J. A. Lipton-Duffin, J. A. Miwa, M. Kondratenko, F. Cicoira, B. G. Sumpter, V. Meunier, D. F. Perepichka and F. Rosei, Step-by-step growth of epitaxially aligned polythiophene by surface-confined reaction, *Proc. Natl. Acad. Sci.*, 2010, **107**, 11200–11204.

170 M.-T. Nguyen, C. A. Pignedoli and D. Passerone, An ab initio insight into the Cu(111)-mediated Ullmann reaction, *Phys. Chem. Chem. Phys.*, 2010, **13**, 154–160.

171 L. Lafferentz, V. Eberhardt, C. Dri, C. Africh, G. Comelli, F. Esch, S. Hecht and L. Grill, Controlling on-surface polymerization by hierarchical and substrate-directed growth, *Nat. Chem.*, 2012, **4**, 215–220.

172 L. Cardenas, R. Gutzler, J. Lipton-Duffin, C. Fu, J. L. Brusso, L. E. Dinca, M. Vondráček, Y. Fagot-Revurat, D. Malterre, F. Rosei and D. F. Perepichka, Synthesis and electronic structure of a two dimensional π-conjugated polythiophene, *Chem. Sci.*, 2013, **4**, 3263–3268.

173 M. Chen, M. Röckert, J. Xiao, H.-J. Drescher, H.-P. Steinrück, O. Lytken and J. M. Gottfried,

Coordination Reactions and Layer Exchange Processes at a Buried Metal–Organic Interface, *J. Phys. Chem. C*, 2014, **118**, 8501–8507.

174 J. Eichhorn, T. Strunskus, A. Rastgoo-Lahrood, D. Samanta, M. Schmittel and M. Lackinger, On-surface Ullmann polymerization via intermediate organometallic networks on Ag(111), *Chem. Commun.*, 2014, **50**, 7680–7682.

175 Q. Fan, C. Wang, L. Liu, Y. Han, J. Zhao, J. Zhu, J. Kuttner, G. Hilt and J. M. Gottfried, Covalent, Organometallic, and Halogen-Bonded Nanomeshes from Tetrabromo-Terphenyl by Surface-Assisted Synthesis on Cu(111), *J. Phys. Chem. C*, 2014, **118**, 13018–13025.

176T. Dienel, J. Gómez-Díaz, A. P. Seitsonen, R. Widmer, M. Iannuzzi, K. Radican, H. Sachdev, K. Müllen, J. Hutter and O. Gröning, Dehalogenation and Coupling of a Polycyclic Hydrocarbon on an Atomically Thin Insulator, *ACS Nano*, 2014, **8**, 6571–6579.

177 R. Gutzler, L. Cardenas, J. Lipton-Duffin, M. E. Garah, L. E. Dinca, C. E. Szakacs, C. Fu, M. Gallagher, M. Vondráček, M. Rybachuk, D. F. Perepichka and F. Rosei, Ullmann-type coupling of brominated tetrathienoanthracene on copper and silver, *Nanoscale*, 2014, **6**, 2660–2668.

178 L. Dong, P. N. Liu and N. Lin, Surface-Activated Coupling Reactions Confined on a Surface, *Acc. Chem. Res.*, 2015, **48**, 2765–2774.

179 Q. Fan, J. M. Gottfried and J. Zhu, Surface-Catalyzed C–C Covalent Coupling Strategies toward the Synthesis of Low-Dimensional Carbon-Based Nanostructures, *Acc. Chem. Res.*, 2015, **48**, 2484–2494.

180 Q. Fan, T. Wang, L. Liu, J. Zhao, J. Zhu and J. M. Gottfried, Tribromobenzene on Cu(111): Temperature-dependent formation of halogen-bonded, organometallic, and covalent nanostructures, *J. Chem. Phys.*, 2015, **142**, 101906.

181 T. A. Pham, F. Song, M.-T. Nguyen, Z. Li, F. Studener and M. Stöhr, Comparing Ullmann Coupling on Noble Metal Surfaces: On-Surface Polymerization of 1,3,6,8-Tetrabromopyrene on Cu(111) and Au(111), *Chem. – Eur. J.*, 2016, **22**, 5937–5944.

182 Q. Fan, J. Dai, T. Wang, J. Kuttner, G. Hilt, J. M. Gottfried and J. Zhu, Confined Synthesis of Organometallic Chains and Macrocycles by Cu–O Surface Templating, *ACS Nano*, 2016, **10**, 3747–3754.

183 S. Grimme and S. D. Peyerimhoff, Theoretical study of the structures and racemization barriers of [n]helicenes (n = 3–6, 8), *Chem. Phys.*, 1996, **204**, 411–417.

184 F. Jensen, F. Besenbacher, E. Laegsgaard and I. Stensgaard, Dynamics of oxygen-induced reconstruction of Cu(100) studied by scanning tunneling microscopy, *Phys. Rev. B*, 1990, **42**, 9206–9209.

185 M. El Garah, J. Lipton-Duffin, J. M. MacLeod, R. Gutzler, F. Palmino, V. Luzet, F. Chérioux and F. Rosei, Self-Assembly of a Halogenated Molecule on Oxide-Passivated Cu(110), *Chem. – Asian J.*, 2013, **8**, 1813–1817.

186 M. Koch, Freie Universität, 2013.

187 M. Koch, S. Hecht and L. Grill, in *SpringerLink*, Springer, Berlin, Heidelberg, 2017, pp. 1–27.

188 T. A. Pham, B. V. Tran, M.-T. Nguyen and M. Stöhr, Chiral-Selective Formation of 1D Polymers Based on Ullmann-Type Coupling: The Role of the Metallic Substrate, *Small*, 2017, **13**, 1603675.

189 J. Liu, P. Ruffieux, X. Feng, K. Müllen and R. Fasel, Cyclotrimerization of arylalkynes on Au(111), *Chem. Commun.*, 2014, **50**, 11200–11203.

190 L. Smykalla, P. Shukrynau, M. Korb, H. Lang and M. Hietschold, Surface-confined 2D polymerization of a brominated copper-tetraphenylporphyrin on Au(111), *Nanoscale*, 2015, **7**, 4234–4241.

191 S. Kawai, K. Takahashi, S. Ito, R. Pawlak, T. Meier, P. Spijker, F. F. Canova, J. Tracey, K. Nozaki, A. S. Foster and E. Meyer, Competing Annulene and Radialene Structures in a Single Anti-Aromatic Molecule Studied by High-Resolution Atomic Force Microscopy, *ACS Nano*, 2017, **11**, 8122–8130.

List of Publications and conference contributions

Publications

- On-Surface Metalation and 2D Self-Assembly of Pyrphyrin Molecules Into Metal-Coordinated Networks on Cu(111)
  Jingyi Li, Christian Wäckerlin, Stephan Schnidrig, Evelyne Joliat, Roger Alberto, and Karl-Heinz Ernst
  Helv. Chim. Acta 100, **2017**, e1600278

- Surface-assisted diastereoselective Ullmann coupling of bishelicenes
  Christian Wäckerlin, Jingyi Li, Anais Mairena, Kevin Martin, Narcis Avarvari and Karl-Heinz Ernst
  Chem. Commun., 52, 2016, 12694

- From a 5-fold symmetric molecule to graphene on a Cu (111) surface
  Jingyi Li, Sam Lampart, Jay Siegel, Karl-Heinz Ernst, Christian Wäckerlin
  Manuscript in Preparation

Conference Contributions

- Self-metalation of pyrphyrin molecules on the Cu(111) surface
  J. Li, S. Schnidrig, E. Joliat, R. Alberto, K.-H. Ernst
  SAOG, Fribourg Switzerland, January 2015

- Metalation and 2D Self-Assembly of Pyrphyrin Molecules Into Metal-Coordinated Networks on a Cu(111) surface
  J. Li, Christian Wäckerlin, S. Schnidrig, E. Joliat, R. Alberto, K.-H. Ernst
  PhD Symposium 2016, Empa Dübendorf, November 2016

- Self-metalation and -assembly of Pyrphyrin on a Cu(111) surface
  J. Li, Christian Wäckerlin, S. Schnidrig, E. Joliat, R. Alberto, K.-H. Ernst
  CMD26, Groningen Netherlands, September 2016

- Self-assembly and metal coordination of surface-adsorbed Pyrphyrin molecules
  J. Li, Christian Wäckerlin, S. Schnidrig, E. Joliat, R. Alberto, K.-H. Ernst
  DPG 2017, Dresden Germany, March 2017

Curriculum Vitae

Jingyi Li

Born on 24/09/1987 in Henan, China

University of Zürich, Switzerland <u>08/2013 – 07/2017</u>

- Ph.D. in Surface Science
- Supervisor: *Prof. Karl-Heinz Ernst*, Lab for Nanoscale Materials Science, Empa Dübendorf

ETH Zürich, Switzerland <u>09/2010 – 06/2013</u>

- M.Sc. in Physics
- Thesis: "Exchange coupling between paramagnetic molecules and magnetic thin films", Thesis Supervisor: *Prof. Thomas A. Jung*, Lab for Micro and Nanotechnology, PSI Villigen

University of Bern, Switzerland <u>09/2009 – 01/2010</u>

- Exchange Student

Wuhan University, China <u>09/2006 – 07/2010</u>

- B.Sc. in Physics
- Supervisor: *Prof. Guojia Fang*, School of Physics and Technology, Wuhan University, Wuhan, China

CMSZH
CHEMICAL MOLECULAR SCIENCES ZURICH
GRADUATE SCHOOL